Development and Analysis of Photonic Crystal Fiber Mach-Zehnder Interferometer for Highly Sensitive Detection and Quantification of Gases

by

Kaveh Nazeri

B.Sc., Sharif University of Technology, Iran, 2005-2008
Continuation of B.Sc., Aachen University of Applied Sciences, Germany 2008-2010
M.Sc., Aachen University of Applied Sciences, Germany2010-2015

A Dissertation Submitted in Partial Fulfillment of
the Requirements for the Degree of

DOCTOR OF PHILOSOPHY

in the Department of Mechanical Engineering

Supervisory Committee

Development and Analysis of Photonic Crystal Fiber Mach-Zehnder Interferometer for Highly Sensitive Detection and Quantification of Gases

by

Kaveh Nazeri

B.Sc., Sharif University of Technology, Iran, 2005-2008
Continuation of B.Sc., Aachen University of Applied Sciences, 2008-2010
M.Sc., Aachen University of Applied Sciences, 2010-2015

Supervisory Committee

Dr. Colin Bradley, Department of Mechanical Engineering, University of Victoria
Supervisor

Dr. Rustom Bhiladvala, Department of Mechanical Engineering, University of Victoria
Departmental Member

Dr. Tao Lu, Department of Electrical and Computer Engineering, University of Victoria
Outside Member

Dr. Martin B. G. Jun, School of Mechanical Engineering, Purdue University
Additional Member

Abstract

Supervisory Committee

Dr. Colin Bradley, Department of Mechanical Engineering, University of Victoria
Supervisor
Dr. Rustom Bhiladvala, Department of Mechanical Engineering, University of Victoria
Departmental Member
Dr. Tao Lu, Department of Electrical and Computer Engineering, University of Victoria
Outside Member
Dr. Martin B. G. Jun, School of Mechanical Engineering, Purdue University
Additional Member

Gas sensing is essential for safety and maintenance operations in many industries, including power generation, petrochemical, capture and storage technologies, and the food-processing sector. The properties of fiber-optic sensors make them a superior choice for environmental monitoring applications, especially in extreme conditions, and particularly when compared against conventional electro-optical sensors. Their advantageous properties include immunity to electromagnetic radiation, high temperature durability, high sensitivity and the ability for high resolution detection, as well as multifunctional sensing capabilities such as temperature, humidity, pressure, strain, and corrosion. Among different types of interferometers, Mach-Zehnder Interferometers (MZI) have received significant attention because they are robust, compact, and have high levels of precision.

In this dissertation, we present an in-line and compact MZI point sensor designed for sensing refractive index. In comparison with various types of interferometers, fiber MZI based RI sensing was selected based on its enhanced sensitivity and fabrication simplicity. The MZI sensor is developed using photonic crystal fiber and demonstrated for high sensitivity detection and measurement of pure gases. The transmission spectrum of MZI sensors is formed by interference between the cladding and core modes. To construct the

device, the sensing element fiber was placed and aligned between two single-mode fibers with air gaps at each side. Two linear-translation micro stages were used to accurately differ and adjust gap lengths from 0 to 5mm. Great measurement repeatability was shown in the cyclic test for the detection of various gases such as methane and helium. A high RI measurement resolution of 2.1 E-7 and a sensitivity of 4629 nm/RIU was achieved, which is among the highest reported. Results show that the sensitivity of the fabricated MZI increases from 3000 nm/RIU to 4600 nm/RIU when the length of the sensing element fiber decreases from 5 mm to 3.3 mm. Furthermore, the device was packaged to demonstrate the laboratory-scale monitoring, as well as leakage detection of different concentrations of CO_2 in both subsurface soil and aqueous environments. Two water resistant but gas permeable membranes were used to package the sensor, to achieve a good balance of CO_2 permeability and water resistance. The experimental study of this work reveals the great potential of the fiber-optic approach for environmental monitoring of CO_2.

This study also explores other potential applications. Three types of sensors were fabricated using the proposed configuration employing 4 mm stub of (i) solid core Photonic Crystal Fiber (PCF), (ii) 10 µm Hollow core PCF (HC-PCF), and (iii) 20 µm HC-PCF as the sensing elements. We compared the performance of these sensors for detecting and measuring the quantity of gas present. As the transmission signals correspond to the frequency components in the sensor's Fast Fourier Transform (FFT) spectrum, the effect of gap distance on the number and amplitude distribution of the modes was examined in an effort to optimize the design elements. The MZI sensors are highly sensitive to low percentages of CH_4 and CO_2, making them suitable for greenhouse gas measurement.

Table of Contents

List of Tables

List of Figures

List of Abbreviations and Symbols

Abbreviation or Symbol	Definition
SMF	Single Mode Fiber
FBG	Fiber Bragg Grating
MFD	Mode Field Diameter
MZI	Mach-Zehnder Interferometer
RI	Refractive Index
RIU	Refractive Index Unit
PCF	Photonic Crystal Fiber
HC-PCF	Hollow-Core Photonic Crystal Fiber
FPI	Fabry-Perot interferometer
NA	Numerical Aperture
FFT	Fast Fourier Transform
CCS	Carbon Capture and Storage
OPD	Optical Path Difference
HST	Hollow Silica Tube
SEM	Scanning Electron Microscope
FWHM	Full Width at Half Maximum

Acknowledgments

In this acknowledgement, I would like to express my special thanks and sincere gratitude to my supervisors Dr. Colin Bradley and Dr. Martin B. G. Jun for the continuous support of my research, and for their motivation and patience. It was a great honor to work under their supervisions. Their support and willingness to help have always been helpful to overcome the challenges during my PhD.

Besides my advisors, I would like to thank my committee members, Dr. Tao Lu and Dr. Rustom Bhiladvala for their insightful comments, valuable suggestions and their encouragement.

I would also like to thank my colleagues and friends in the Adaptive Optics, and Advanced Multi-scale Manufacturing Laboratories at the University of Victoria, Dr. Vahid Ahsani, Dr. Farid Ahmed, JooYoung Lee, Yonghyun Cho, Dr. Vahid Moradi, Dr. Max Rukosuyev and many others.

Finally, I would like to express my gratitude to my parents for their lifetime support, constant love, and sacrifices. I could never have accomplished my PhD without their patience and encouragement.

Dedication

I dedicate this work and give special thanks to my lovely parents for their endless love, support, guidance and encouragement. I will always appreciate all they have done.

Chapter 1 Introduction

Optical fiber sensors have received attention over several years and researchers have pursued the applicability of optical fiber sensors across many sensing applications. For detecting or quantifying changes in the properties of a medium, especially in extreme conditions, the silica optical fiber provides a promising platform. Unique properties of optical fiber sensors over conventional sensors made them a better choice for environmental monitoring applications. Their properties consist of immunity to electromagnetic waves [4], high temperature durability [5], high accuracy and sensitivity [6], light weight, and multifunctional sensing capabilities [7] such as temperature, pressure, strain and corrosion, and the ability for high-resolution detection. Based on the working principle of the sensor, optical fiber sensors can generally be categorized as phase/intensity based, or as extrinsic/intrinsic sensors. When an optical fiber is exposed to a change in the properties of the surrounding medium, it modifies and modulates properties of light in the optical fiber. Thus, any change in properties of light can be measured at the detection end. Figure 1 illustrates light rays of a wave propagating along the z-direction with inclination angle ø, which is the phase difference between the two light rays belonging to the same wave.

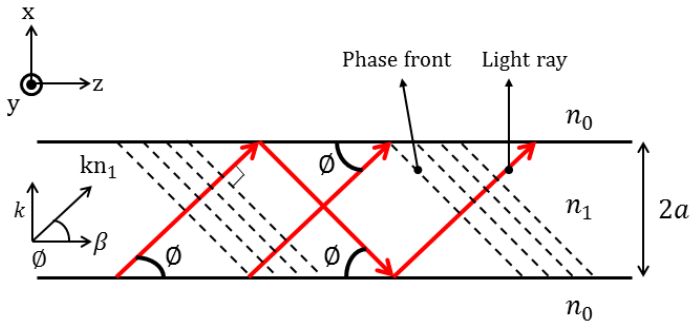

Figure 1.1 Light rays and their phase fronts in the waveguide.

By considering phase-matching condition, equation 1 represents the condition for propagation angle with wavenumber $k = {}^{2\pi}/_{\lambda}$:

$$\tan(kn_1 a \sin \emptyset - \frac{m\pi}{2}) = \sqrt{\frac{2\Delta}{Sin^2_{\phi}}} - 1 \quad ; \quad (m: integer) \qquad \textbf{(Eq. 1.1)}$$

It is been proved that the propagation angle of a light ray is discrete and is determined by the waveguide structure (core radius a, RI, RI-difference Δ) and λ of light source [166]. The optical field distribution that satisfies the phase matching condition of Eq. 1 is called the mode. Each mode is associated with light rays at a discrete angle of propagation [167]. The mode that has the minimum angle of φ (m=0) is called the fundamental mode. Modes in an optical fiber consist of transverse electric modes ($E_z = 0$), transverse magnetic modes ($H_z = 0$) and hybrid modes ($E_z \neq 0$; $H_z \neq 0$). A transverse mode of electromagnetic radiation is a particular electromagnetic field pattern measured in a plane perpendicular i.e. transverse to the propagation direction. These modes are specific to each waveguide and satisfy the orthogonality conditions between the modes [165]. For the construction of optical devices, it is necessary to utilize the light wave interaction between two propagating light beams in the adjacent waveguides. It is known that if two waveguides are brought close together, optical modes of each waveguide either couple or interfere with each other [165]. Coupled mode theory deals with the light wave interaction between two propagating modes. In order to analyze wave propagation in axially symmetric structures like optical fibers, Maxwell's equations are written in cylindrical coordinates. In a homogeneous dielectric medium, Maxwell's equations can be written in terms of electric field (e) and magnetic field (h) as [168]:

$$\nabla \times e = -\mu \frac{\partial h}{\partial t} \quad \textbf{(Eq. 1.2)}$$

$$\nabla \times h = \varepsilon \frac{\partial e}{\partial t} \quad \textbf{(Eq. 1.3)}$$

Permeability (μ) and permittivity (ε) of the medium are related to their values in vacuum of $\varepsilon_0 = 8.854 \times 10^{-12}$[F/m] and $\mu_0 = 4\pi \times 10^{-7}$[H/m] by $\varepsilon = \varepsilon_0 n^2$(n is the refractive index) and $\mu = \mu_0$. Considering an electromagnetic wave having angular frequency of ω and propagating in the Z-direction with propagating constant β, the electromagnetic fields in cylindrical coordinates for optical fibers can be written as:

$$\tilde{E} = E(r,\theta)e^{j(\omega t - \beta z)} \quad \textbf{(Eq. 1.4)}$$

$$\tilde{H} = H(r,\theta)e^{j(\omega t - \beta z)} \quad \textbf{(Eq. 1.5)}$$

where "r" is position in the plane transverse to Z-axis. Set of equations for analysis of propagation in optical fibers are provided on Appendix B.

The various mechanisms that have been investigated for refractive index-sensing functionality include Raman scattering [8], surface Plasmon resonance [9], evanescent-field absorption [10], derivative spectroscopy [11], and interferometric sensors [6]. Successes in these research projects relied upon experimentation with a range of optical fibers: D-shaped fiber, multimode fiber, fused silica fiber optic bundles, and photonic crystal fiber (PCF) [6, 8-11]. Different types of fiber-optic interferometers that have been studied for their RI-sensing capabilities include the Sagnac, Michelson, Fabry-Perot (FP), and MZI. A typical configuration of the fiber-optic MZI sensor has a sensing arm and a reference arm. The incident light is divided into two arms by a splitter and the light propagating in two paths is recombined by a coupler. The transmission spectrum of MZI sensors are formed by interference between the cladding

and core modes. The in-line MZI sensors composed of two contact arms formed with different optical fibers such as long-period gratings (LPGs) [142], splicing the core-offset [124], tapered fiber [125], microfiber [126], and micro-structured fiber [26]. A FP interferometer consists of two parallel mirrors that allows multiple round trips of light, and allows high transmission of certain optical frequencies. In contrast, a Michelson interferometer is usually made by a single beam splitter. In this type of interferometers only one output can be accessible and the other output returns back to the light source. Therefore, destructive or constructive interferences can be achieved. The Sagnac interferometer has a beam splitter which split the incoming light from light source into two beams. These beams circulate the interferometer and interfere on the splitter. One of the two output ports of the interferometer travels back to the light source and the other toward detector. Among different types of interferometers, MZIs have received significant attention because they are robust, compact, and have high levels of precision.

Solid and hollow-core PCF are the main focus of this research due to their distinguished properties such as high transmission, low background noise [129, 130], and tailored dispersion [131]. Photonic crystal fibers have a cladding which holds periodically spaced air holes. This provides a great opportunity for gas sensing because of the possibility of direct interaction between light and gas molecules. The light guidance mechanism in HC-PCF is distinct from the total internal reflection guidance in conventional fibers [140]. Hence, it provides long interaction length between a measurand gas and the transmitted light with high optical field confinement [43, 141]. The favored mode in HC-PCF has a quasi-Gaussian intensity distribution [45].

Generally, they support several higher order core modes and sometimes additional surface modes that are located on the core-cladding boundary [45]. It should be noted that fusion splicing of an HC-PCF to an SMF is more difficult than a PCF to an SMF because of the existence of hollow core, which holds much larger volume of air. The air will expand during splicing and distort the structure.

This research started with the fabrication of MZI sensors for high sensitivity liquid detection in the RI range of 1.33 to 1.42, deploying photonic crystal fibers. Fabrication procedure started with fabrication of MZI by fusion-splicing a short length of PCF and HC-PCF to single mode fibers with fully collapsed air holes in the splicing region, as shown in Fig 1.2. This happens as the structure of PCF has a lower softening point in comparison to SMF. As it has been reported that implementation of sensitive coatings onto optical fibers can enhance some characteristics of a sensor such as sensitivity and selectivity [100], deposition of polymers on the cladding air holes of PCF was performed using capillary force. The findings of this work are presented in the appendix A of this dissertation.

a) b)

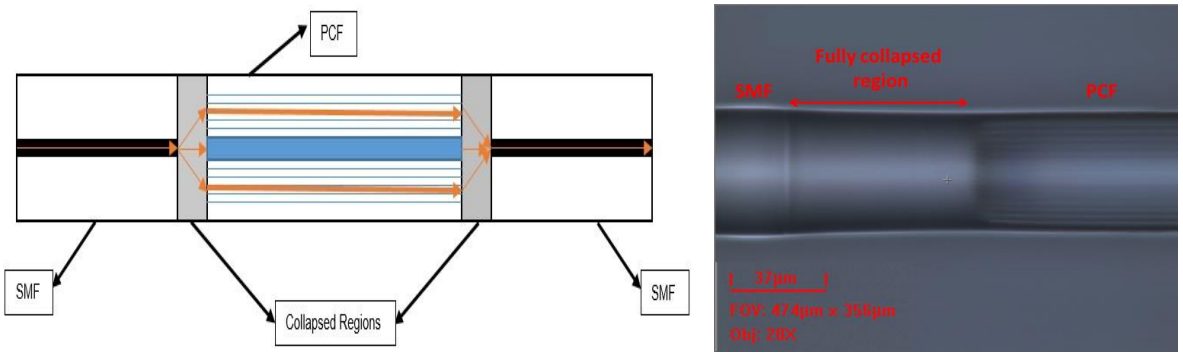

Figure 1.2 a) Schematic of SMF-PCF-SMF fusion splicing, b) microscopic image of a SMF fusion spliced to a solid core PCF with fully collapsed region.

The research continued with a focus on fabrication of MZI sensors for high sensitivity gas detection using photonic crystal fibers. Because of the challenges in splicing photonic crystal fibers, the idea of designing an MZI sensor without splicing was investigated. The main challenge in splicing of a PCF or HC-PCF is that the air that exists in the micro holes of the fiber will expand and distort the structure (Fig 1.3). It should be noted that the electric current as well as the duration of the arc have significant impact on fiber splicing.

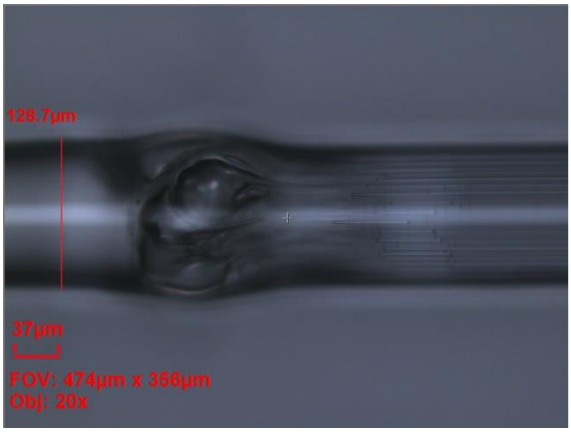

Figure 1.3 Microscopic image of a distorted splicing point during fusion splicing of a PCF

Butt coupling method was selected as an efficient way to fabricate the proposed gas sensor. In constructing the sensor, the SMFs and HC-PCF were assembled on a standard microscope glass slide (25 mm × 5 mm × 1 mm). Micro-machining using a femtosecond laser created a V-groove on the microscope glass (25 mm length, ~ 90 µm width, and ~ 50 µm depth), which is used to align fibers. The cleaved stub of HC-PCF was positioned in the middle of the V-groove and fixed using epoxy glue. Then the single-mode fibers were positioned on both sides of the sensing element fiber. To achieve a strong interference spectrum, gap lengths on both sides of the sensing

element fiber were manually adjusted. In this way, mode splitting and recombination can be controlled, and when an acceptable signal was observed, SMFs were glued to the glass slide. The resulting fiber sensors can measure the RI of a gas-filled cavity and they showed high-sensitivity to helium, methane, and carbon dioxide. The RI sensitivity of 4629 nm/RIU was demonstrated in the RI range of 1.0000347–1.000436 for the sensor with an HC-PCF length of 3.3 mm. Results show that the sensitivity of the proposed sensor increases when the length of the sensing element decreases. In addition, response and recovery times of the sensor inversely change with the length of HC-PCF.

Due to the fact that carbon dioxide is the greenhouse gas of most immediate concern, the research continues to focus on detection of CO_2. Early detection of CO_2 leakage is essential in several industries, which can be achieved using sensors with high-sensing resolution. Suitable packaging of a fiber-optic sensor is crucial for its reliable sensing operation and longer life span. Therefore, the device was packaged to make it operational in the subsurface and aqueous environment. The two membranes were assembled to achieve a good balance of CO_2 permeability and water resistance.

For a better understanding on the effect of photonic crystal fiber structure on the performance of the MZI sensor, three types of sensors were fabricated employing short stub of PCF, 10 µm HC-PCF, and 20 µm HC-PCF as the sensing elements. Furthermore, in order to explain the effect of gap distances on the performance of the sensor, it was necessary to have a fabrication setup capable of accurate control of gap distances. Thus, a simple and efficient fabrication setup was made using two linear-translation stages and a fiber alignment stage. For each sensor type, gap distances were

varied between 0.00 and 5.00 mm in 50-micron increments for each gap and transmission spectrums were recorded. These transmission signals correspond to the frequency components in the sensor's Fast Fourier Transform (FFT) spectrum. The effect of gap distance on the number and amplitude distribution of the modes was examined in an effort to optimize the design elements. Results show that for this type of MZI sensor, power is mainly carried by two dominant modes in the 10 μm MZI, three dominant modes in the 20 μm MZI, and one mode in the solid-core PCF. The highest amount of power transmission was recorded for an MZI with solid core PCF. Additionally, the power transmission and phase shift of dominant modes were studied for MZIs with different sensing elements. The final chapter summarizes the main results and suggests directions for possible future research.

1.1. Dissertation Outline

A brief framework of this dissertation is provided in this section. The first introductory chapter is written to link the context of the dissertation according to research progress. This thesis consists of a conference paper and of three papers that have already been published in different peer-reviewed journals. Information on each publication is provided on the first page of each chapter.

Chapter 2 demonstrates the development of an optical fiber gas sensor for high sensitivity detection and measurement of pure gases. The light propagation, working principle and essential performance parameters of the gas sensor are presented in this chapter. The proposed MZI sensor employed a short stub of 10 μm HC-PCF as the sensing element of a Mach-Zehnder interferometer. Fabrication of the sensor was done

by positioning and aligning the sensing element fiber between two single mode fibers with air gaps at each interface. Furthermore, the effects of length of HC-PCF on RI sensitivity, response and recovery times were studied. The RI sensitivity of 4629 nm/RIU was achieved in the RI range of 1.0000347–1.000436 for the sensor with an HC-PCF length of 3.3 mm.

Chapter 3 focuses on the performance of the optical fiber MZI sensor in the detection of carbon dioxide. Several experiments were performed to demonstrate the laboratory-scale monitoring and leakage detection of CO_2 concentration in both subsurface soil and aqueous environments. For this purpose, the sensor was packaged by two layers of gas permeable but water-resistant membranes. The spectrum of the sensor did not show any significant degradation under the soil and over the period of 24 hours in an aqueous environment. The sensor showed a stable and reliable measurement of CO_2 concentrations with a considerably short response and recovery times. For the test chamber with dimension of 14.5 cm × 11.2 cm × 4.4 cm, the sensor shows fast response and recovery times of 64 s, and 69 s, respectively. The resolution of the sensor was ~0.2% CO_2 and the sensor shows a linear response to CO_2 concentration with the sensitivity of 4.3 pm/ % CO_2.

Chapter 4 consists of several set of experiments on the proposed gas sensor, to understand and describe the effect of photonic crystal fiber structure and gap distances on the performance of the sensor. Three types of sensors were fabricated employing 4 mm stub of PCF, 10 μm HC-PCF, and 20 μm HC-PCF as the sensing elements. Furthermore, for all three types of sensors using two linear-translation stages, gap distances were varied between 0.00 and 5.00 mm in 50 micron increments for each gap

and transmission spectrums were recorded. These transmission signals correspond to the frequency components in the sensor's Fast Fourier Transform (FFT) spectrum. The effect of gap distance on the number and amplitude distribution of the modes was examined in an effort to optimize the design elements. This method can be an alternative approach to characterize and distinguish the presence of different gases. Spatial frequency analysis revealed that power is mainly carried by two dominant modes in the 10 μm MZI, three dominant modes in the 20 μm MZI, and one mode in the solid-core PCF. It was concluded that stronger interference occurs by using 20 μm HC-PCF as sensing element of the MZI, and a higher number of modes can be carried by this fiber. Furthermore, the 20 μm HC-PCF MZI sensor shows the fastest response/recovery time, while solid-core PCF-MZI shows the slowest response/recovery time. It should be noted that the instability of light source as well as inaccuracy in the distance between two ends of SMFs can impose errors on spatial frequency values. Errors associated with gap lengths can be eliminated by using automated fiber positioning systems. Besides, by equally splitting the fundamental core mode of the lead-in fiber into core and cladding modes of the HC-PCF, transmission fringe can be improved. The last chapter reviews and summarizes the main findings of this thesis and suggests some possible future research.

1.2. Research Contributions

The presented research shows the development and fabrication procedure of a highly sensitive fiber-optic MZI for ambient refractive index sensing. The main objectives were to fabricate reliable and accurate MZI gas sensors by implementing photonic crystal fibers.

Because of difficulties in splicing photonic crystal fibers, especially hollow-core fibers, MZI fabrication without splicing was considered as the main preference. Compactness, fast response, high resolution and high sensitivity, and easy fabrication procedure were the main concerns during development of new MZI configurations. The main contributions of this dissertation are provided below:

1. After studying the various types of MZI sensor configurations, the idea of designing an MZI sensor without splicing was investigated. Butt coupling method was selected as an efficient method to fabricate the proposed gas sensor. In order to eliminate the usage of fiber connectors and make it possible to align several fibers, a standard microscope glass slide was selected. Micro-machining using a femtosecond laser created a V-groove on the microscope glass (25 mm length, ~ 90 μm width, and ~ 50 μm depth), which was used to assemble and align SMFs and sensing element fibers. To achieve a strong interference spectrum, gap lengths on both sides of the sensing element fiber were manually adjusted. The resulting fiber sensors can measure the RI of a gas-filled cavity and they showed high-sensitivity to helium, methane, and carbon dioxide. The RI sensitivity of 4629 nm/RIU was demonstrated in the RI range of 1.0000347–1.000436 for the sensor with an HC-PCF length of 3.3 mm.
2. In order to evaluate the performance of the optical fiber MZI sensor in the leakage detection of different concentrations of carbon dioxide, several tests were performed for gas detection in a laboratory-scale test chamber, subsurface

soil and aqueous environments. Suitable packaging of the sensor was crucial for the mentioned set of experiments. Therefore, the device was packaged by several methods using different types of membranes and silica gels (aerogel) to make it operational in the aqueous environment. After securing the sensor, it was wrapped with two water-impermeable membranes to achieve a good balance of CO_2 permeability and water resistance. The packaged sensor was then wrapped with Tyvek to protect the sensor from dust. The sensor showed a stable and reliable measurement of CO_2 concentrations with a considerably short response and recovery times. The resolution of the sensor was ~0.2% CO_2 and the sensor shows a linear response to CO_2 concentration with the sensitivity of 4.3 pm/ % CO_2.

3. Performing the previously mentioned experiments raised several questions regarding the effect of the design elements on the performance of the MZI gas sensor. These questions including the effect of length of the sensing element fiber on the sensitivity and response time of the sensor, and the effect of the photonic crystal fiber structure on the performance of the sensor were addressed in this work. Furthermore, the effect of gap distance on the number and amplitude distribution of the modes, as well as phase shift of dominant modes were examined for three types of sensors. Three types of sensors were fabricated using short stub of PCF, 10 µm HC-PCF, and 20 µm HC-PCF as the sensing elements. For each sensor type, gap distances were varied between 0.00 and 5.00 mm in 50-micron increments for each gap. A fabrication setup capable of accurate control of gap distances was assembled using two linear-translation

stages and a fiber alignment stage. Transmission spectra were recorded to find their corresponding frequency components in the sensor's spectrum after performing the Fast Fourier Transform (FFT). FFT analysis revealed valuable information about power transmission as well as contributed modes for each sensor type.

Chapter 2 Hollow-Core Photonic Crystal Fiber Mach-Zehnder Interferometer for Gas Sensing

This paper was published in Journal of Sensors (MDPI) in May 2020.

Kaveh Nazeri, Farid Ahmed, Vahid Ahsani, Hang-Eun Joe, Colin Bradley, Ehsan Toyserkani, and Martin B. G. Jun. "Hollow-Core Photonic Crystal Fiber Mach-Zehnder Interferometer for Gas Sensing", Sensors 2020, 20(10), 2807.

Abstract

A novel and compact interferometric refractive index (RI) point sensor is developed using hollow-core photonic crystal fiber (HC-PCF) and experimentally demonstrated for high sensitivity detection and measurement of pure gases. To construct the device, the sensing element fiber (HC-PCF) was placed between two single-mode fibers with air gaps at each side. Great measurement repeatability was shown in the cyclic test for the detection of various gases. The RI sensitivity of 4629 nm/RIU was demonstrated in the RI range of 1.0000347–1.000436 for the sensor with an HC-PCF length of 3.3 mm. The sensitivity of the proposed Mach-Zehnder interferometer (MZI) sensor increases when the length of the sensing element decreases. It is shown that response and recovery times of the proposed sensor inversely change with the length of HC-PCF. Futhermore, spatial frequency analysis for a wide range of air gaps revealed information on the number and power distribution of modes. It is shown that the power is mainly carried by two dominant modes in the proposed structure. The proposed sensors have the potential to improve the ability of current technology to detect and quantify pure gases.

2.1. Introduction

Gas sensing is essential for safety and maintenance operations in many industries, including the power generation [1], petrochemical [2], and food-processing sectors [3]. For detecting the presence of gases, especially in extreme conditions, the silica optical fiber provides a promising platform due to its unique properties. These include immunity to electromagnetic radiation [4], high-temperature durability [5], compactness, as well as high accuracy and sensitivity [6]. Researchers have pursued the applicability of optical fiber sensors across many sensing applications, because of their multifunctional sensing capabilities (e.g., RI, temperature, and pressure) [7]. The various mechanisms that have been investigated for gas-sensing functionality include Raman scattering [8], surface Plasmon resonance [9], evanescent-field absorption [10], derivative spectroscopy [11], and interferometric sensors [6]. Successes in these research projects relied upon experimentation with a range of optical fibers: D-shaped fiber, multimode fiber, fused silica fiber optic bundles, and photonic crystal fiber (PCF) [6, 8-11]. Various types of fiber-optic interferometers have been studied for their RI-sensing capabilities including the Sagnac, Michelson, Fabry-Perot, and Mach-Zehnder interferometers (MZIs) [6]. Wang et al. [12] developed a micro Fabry-Perot cavity interferometer and achieved the RI sensitivity of 851 nm/RIU, while having very low temperature sensitivity of 0.27 pm/°C and low temperature cross-sensitivity of 3.2 E-7 RIU/°C. Hu et al. [13] proposed an intrinsic Fabry-Perot interferometer based on simplified hollow core fiber and achieved resolution of 6.5 E-5 in RI measurement. Key features of this sensor type are easy fabrication process and low loss. An example of Michelson interferometer is the RI sensor engineered by Jha et al. [14] by splicing a stub of large-mode area PCF to SMF. They achieved RI resolution of E-4 in the RI

range of 1.33–1.45. Sun et. al [15] proposed a hybrid interferometer by forming a Fabry-Perot cavity in one of the optical paths of the Michelson interferometer. The spectral response of this hybrid sensor demonstrated two distinctive interference fringes. The simultaneous measurement of RI and temperature revealed a resolution of 8.7 E-4 in the RI range of 1.33–1.38 with temperature sensitivity of 13 pm/°C. A photonic crystal fiber Sagnac interferometer was developed by Liu et al. [16] as an RI sensor by filling the central hole of the fiber with microfluidic analytes. Fabrication of this sensor types are complicated as filling air holes of a PCF is challenging. A high sensitivity of about 19000 nm/RIU with the resolution of 1.05 E-6 was achieved in their work. Among these, MZIs have received significant attention because they are robust, compact [17], and low-cost units that also have high levels of precision [18].

Other researchers have proposed disparate configurations in fabricating in-line MZI sensors for sensing ambient RI changes. Implementation techniques already tested extend from core mismatch splicing of optical fibers [19] to cladding collapse of PCF [20], tapering of fibers [21], the use of microfiber [22], and splicing of hollow-core fiber [23]. Similarly, many approaches have been used in attempts to enhance ambient refractive index sensitivity of fiber-optic MZIs. Huang et al. [18] developed a thin-core fiber-based MZI for ammonia sensing with a sensitivity of 850 nm/RIU in the RI range of 1.5–1.518. In other studies, graphene-coated fiber-optic MZI sensors were found to have gas sensing sensitivity in the range of 3–6 pm/ppm [24, 25]. Duan et al. [26] engineered a compact MZI by creating a short length (62.5 μm) of cavity through offset-splicing the SMFs on both ends. Their innovative design resulted in a sensitivity of 3400 nm/RIU in the RI-range 1.0–1.0022. PCF has also proven to be an excellent choice for fabricating RI sensors because the effective RI

of the propagating cladding mode is highly sensitive to the surrounding environment [27–29]. Yang et al. [29] demonstrated the viability of a compact PCF Mach-Zehnder refractometer for sensing methane. They coated a polymer (fluoro-siloxane) over the internal surface of air holes, with one end of the PCF fusion spliced to an SMF while the other end was open for gas-molecule penetration. Through this fabrication technique, a sensitivity (defined as wavelength change per percentage of methane) of 0.514 nm%-1 was achieved [29]. This otherwise promising sensor type has drawbacks; it requires a long response time when retrieving initial conditions and also has a low level of gas selectivity.

The article by Cregan et.al in 1999 was the first research that utilized HC-PCF for the application of gas detection [30]. The presence of hollow channels in a fiber's core and cladding regions makes it difficult to fusion splice an HC-PCF to an SMF. The air holes in HC-PCF hold a large volume of air. During fusion splicing, air will expand and distort the fiber structure. In 2011, Qu et al. [31] suggested using hollow-core fiber to infiltrate various aqueous analytes in high RI measurements with a sensitivity of 1400 nm/RIU. Subsequent to this innovative proposal, a 5.1 m HC-PCF gas cell was used for the detection of methane [32]. Generally, it takes time for gas molecules to fill the cavities of HC-PCF, so this technique makes a delay in the initial measurement response to the presence of the gas [33]. Furthermore, the suggestion of Wynne et al. [34] regarding the pressure-driven filling of air-holes with gases is not applicable for real-time monitoring. Moreover, focused ion beam or femtosecond laser-assisted micro-channels can be fabricated on the cladding of HC-PCF to accelerate gas diffusion [35, 36]. Nicholas et al. [37] proposed an HC-PCF-based MZI using ceramic ferrules to connect a 344 mm long HC-PCF to two SMFs. An alternative HC-PCF-based MZI gas sensor has been reported, which employs the HC-PCF as one of the

interferometer's arms [38]. Many of the sensors proposed to date either have complex configurations or poor sensitivity and response time for high-resolution measurement of gases. Recently, Ahmed et al. [39] reported a highly sensitive MZI structure that uses a small stub of HC-PCF for monitoring of CO_2. However, a detailed study on such a configuration is necessary to better understand its performances and to explore other potential applications. Recently, we studied length-dependent performance of these devices to understand their sensing properties [40]. However, more studies are required to better understand design parameters and sensing performance of these MZI sensors.

An in-line fiber-optic MZI sensor, which is compact and robust with high sensitivity, is presented in this report. The HC-PCF MZI sensor utilized a short length of HC-PCF placed in between two SMFs with gaps at each interface. The light propagation, working principles, and essential performance parameters of the proposed gas sensor are presented in this study. These include response and recovery times, RI sensitivity, as well as the number and power distribution of modes. Relative RI detection was used in all experiments, because of the difficulties in absolute RI measurement with high accuracy [41]. Experiments show promising results in the sensor's RI sensitivity. The device responds well to different gases and shows good repeatability on gas detection. Comparing performance of the proposed MZI with other MZI gas sensors reported in this report shows that this MZI has a high resolution of 2.1 E-7, and sensitivity of 4629 nm/RIU which is among the highest reported. It is also a cost effective product because it is compact, and only a few mm of HC-PCF is required for fabrication of each sensor. It is shown that the RI sensitivity of the HC-PCF MZI sensors increases as the length of the HC-PCF stub decreases. In addition, implementing short lengths of HC-PCF as the sensing element improves response time of the sensor, leading to a

faster response to the presence of a measurand gas. For example, the proposed sensor has a response time of 32 seconds in detection of methane. The main drawback of this sensor is gas selectivity, as its response to the presence of any gas and is not selective. Furthermore, the present study investigates the temperature sensitivity of the HC-PCF MZI sensor, as the effect of temperature cross-sensitivity needs to be considered and compensated in ambient RI measurement. The proposed sensors have the potential to improve current technology's ability to detect and quantify pure gases.

2.2. Working Principle

Figure 2.1 (a) schematically shows a fiber arrangement of the proposed MZI sensor. A short length of HC-PCF was positioned on the V-groove and aligned with SMFs. There is an air gap at each end of the sensing element fiber. The schematic illustration of light transmission in the sensor is shown in Figure 2.1 (b). The lead-in SMF carries the incoming light wave. It radiates from the SMF core after reaching the first sensor gap in region 2 and acts as a pseudo-point light source. In the first air gap, the fundamental mode broadens and when it reaches the HC-PCF both fundamental and higher-order modes are excited in the circular channels of the sensing element. Interaction between the light and the gas molecules takes place in region 3 along the length of the sensor. Optical interference occurs in region 4 (second gap) due to the phase difference between the fundamental mode and higher-order modes. The lead-out SMF then transfers the interference spectrum to an interrogator (or spectrum analyzer). The device's reference and sensing arms are both in contact with gas molecules. However, the effect of RI change on the interference in the sensing arm is higher

than in the reference arm. That imbalance occurs due to differences in optical-path lengths and phase shifts between the arms.

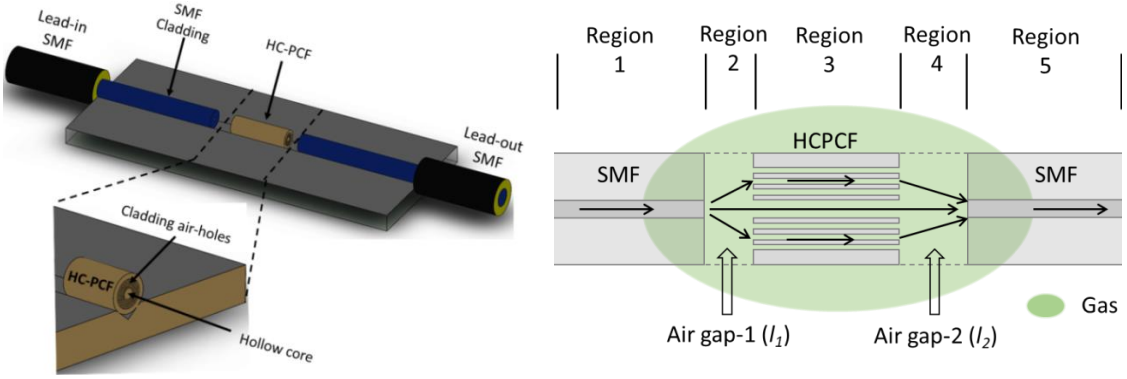

(a) (b)

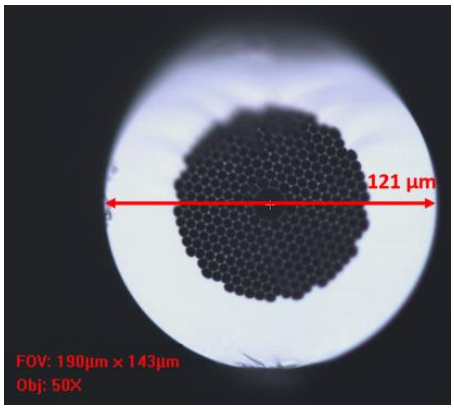

(c)

Figure 2.1 (a) Schematic of the proposed sensor arrangement, (b) Schematic of light transmission within the sensor, (c) microscopic image of the cross-section of 10 micron HC-PCF fiber.

Figure 2.1 (c) shows the cross-section of the HC-PCF used in this study. This fiber offers low index guiding of light as the core-index of the HC-PCF is lower than the effective index of the cladding [42]. The photonic bandgap effect makes propagation impossible in the microstructure cladding leading to light confinement in the core. This design enhances gas sensing capabilities as the HC-PCF provides a remarkably strong interaction between gas

molecules and light particles due to strong field confinement [43, 44]. Higher-order core modes and surface modes are supported by HC-PCF fibers [45]. The optical path difference between the reference arm and sensing arm defines the fiber-optic MZI sensor's interference spectrum. Such interference is a function of core intensity (I core), cladding intensity (I cladding), and phase difference (ϕ) [17, 46], which can be written by the following equation:

$$I = I_{core} + I_{cladding} + 2\sqrt{I_{core} I_{cladding}} \cos \emptyset \qquad \textbf{(Eq. 2.1)}$$

Modes that are traveling the same distance (L) will have the phase difference ($\Delta\phi$) of:

$$\Delta\phi = 2\pi(\Delta n_{eff})L\,\lambda^{-1} \qquad \textbf{(Eq. 2.2)}$$

Δn_{eff} is the difference in the effective RI between the core and cladding modes in equation 2, λ is the input wavelength, and L is the length of the HC-PCF path. Maximum transmission occurs at $\Delta\Phi = 2\pi m$ (m is an integer) and peaks form on the transmission signal at the following wavelengths:

$$\lambda_m = (\Delta n_{eff})L\,m^{-1} \qquad \textbf{(Eq. 2.3)}$$

Therefore, the m^{th} order spectral shift can be written as:

$$\Delta\lambda_m = (\Delta n_{eff} + \Delta n)L\,m^{-1} - \Delta n_{eff}\,m^{-1} = \Delta nL\,m^{-1} \qquad \textbf{(Eq. 2.4)}$$

L is constant in the above equation and as a result the refractive index of the MZI's core and cladding will change Δn and correspondingly $\Delta\lambda_m$. Consequently, a shift occurs at the transmission spectrum of the device and such change can be used for sensing a measurand.

2.3. Experimental Procedures

2.3.1. Fabrication of the MZI sensor

Two types of fibers were used to fabricate the HC-PCF MZI sensors: the SMF (Corning SMF28) and the HC-PCF (NKT Photonics HC-PCF 1550). Lead-in and lead-out fibers are standard single-mode fibers (SMF-28) with a core diameter of 8.2 μm, numerical aperture of 0.13, and a mode field diameter (MFD) of 9.3 μm (±0.5 μm). This sensor type utilizes an NKT Photonics HC-PCF fiber (HC-PCF 1550) as the sensing element. The HC-PCF fiber has a numerical aperture (NA) of 0.2, MFD of 9.00 μm (±1 μm) and core diameter of 10.00 μm. This sensing fiber element also has cladding air holes of diameter 3.10 μm and a cladding pitch of 3.80 μm. These fibers can guide several modes within a transmission of 1490–1680 nm [30]. In constructing the sensor, the SMFs and HC-PCF were assembled on a standard microscope glass slide (25 mm × 5 mm × 1 mm). Micro-machining created a V-groove on the microscope glass (25 mm length, 95 μm width, and 48 μm depth) using a femtosecond laser, which is used to align fibers. A CT-30 Fujikura cleaver was used to cleave the fibers. To be able to cleave short lengths of HC-PCF in the order of a few millimeters, it was necessary to extend the length of the adapter plate in order to decrease the distance between the cutting blade and the adapter plate. Therefore, a 4 mm long aluminum plate was machined with marks at increments of 1 mm on it. Attaching the extension plate to the adapter plate made it possible to cleave fibers with lengths down to 2 mm. The cleaved stub of HC-PCF was positioned in the middle of the V-groove and fixed using epoxy glue. The exact length of the fiber, as well as the cleaving angles on both sides of the cleaved HC-PCF, were checked by examining them under an optical tooling microscope. Afterward, the single-mode fibers were positioned in fiber holders mounted on linear-translation micro-

stages and aligned with the sensing element fiber on the V-groove. Figure 2.2 (a) shows an isometric view of the fabrication setup. To achieve a strong interference spectrum, gap lengths on both sides of HC-PCF were accurately adjusted. In this way, mode splitting and recombination can be controlled. Fibers were then glued to microscope glass when an acceptable signal was observed. To provide mechanical strength to the assembly, the glass slide was secured in a meshed stainless-steel tube, as shown in Figure 2.2 (b). Testing proved the robust effectiveness of the resulting sensor. Spacing between the HC-PCF and SMFs enabled ambient gas to diffuse into the HC-PCF air holes.

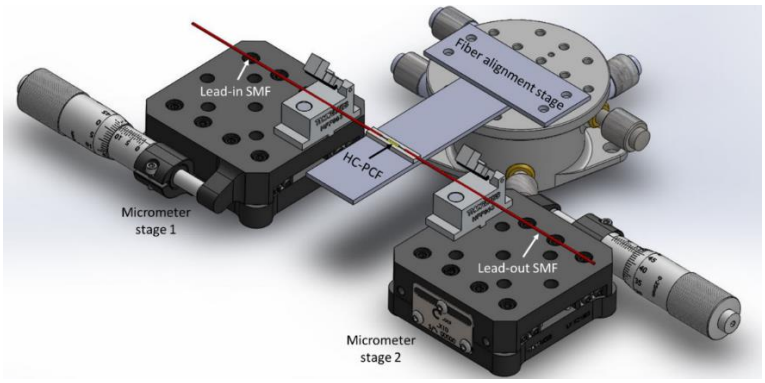

(a)

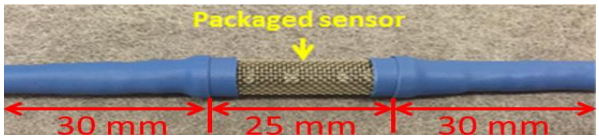

(b)

Figure 2.2 (a) Isometric view of the fabrication setup using two linear-translation micro stages for accurate control of gap distances, (b) Packaged sensor using meshed stainless steel tube.

The normalized transmission spectrum of a sensor with an HC-PCF length of 3.30 mm and a gap distance of 1 mm on each side (Sensor C) is shown in Figure 2.3 (a). Figure 2.3 (b) shows the fringe spacing of the same sensor. The measurement was taken when the device was immersed in nitrogen (99.99% pure, atmospheric pressure) at room temperature. Each

valley measured at the sensor's output, see Figure 2.3 (a), results from interference between the signal arms in the MZI at that wavelength. The magnified spectrum graph shows a fringe spacing of 1.91 nm and a full width at half maximum (for transmission dip) of 0.47 nm. For the same configurations, the fringe spacing of sensor A (L = 4.97 mm) and sensor B (L = 4.73 mm) are 1.70 nm and 1.74 nm, respectively. The fringe spacing of the transmission spectrum increases as the length of HC-PCF decreases.

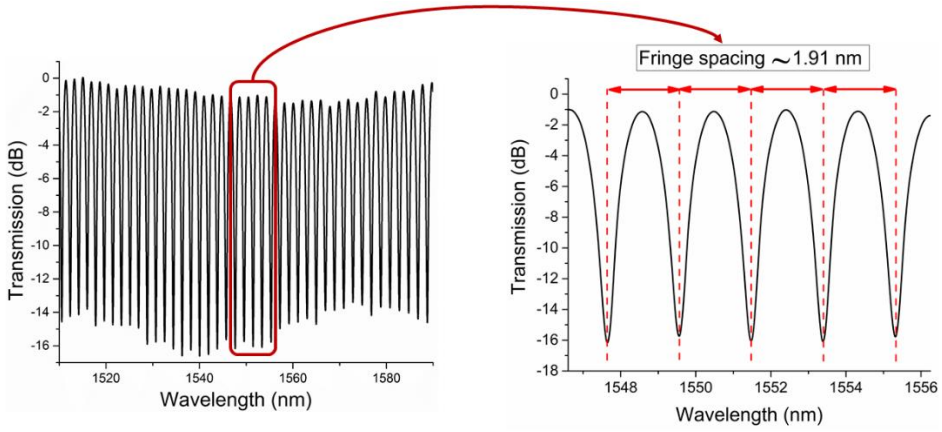

(**a**) (**b**)

Figure 2.3 (a) Normalized transmission spectrum of an HC-PCF MZI sensor with HC-PCF length of 3.3 mm and gaps of 1 mm immersed in nitrogen at room temperature and atmospheric pressure, (b) Fringe spacing of the same sensor.

2.3.2. Spatial Frequency Analysis

In order to analyze the modes participating in the modal interference process, the transmission spectrum of MZIs with 4 mm of HC-PCF as a sensing element was Fourier transformed. This process allowed us to obtain the sensor's corresponding spatial frequency, described as $v = \frac{\Delta n_{eff}.D}{\lambda^2}$ [47], where Δn_{eff} represents the effective RI-difference between core and cladding of the sensing element and D is the distance between SMFs at each of the sensor's ends. D varies from 4 mm to 16 mm in 500-micron increments. Different peaks in

the spatial frequency graph correspond to the interference between the fundamental mode and different higher-order modes.

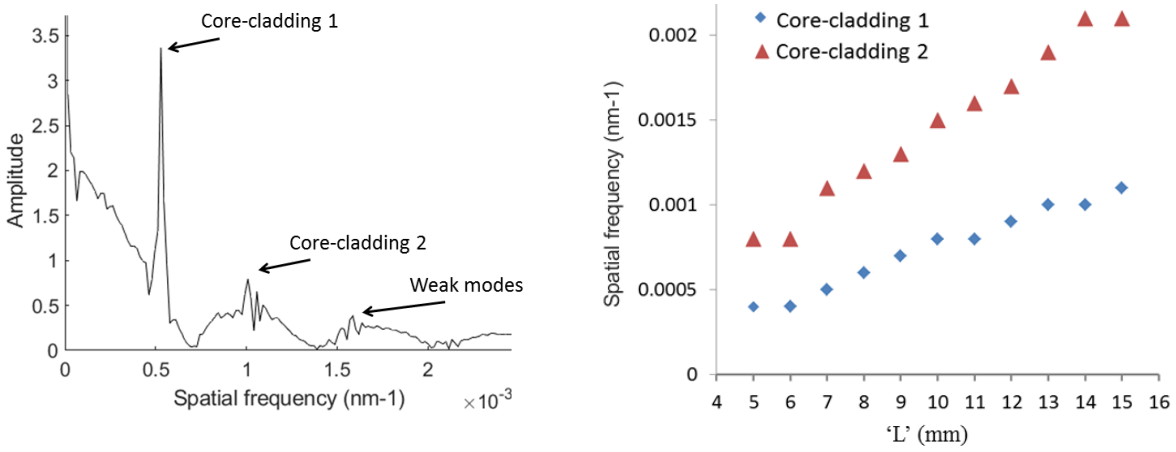

(a) (b)

Figure 2.4 (a) Spatial frequency graph for MZI with HC-PCF length of 4 mm and D of 7 mm, (b) Tracking dominant modes of the sensor for D.

Testing the MZIs with 10 µm HC-PCF as their sensing element revealed several multimodal-interference patterns occurring in the transmission spectrum. Furthermore, power is mainly distributed in such a sensor between two dominant modes in the spatial frequency spectrum, a finding that holds true across the entire range of gap distances. This phenomenon confirms that higher-order modes would gradually leak off the sensing fiber, contributing to transmission losses. Thus, fewer peaks would turn up in the spatial frequency graph due to a weakening interference-effect. As an example of the described effect, Figure 2.4 (a) presents the spatial frequency graph for an MZI with 4 mm of 10 µm HC-PCF and gaps of 1.5 mm on each side (D = 7 mm). The sensor has a strong cladding mode with a spatial frequency of 5×10^{-4} (1/nm) and a normalized FFT value of 3.14 and labeled core-cladding 1. Besides this dominant cladding mode, the sensor has a relatively weaker cladding mode (core-cladding 2) with a spatial frequency of 1.1×10^{-3} (1/nm) and a normalized FFT value of 0.99.

Experimental findings show that for gaps from 0 to 1.65 mm, core-cladding 1 is the dominant cladding mode, while for higher gaps core-cladding 2 became the dominant mode. The highest power transmission resulted in MZIs with gaps of 1.35 mm, and the amplitude of spatial frequencies was seen to decrease intensely for gaps greater than 4.5 mm. Figure 2.4 (b) was plotted by tracking dominant modes to show how the magnitude of spatial frequencies increases by increasing gap lengths for this sensor.

2.3.3. Characterization

In the first set of experiments, RI measurements using three MZIs (constructed with different lengths of HC-PCF as their sensing elements) were carried out and their relative performances were compared. Figure 2.5 schematically shows the sensor evaluation system that includes the optical interrogator, a circulator, the MZI sensor, a Fiber Bragg Grating (FBG), reference gas tank, and measurand gas tanks. The MZI sensors under investigation were placed in a chamber with four gas intake valves. Reference nitrogen (N_2) and measurand gas-tanks (He, Ar, and CH_4) were connected to these valves. The experiment used helium, methane, and argon with purity levels of 99.999%, 99%, and 99.99%, respectively. Using pressure regulators, an injection pressure of 15 psi was maintained during the testing process. To maintain constant pressure in the test chamber a discharge tube with a bubbler was connected to the test chamber. An interrogator (SM125) with a resolution of 1 pm was used to record and evaluate changes in the transmission spectrum. In addition, a FBG (sensitivity ~10 pm/°C) was positioned in the chamber to monitor and record the temperature variations. The spectral shifts of three sensor types and FBG were analyzed using the Micron Optics' Enlight software. The experiments started with injecting N_2 into the test chamber for

long enough time to make sure an even gas diffusion into the air holes of HC-PCF was achieved. Measurand gases were then injected into the chamber (He, Ar, or CH_4). Using the mentioned software, spectral responses were recorded. Response and recovery times as well as refractive index sensitivity are among important sensing performance parameters of a gas sensor and were studied for three MZIs. The cyclic tests were performed using the various sensors to inspect the repeatability of RI measurements. Temperature, pressure and the injected gas species determined the spectral response of each sensor. Therefore, MZI sensors were temperature-characterized to compensate for the effect of temperature fluctuations during the experiments.

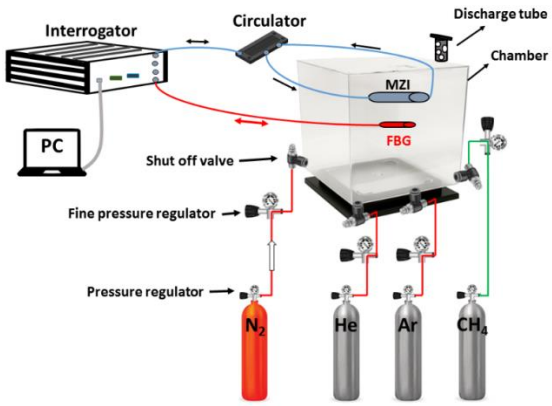

Figure 2.5 Schematic of the experimental setup; tests were carried out at atmospheric pressure and room temperature.

Another set of experiments sought to analyze the effect of gap distances on modal interference in the proposed MZI gas sensor. Here, lead-in and lead-out SMFs were not glued to the glass to facilitate easy adjustment of both airgaps. Using linear micro stages, gap lengths increased from 0 to 6 mm in 500-micron increments. Ensuring equal gap distance on both sides, we collected transmission spectrums for an interferometer with 10 μm HC-PCF as

its sensing fiber. Spectrums were Fourier transformed to produce spatial frequency graphs, to explore the power distribution and the number of the sensor's modes.

2.4. Results and Discussion

2.4.1. Refractive Index Sensing

Figure 2.6 (a) illustrates the responses of sensor A (L = 4.97 mm) to methane, argon, and helium for one cycle. MZI sensors were exposed to measurand gases separately to determine its spectral response to each gas. The sensor was interrogated with each measurand gas to investigate its spectral response in a complete test cycle. Each cycle started with the injection of nitrogen (99.99% pure) until saturation followed by injection and measurement of target gas; and finally, an injection of nitrogen back into the chamber to purge the gas. The injection of gases was carried out for 7 minutes at each stage of a test cycle. As shown in Figure 2.6, the ambient gas in the test chamber determines the sensor's wavelength response. Considering the location of the spectrum in N_2 as the reference, sensor A showed spectrum shifts of 780 pm (±6 pm) when immersed in helium, 45 pm (±1 pm) when immersed in argon, and 440 pm (± 3 pm) when immersed in CH_4 Spectral shifts of three valleys at different wavelengths were used to estimate mean wavelength shifts and measurement errors. Redshifts were recorded in the transmission spectrum for Ar or He and blue shifts were recorded for CH_4. This finding can be explained in terms of spectral response to RI change. For a given ambient RI, the sensor's transmission spectrum shows redshift to a negative RI change and blue shift to a positive RI change. In standard conditions, the RI values of He, Ar, N_2 and CH_4 are 1.0000347, 1.0002820, 1.0002944, and 1.0004365, respectively. The interference fringe showed a redshift in the presence of helium and argon because the RI of

nitrogen is higher than the RIs of helium and argon. In contrast, the spectrum underwent a blue shift for methane, as the RI of nitrogen is lower than the RI of methane. The transmission fringe shifts of MZI sensors for helium, methane, and argon are listed in Table 2.1.

Table 2.1. Transmission fringe shift of the MZI sensors for helium, methane, and argon.

Sensor	HC-PCF Length	Spectral shift (pm) in helium	Spectral shift (pm) in methane	Spectral shift (pm) in argon	RI sensitivity (nm/RIU)
A	4.97 mm	780	440 (negative)	45	3019
B	4.73 mm	1060	600 (negative)	70	4300
C	3.30 mm	1300	618 (negative)	100	4629

Sensor C, which has the shortest length of HC-PCF, shows the highest wavelength shifts among the three sensors tested when interrogated with all three gases. In contrast, sensor A, which has the longest HC-PCF stub of the three sensors, shows the smallest shifts. The RI sensitivities of the interferometric sensors are listed in table 2.1, all falling in the RI range of 1.0000347–1.0004365. This RI range was selected based on the availability of gas tanks, and it could be extended in future research. The highest sensitivity was achieved by sensor C: 4629 (nm/RIU). This suggests that the RI sensitivity of the HC-PCF MZI sensors increases as the length of the HC-PCF stub decreases. As the next step in our experiments, argon, methane, and helium gases were sequentially injected into the test chamber, to investigate the sensors' capacities to detect multiple gases. In each test cycle, the gas injection was carried out in the sequence of N_2, Ar, N_2, CH_4, N_2, He, and N_2. This sequence was then repeated

three times to determine sensing repeatability. Figure 2.6 (b) shows the sequential gas response for sensor A, where the test cycles produced identical results. An FBG was used to record any temperature variation during the test. A maximum temperature fluctuation of 1°C was recorded during the entire experiment.

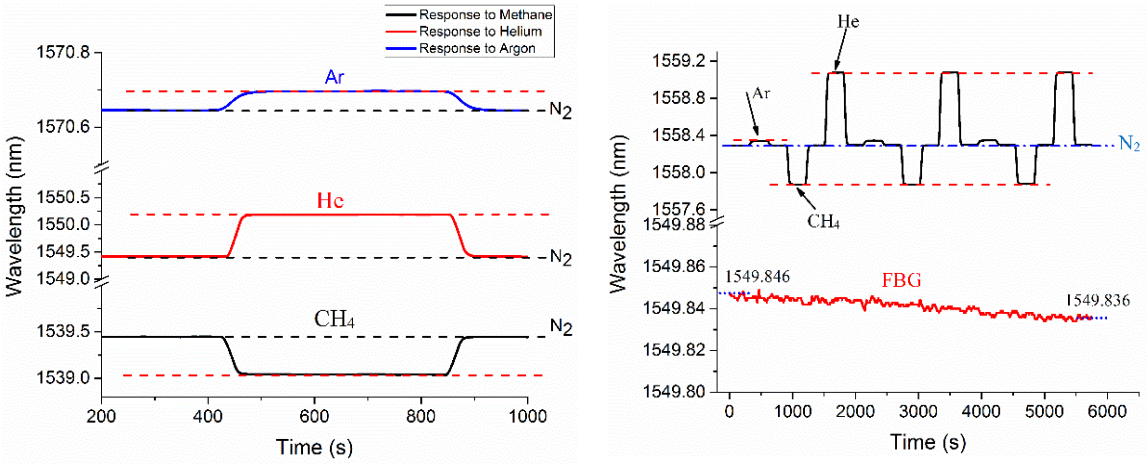

(a) (b)

Figure 2.6 (a) The spectral shifts of Sensor A when immersed in argon, helium, and methane injections, (b) The results of sequential sensing of measurand gases with Sensor A, with gas injections carried out in the sequence of argon, methane, and helium.

To check the consistency of the sensor's measurements, repeatability tests were performed using all three sensors. For each test cycle, the sequential injection of nitrogen, measurand gas, and nitrogen was performed at 5 minutes intervals. Figure 2.7 (a) shows the repeatability of sensing helium gas using all three sensors for eight cycles. The repeatability test for sensing methane gas was conducted for three test-cycles, as shown in Figure 2.7 (b). Both graphs below show the normalized wavelength shift that resulted when the chamber was sequentially filled with nitrogen and measurand gases. The data shows great repeatability of gas detection using the proposed HC-PCF interferometer.

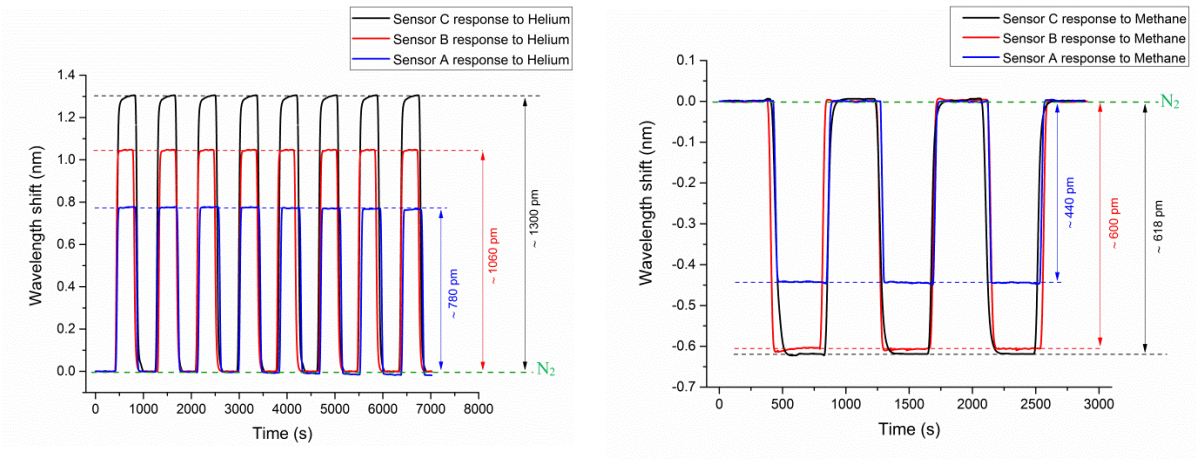

(a) (b)

Figure 2.7 The normalized cyclic response of HC-PCF MZI sensors to (a) helium and (b) methane.

The RI sensitivity of sensors A, B, and C are 3019 nm/RIU, 4300 nm/RIU, and 4629 nm/RIU, respectively. Figure 2.8 shows the RI sensitivity of Sensor A in the mentioned RI range. These data points were obtained via five separate measurements with a measurement error of ± E-6, ± 2.3 E-6, and ± 5 E-7 for methane, helium, and argon, respectively. The proposed sensor configuration can improve on current technology due to its linear RI response and high sensitivity to gases. The proposed interferometric sensor has, nonetheless, the potential for advancing current capacity for gas detection, quantitatively analyzing changes in pure gases, as well as environmental monitoring applications. The RI characterization tests were conducted using an optical interrogator that has a wavelength accuracy of 1 pm (0.001 nm). Therefore, the sensor C (sensitivity of 4629 nm/RIU) has a RI resolution of 2.1 E^{-7}. Similarly, the sensing resolution of sensors A and B can be calculated.

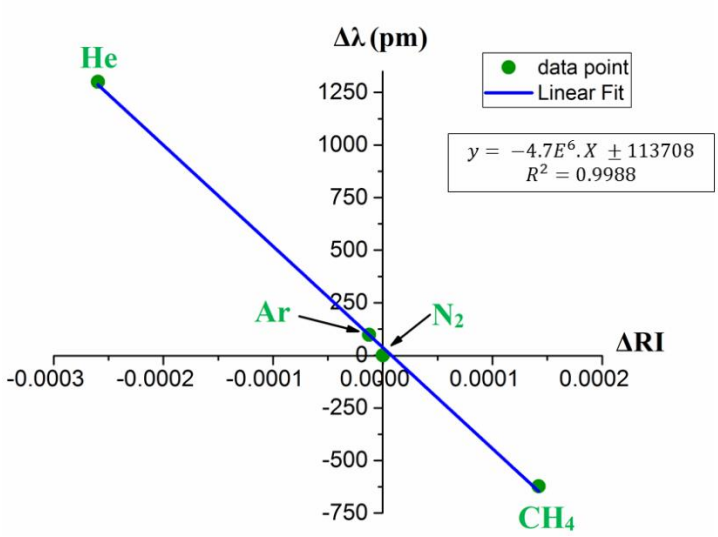

Figure 2.8 Sensitivity graph for sensor C to ambient RI change.

The refractive index of any target gas (RI target gas) can be written as:

$$\mathrm{RI}_{\text{target gas}} = \mathrm{RI}_{\mathrm{N_2}} - \Delta\mathrm{RI} = \mathrm{RI}_{\mathrm{N_2}} - \Delta\lambda/(\text{RI sensitivity}) \qquad \textbf{(Eq. 2.5)}$$

The spectral shift, Δλ in the above equation can be attained by tracking valleys of transmission fringe of a sensor, as shown in Figures 2.6 and 2.7. $\mathrm{RI}_{\mathrm{N_2}}$ is the refractive index of nitrogen, and ΔRI is the relative difference in RI between nitrogen and measurand gas. By knowing the wavelength shift (Δλ) and sensitivity of the MZI sensor, ΔRI can be calculated.

Table 2.2 compares the sensitivity achieved in the present research with other similar and alternative studies available in published works. The table shows that the proposed MZI configuration shows much higher sensitivity in gas sensing compared to its counterparts in the RI range of 1 to 1.02. As shown in [40], decreasing the length of HC-PCF, the sensitivity of this sensor can be further improved. The proposed sensor is fairly compact (3.3 mm) compared to other HC-PCF based RI sensors [31, 32, 37, 38], some of which are as long as ~35 cm. Therefore, the proposed MZI configuration is believed to perform much better in single-point gas sensing. It is worth mentioning here that even though a compact Fabry-Perot

fiber sensor (in the range of micrometer) can be fabricated using ultrafast laser micromachining they have relatively poor RI sensitivity [12]. Despite its excellent gas sensing capabilities, the reported device has few drawbacks including fabrication complexity as it requires alignment and positing of the HC-PCF stub and cross-sensitivity to other measurands such as temperature and pressure. With the recent improvement in automated fiber alignment and positing systems, we believe the fabrication complexity can be drastically reduced for commercial applications. Similar to other fiber-optic sensors, the cross-sensitivities can be eliminated or reduced using an in-line fiber sensor such as a properly packaged FBG. The demonstrated sensor also needs to be packaged with a suitable membrane for selective sensing of gasses.

Table 2.2. RI sensitivity comparison for gas sensing with other reported fiber-optic gas sensors.

Optical structure	RI range	RI sensitivity (nm/RIU)	Reference
Proposed HC-PCF MZI	1.000034–1.000449	4629	This work
HC-PCF MZI	1.0000–1.0005	1233	[37]
FP based on hollow silica tube	1.00027–1.00189	1546	[48]
	1.00007–1.00051		
SPR with metallic surface grating	1–1.41	500	[49]
(tapered SMF)			
Hybrid optical fiber Fabry-Perot (FP) interferometer	1.0005–1.00275	560	[50]
Surface plasmon resonance (SPR) based with fiber grating (MMF)	1–1.33	280	[51]
Cavity based FP	1.0000–1.0025	1053	[52]
Open cavity MZI	1–1.02	3402	[26]

2.4.2. Sensor Response and Recovery Times

Figure 2.9 illustrates the response and recovery times of Sensor A for one cycle of methane sensing. The time duration that an MZI device takes to reach 90% of the total wavelength shifts is defined as response/recovery times. Accordingly, response and recovery times of sensor A are 32 seconds and 39 seconds for methane. Response and recovery times of three HC-PCF MZI sensors to methane, helium, and argon are listed in table 2.3. Each reported time in this table is an average of five response or recovery times. Results indicate that sensor A, which has the longest HC-PCF stub, shows the fastest response/recovery times. However, the highest RI sensitivity was achieved using sensor C, which has the shortest length of HC-PCF. Response and recovery times depend on HC-PCF lengths and the volume of the test chamber. The test chamber has a dimension of 14.5 cm × 11.2 cm × 4.4 cm.

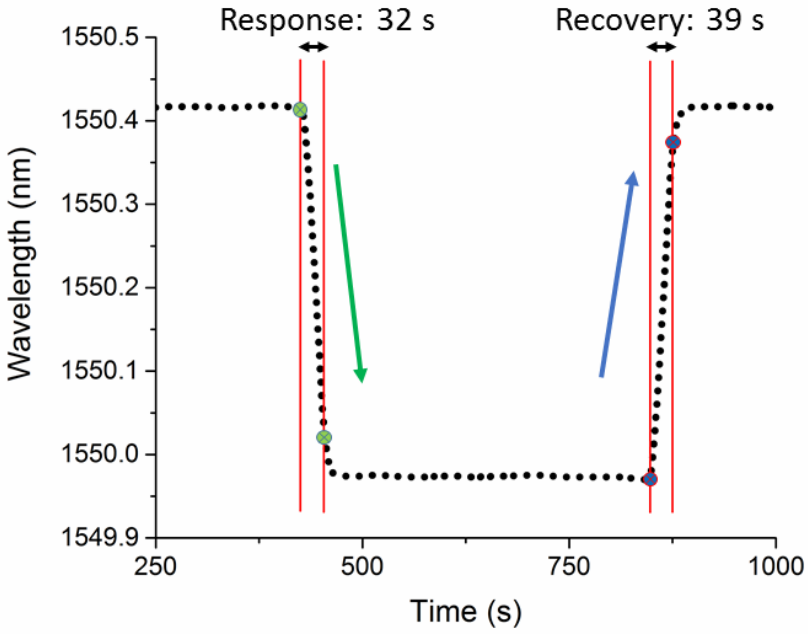

Figure 2.9 Response and recovery times of sensor A for methane.

Table 2.3. Response and recovery times of HC-PCF MZI sensors to different gases.

HC-PCF length (mm)	**A(4.97)**	**B (4.73)**	**C(3.30)**
Helium: response (s) / recovery (s)	50/50	50/55	57 / 57
Methane: response (s) / recovery (s)	32/39	44/46	46 / 56
Argon: response (s) / recovery (s)	37/44	62/49	110/ 100

2.4.3. Temperature Characterization

The RI of a gas depends not only on gas species but also on ambient temperature and pressure. All the experiments were conducted at atmospheric pressure and room temperature. However, fluctuation of ~ 1°C was recorded using an FBG sensor during the experiments, a result shown in Figure 2.6 (b). Therefore, it is required to characterize the temperature sensitivity of the HC-PCF MZI sensor before deploying the sensor for applications in the field. As part of the present research, HC-PCF sensors were placed in an oven and the temperature was varied from 35°C to 65°C in 10°C increments. Figure 2.10 displays the resulting correlation between recorded wavelength shifts and measured temperatures of the sensors and FBG. The temperature sensitivities of sensors A, B, and C were found to be 33.1 pm/°C, 31.6 pm/°C, and 20 pm/°C, respectively. This finding shows that the temperature sensitivity of the fiber-optic interferometer decreases when the length of the HC-PCF decreases. As shown in Fig. 10, a typical FBG has a temperature sensitivity of 10 pm/°C and it is insensitive to ambient RI change. Therefore, an in-line or parallel FBG can be placed as a reference to eliminate temperature cross-sensitivity in ambient RI measurement for practical applications. Like temperature, a fiber-optic pressure gauge that is insensitive to ambient RI can be used to eliminate pressure cross-sensitivity in real-life measurement.

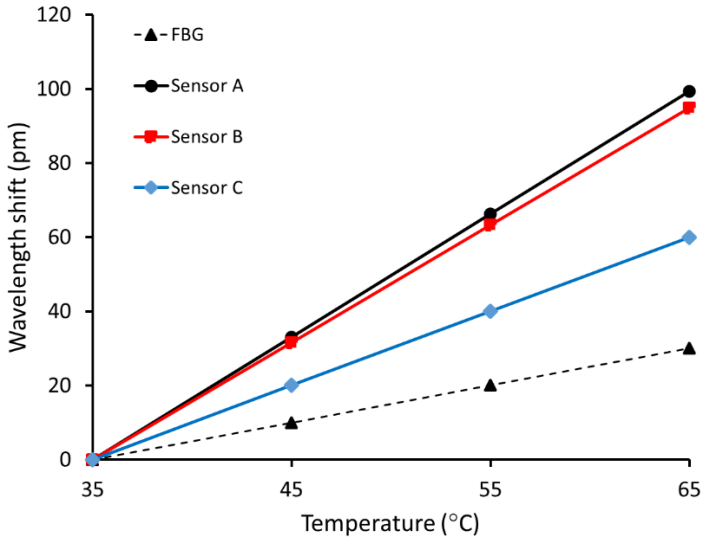

Figure 2.10 Temperature characterization of FBG and HC-PCF sensors.

2.5. Conclusion

A compact fiber-optic MZI sensor is proposed and has been experimentally demonstrated for ultra-high sensitive detection of gases. Different lengths of HC-PCF stubs were used to construct and characterize several sensors. The resulting MZI sensors were able to measure the RI of target gases and showed great sensitivity to measurand gases. The refractive index sensitivity of 4629 nm/RIU was achieved for the MZI with an HC-PCF length of 3.30 mm. The RI sensitivity of the proposed MZI sensor inversely relates to the length of the HC-PCF stub. However, response and recovery times turned out to be shorter for longer HC-PCF stubs. The effect of gap distances on the number and amplitude distribution of the sensors' modes was examined, and spatial frequency analysis revealed that power is mainly carried by two dominant modes in the proposed MZI. These novel and compact sensors have high-temperature sensitivity, compared to an FBG. With appropriate packaging, the proposed sensor becomes robust and is a suitable choice for low-percentage detection of gases as well as environmental monitoring.

Chapter 3 Monitoring of Carbon Dioxide using Hollow-Core Photonic Crystal Fiber Mach-Zehnder Interferometer

This paper was published in Journal of Sensors (MDPI) in July 2019.

Farid Ahmed, Vahid Ahsani, Kaveh Nazeri, Ehsan Marzband, Colin Bradley, Ehsan Toyserkani, and Martin B. G. Jun. "Monitoring of Carbon Dioxide using Hollow-Core Photonic Crystal Fiber Mach-Zehnder Interferometer", Sensors 2019, 19(15), 3357.

Abstract

Monitoring of greenhouse gases is essential to understand the present state and predict the future behavior of greenhouse gas emissions. Carbon dioxide (CO_2) is the greenhouse gas of most immediate concern, because of its high atmospheric concentration and long lifetime. A fiber-optic Mach-Zehnder interferometer (MZI) is proposed and demonstrated for the laboratory-scale monitoring of carbon dioxide concentration. The interferometric sensor was constructed using a small stub of hollow core photonic crystal fiber between a lead-in and lead-out standard single mode fiber with air-gaps at both interfaces. At room temperature and atmospheric pressure, the sensor shows the sensitivity of 4.3 pm/ % CO_2. The device was packaged to demonstrate the laboratory-scale leakage detection and measurement of CO_2 concentration in both subsurface and aqueous environments. The experimental study of this work reveals the great potential of the fiber-optic approach for environmental monitoring of CO_2.

3.1. Introduction

Carbon dioxide (CO_2) has been identified as the primary heat-trapping gas to adversely affect our climate between 1750 and 2011 [53]. As our planet is likely to face greater future challenges, in recent years considerable carbon mitigation research has been undertaken in an effort to fight global warming caused by CO_2. Deployment of carbon capture and storage (CCS) technologies have been proposed for a drastic reduction of CO_2 emission [54]. As of September 2012, 75 large-scale global CCS projects (at least 400,000 tonnes of CO_2 per year) and a number of projects under advanced stages of development have been identified by the Global CCS Institute [55]. While CCS has a vital role in controlling greenhouse gas emissions, CO_2 leakage at sequestration sites is the primary concern because of its adverse environmental impacts [56,57]. Research models predict that in an event of leakage, CO_2 escape rate above 0.1% may jeopardize the effectiveness of a geological storage site [58]. Hence, early detection of CO_2 leakage is essential to re-establish the efficiency of a CCS operation and minimize its ecological damages. Monitoring of CO_2 leakage has been investigated using diverse approaches including seismic [59], geoelectrical [60], geochemical [61], gravimetric [62], temperature logs [63], and soil gas composition [64]. There are many challenges inherent to monitoring a CCS project, most notably: prolong periods (i.e., several decades), long transmission lengths, extreme physical and chemical conditions, and capital and operating costs. Most of the techniques mentioned above have a low sensing resolution or do not meet the challenges associated with monitoring CCS projects.

Fiber-optic sensors have unique properties that make them ideal for CCS site monitoring, for example: compact size, immunity to electromagnetic radiation, superior aging characteristics, long-haul monitoring capabilities, and the ability for high-resolution CO_2 detection. Fiber-optic sensors are very efficient in gas detection and monitoring applications [65–67] as compared to conventional sensors. Various fiber-optic sensor configurations have been exploited for monitoring CO_2 concentration including long period grating [68], Bragg grating [69], evanescent filed [70], and fluorescent based [71,72]. Fiber fluorescence sensor has also been employed to demonstrate monitoring of environmental CO_2 [73]. Use of fluorescent dyes, nanoparticle coatings, or extensive etching of the fibers in the reported studies likely to affect aging behavior and robustness of the sensors. There has been a constant effort to develop highly sensitive all-fiber sensors using suitable fiber type and device configuration [65,66,74]. The evanescent field in the cladding air holes of photonic crystal fibers reveals new opportunities to exploit light interaction with gasses for sensing applications [75,76]. Hollow core photonic crystal fibers (HPCF) have air holes running along the fiber propagation axis in both the core and cladding regions. These structures have been introduced to improve the light interaction with the sample gas leading to superior sensitivity [77,78]. Various mechanisms have been explored for HPCF based gas sensing including tuneable modal interference [79], Fabry–Pérot interference [80], photo-thermal phase modulation [81], surface-enhanced Raman scattering [82], and a gas absorption spectroscopy in HPCF [77,83]. However, these sensing devices require an extended length of HPCF, drilling side micro-holes on HPCF, or filling the air holes of HPCF with Raman scattering substrate such as nanoparticle colloids. The reported fiber-optic

gas sensors to date either display insufficient sensitivity/reliability or require complex fabrication and/or packaging processes.

In this study, a hollow core photonic crystal fiber (HC-PCF) based Mach-Zehnder (MZI) sensor is proposed for the detection and measurement of CO_2 concentration in subsurface soil and aqueous environments. As shown in Figure 3.1, the device was fabricated by placing a small stub of HC-PCF between a lead-in and lead-out standard single mode fiber (SMF) with air gaps at both interfaces. The air holes in HC-PCF provide a large area of interaction with the gas leading to high-sensitive detection and measurement of CO_2.

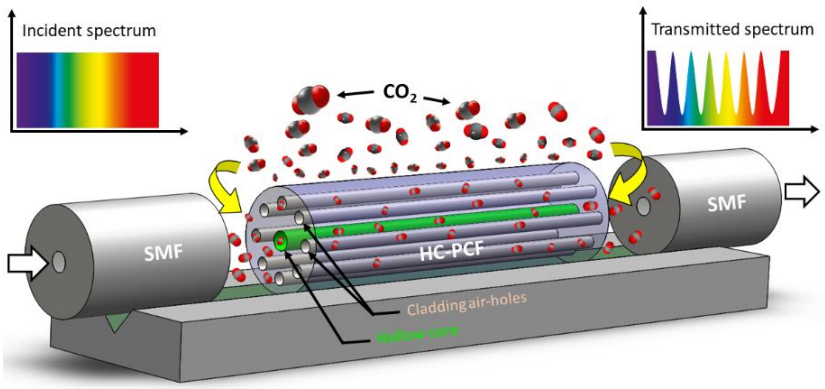

Figure 3.1 Schematic of the MZI sensor constructed using a small stub of HC-PCF.

3.2. Working Principle

The schematic of the sensor configuration is shown in Figure 3.2. It is a common MZI structure where the fringe pattern appears at the transmission end because of interference between the core mode and dominant cladding mode. The transmission fringe of a fiber-optic MZI can be expressed as [84,85]:

$$I = I_{core} + I_{clad} + 2\sqrt{I_{core} I_{clad}} cos\phi, \qquad \textbf{(Eq. 3.1)}$$

where I_{core} and I_{clad} are the intensities of light in the core and cladding, respectively. The phase difference between core and cladding mode can be expressed as $\phi = 2\pi\Delta n_{eff}L/\lambda$, where n_{eff} is the difference of effective refractive indices between core and cladding modes, L is the length of the MZI, and λ is the wavelength. For $\phi = (2m + 1)\pi$ in Eq. (6), the m^{th} order attenuation peak is maximum and its associated wavelength can be expressed as $\lambda_m = 2\Delta n_{eff}L/(2m + 1)$. Therefore, any change in Δn_{eff} or L due to an ambient refractive index or temperature variation results in a shift of attenuation peak. Such spectral shifts can be utilized to measure the ambient gas concentration.

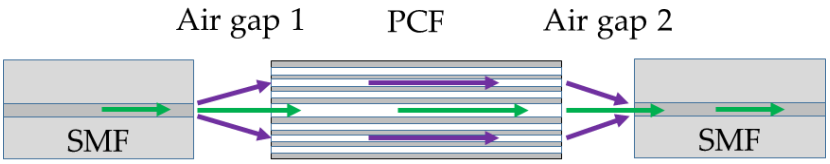

Figure 3.2 Working principle based on geometric light propagation in the fiber assembly.

3.3. Sensor Fabrication and Packaging

As shown in Figure 3.1, SMF (Corning SMF28) and HC-PCF (NKT Photonics HC-PCF 1550) were used to fabricate the sensor. The small stub of HC-PCF was placed between a lead-in and lead-out SMFs with suitable air gaps at both interfaces The fiber assembly was first aligned and fixed on V-groove of a glass slide (25 mm × 5 mm × 1 mm) using a waterproof adhesive. Suitable packaging of a fiber-optic sensor is crucial for its reliable sensing operation and longer life span. Therefore, the device was packaged to make it operational in the subsurface and aqueous environment. Figures 3.3 (a) and (b) show the schematic of the packaged configuration, and the steps involved in packaging the sensor, respectively. The glass slide holding the fiber assembly was first secured in a stainless steel

mesh tube to provide mechanical strength to the fiber assembly and allow easy handling of the device. The sensor was then wrapped with two water-impermeable membranes that allow gas flow in the chamber. The scanning electron microscope (SEM) images shown in Figure 3.4 reveal the morphologies of both front and rear surfaces of the inner (TRAKETCH, Sabeu-Plastics, and Membrane Technology, Germany) and outer (SQ-S GASKET SHEET, Inertech Inc., USA) membranes. Figures 3.4 (a), (b), and (c) show the front, rear, and magnified images of TRAKETCH membrane capturing both surfaces, respectively. The capillary pores (pore size: 1.37 ±0.02 µm, pore density: ~13.7 $\times 10^6$ / cm^2, thickness: 170 ± 20 µm, water entry pressure ≥ 0.6 bar) of this micro filtration membrane work as hydrophobic surface and allow CO_2 gas flow. Figures 3.4 (e), (f), and (g) show the front, rear, and magnified surfaces of the INERTEX SQ-S membrane. The gasket sheet is made of polytetrafluoroethylene (PTFE) that can operate in full vacuum to 200-bar pressure and it does not support any bacterial growth. The two membranes were assembled to achieve a good balance of CO_2 permeability and water resistance. To protect the device from dirt and dripping water, it was finally wrapped with Tyvek, a commercially available building water insulation membrane.

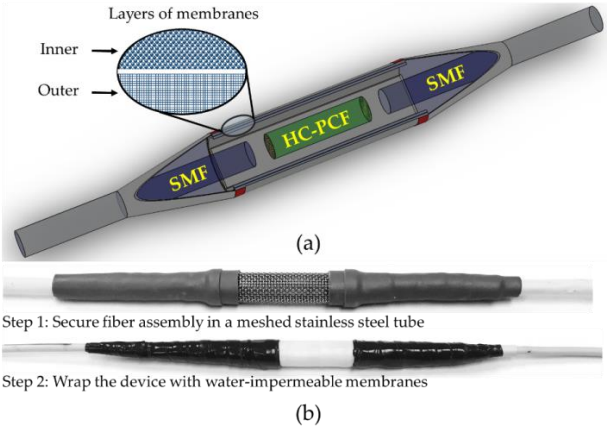

Figure 3.3 (a) Schematic of packaging, and (b) sensor packaging.

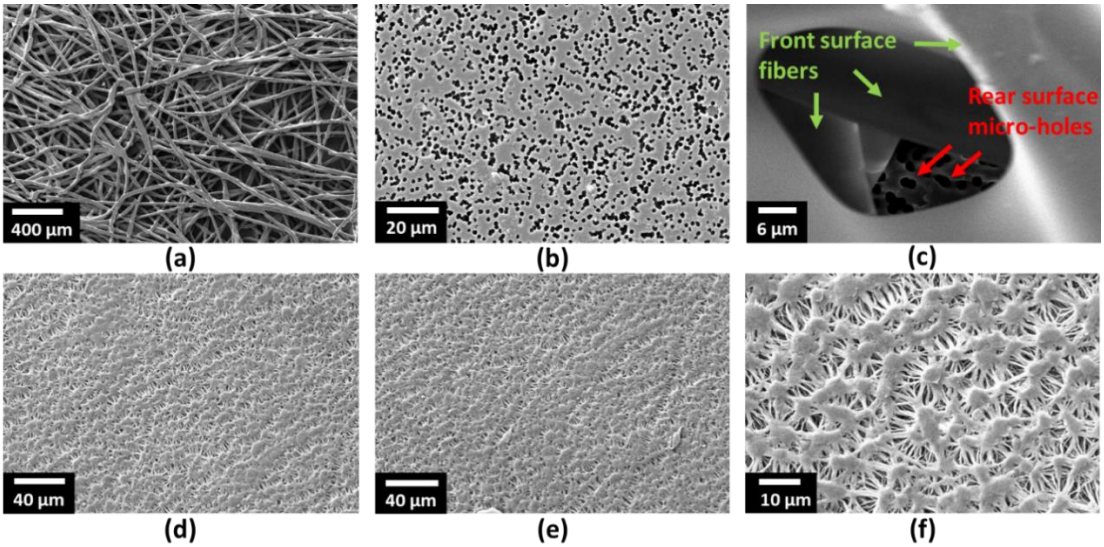

Figure 3.4 SEM images of the two membranes used in packaging of the sensor to make it waterproof: (a) front surface of the inner membrane, (b) rear surface of the inner membrane, (c) magnified image of the inner membrane showing both fibers and microholes on two surfaces, (d) front surface of the outer membrane, (e) rear surface of the outer membrane, and (f) the magnified image if the outer membrane.

3.4. Results and Discussion

3.4.1. Sensor Characterization

The schematic shown in Figure 3.5 was used to characterize CO_2 concentration in near atmospheric pressure. The dimension of the test chamber used in this experiment is 14.5 cm × 11.2 cm × 4.4 cm. The sensor was interrogated with different known concentrations (25%, 50%, 75%, and 100%) of CO_2 gases. 99.99% pure nitrogen (N_2) was used as a reference gas and the discharge tube with a bubbler was used to keep near atmospheric pressure in the test chamber. A circulator was used to connect the MZI sensor to the Micron Optics interrogator (SM125). The chamber was also equipped with a fiber Bragg grating (FBG) to monitor any temperature variation during the experiments. As shown in Figure 3.6 (a), the sensor shows a consistent trend of shifts as it is subjected to different concentration of CO_2 gas. The sensor has a sensitivity of 4.33 pm/ % CO_2, which is very promising.

Considering the sensitivity of the sensor and wavelength stability of the interrogator (1 pm), it exhibits a measurement resolution of ~ 0.2% CO_2. Figure 3.6 (b) shows the sensor response to the ambient temperature change in the range of 25 ˚C to 65 ˚C. The sensor shows a linear spectral shift with temperature change with a sensitivity of 31.67 pm/ ˚C.

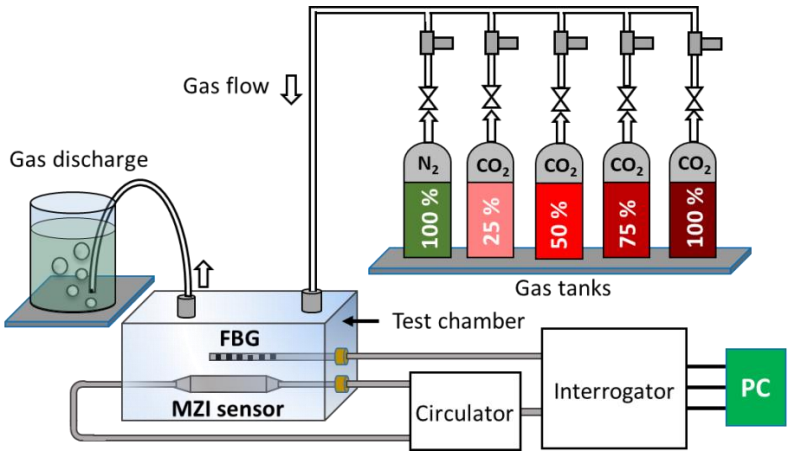

Figure 3.5 Experimental schematic for sensor characterization and interrogation.

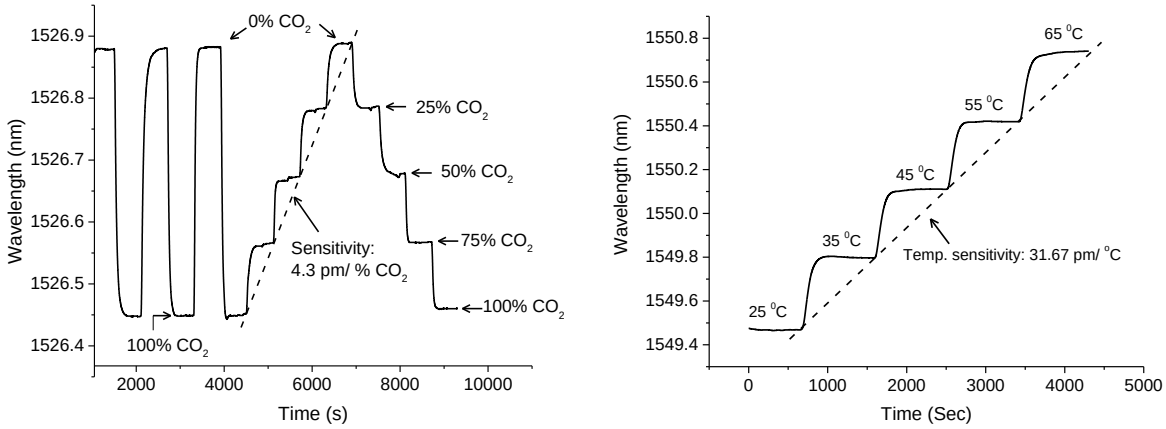

(a) (b)

Figure 3.6 The response of the sensor to (a) CO_2 concentration, and (b) temperature change.

Reliable operation is essential in any sensing application. Hence, repeatable sensing capability is crucial in particular for effective gas monitoring applications. To examine the sensing reliability of the device, a cyclic test was performed for four different known concentrations of CO_2 gasses such as 25% CO_2, 50% CO_2, 75% CO_2 and 100 % CO_2 as

shown in Figure 3.7. Nitrogen was used as a reference gas for this test. The cyclic test started with injecting atmospheric N_2 gas into the test chamber for 10 minutes. Once the injection of N_2 stopped, the 25% CO_2 gas was injected into the chamber for 10 minutes. This two-step process was repeated two more times to finish the cyclic test for 25% CO_2. For the higher concentration of CO_2 gases, the same two-step process was repeated three times. An FBG sensor with a temperature sensitivity of 10 pm/ $^{\circ}$C was placed in the test chamber to monitor any temperature change during this experiment. The sensor shows good repeatability in the measurement of CO_2 concentration. A maximum of 40 pm spectral deviation was observed for the entire experiment as shown in Figure 3.7, which is largely because of temperature change in the chamber. The FBG shows 1°C increase of temperature (that corresponds to 10 pm FBG spectral shift) in the test chamber by the end of the experiment. Since the temperature sensitivity of the proposed MZI sensor (31.67 pm/ $^{\circ}$C) is about three times more than that of FBG (10 pm/ $^{\circ}$C), ~ 32 pm spectral shift appeared due to 1°C temperature raise in the test chamber. The remaining 8 pm spectral shift may appear due to a pressure change in the chamber or measurement errors. The sensor showed good measurement repeatability as shown in Figure 3.7.

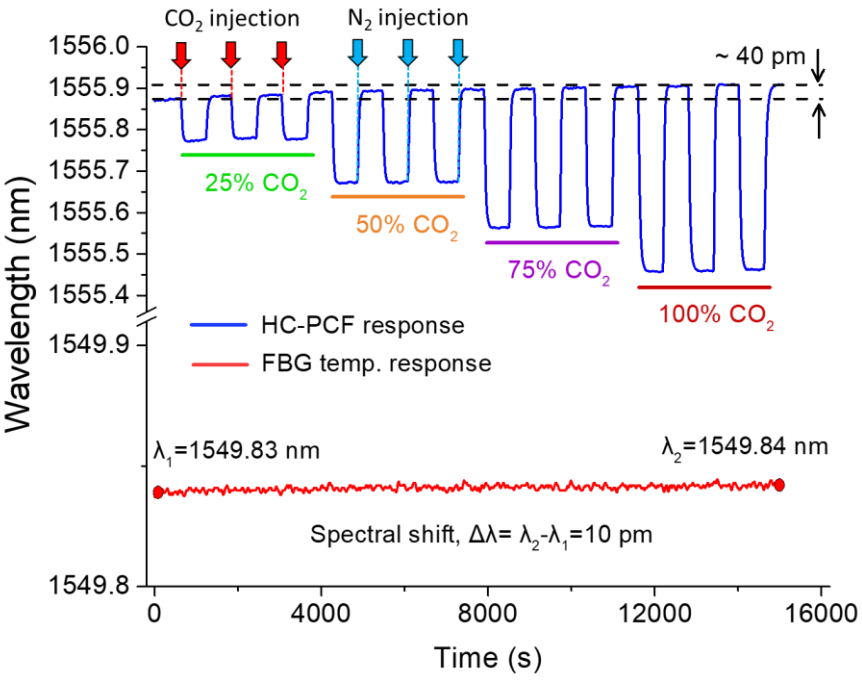

Figure 3.7 Cyclic test to examine the measurement reliability of the gas sensor.

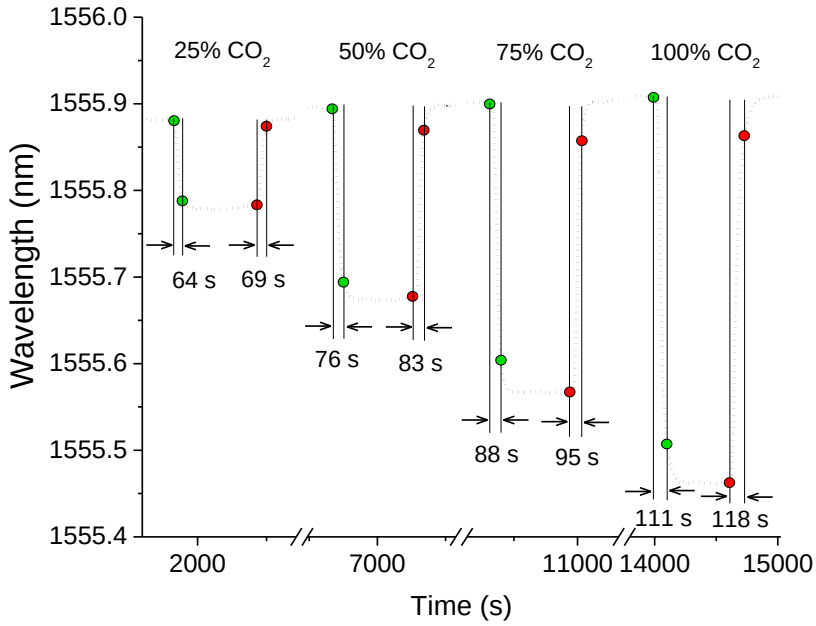

Figure 3.8 Response and recovery times of the sensor for different concentration of CO_2 gases.

Response and recovery times are widely used to characterize gas sensors, which are essentially the times taken by a sensor to reach 90% of final and initial indications, respectively. For the given test chamber, Figure 3.8 reports the response and recover times

for four different concentration of CO_2 gases. The response times of the sensor for 25%, 50%, 75%, and 100% CO_2 are 64 s, 76 s, 88 s, and 111 s, respectively. The recovery times of the sensor for 25%, 50%, 75%, and 100% CO_2 are 69 s, 83 s, 95 s, and 118 s, respectively. Since the sensor sits on the floor of the test chamber and the CO_2 gases used in this experiment are heavier than the reference gas (N_2), response times are shorter than the recovery times. The main limiting factor for both response and recovery times is the delivery of gasses to the air gaps and air holes. Therefore, both the response and recovery times can be improved by reducing the volume of the test chamber.

3.4.2. Subsurface CO_2 Measurement

The sensor was tested to measure CO_2 concentration in soil column in room temperature and atmospheric pressure. As shown in the schematic of Figure 3.9 (a), the sensor was buried 20 cm under the 50 cm deep soil column. The radius and height of the cylindrical soil column are 30 cm and 60 cm, respectively. The CO_2 and N_2 were injected into the soil column from the bottom. The transmission spectrum of the interferometer was first monitored for 10 min in the air, followed by injection of N_2 for the next 10 min as shown in Figure 3.9 (b). The 100% CO_2 was then injected into the soil column for 10 min followed by injecting reference N_2 gas for another 10 min. The percentage of CO_2 injection was then gradually increased up to 100% as shown in Figure 3.9 (b). A reverse trend was then followed to return the sensor spectrum to the initial level. The 100% CO_2 gas was then injected for 10 min for the last time followed by injection of the reference gas. The purpose of this test was to understand the response of the sensor in the sub-surface environment. With a larger surface area of the soil column exposed to the atmosphere and increased volume of

sensing environment, the sensor shows longer response and recovery times (with reference to Figure 3.6 (a). At the end of the experiment, the overall spectrum also followed a red shift, which may be attributed to the rise in temperature as noticed in Figure 3.7.

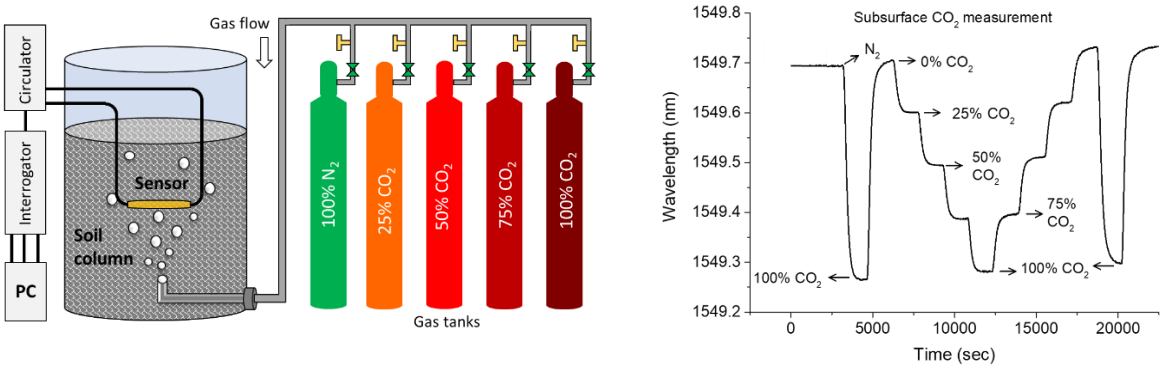

(a) (b)

Figure 3.9 (a) Laboratory setup for CO_2 concentration measurement in soil, and (b) Measurement of CO_2 concentrations in soil (at atmospheric pressure and room temperature).

3.4.3. Aqueous CO_2 Measurement

Figure 3.10 (a) shows the experimental setup for the measurement of CO_2 concentration in an aqueous environment. To investigate the performance of sensors that are packaged using water-resistant membranes, the sensor was first immersed in water for 24 hours and its transmission spectrum was recorded for every 12 hours. As shown in Figure 3.10 (b), the spectrum of the sensor did not show any significant degradation over the period of 24 hours, except a small spectral shift which is likely due to temperature change during the experiment.

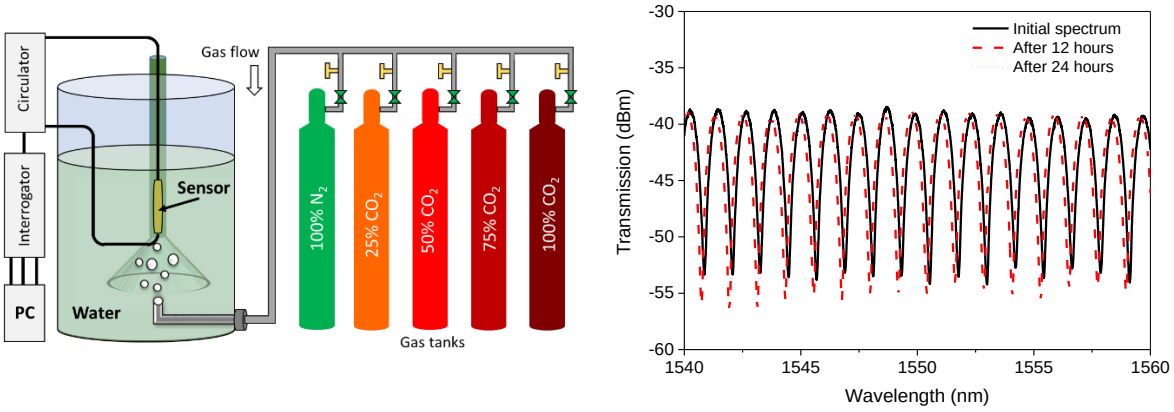

(a) (b)

Figure 3.10 (a) Setup for CO_2 concentration measurement in an aqueous environment, and (b) spectral stability in water for 24 hours.

A funnel was used for guiding the CO_2 bubbles to the sensor vicinity that helps the diffusion of gas into the packaged sensor. The response of the sensor to CO_2 concentration changes in the aqueous environment is shown in Figure 3.11 (a). Each of the 25%, 50%, 75%, and 100% CO_2 gases was successively injected for 30 min. The sensor shows spectral blue shifts with a gradual increase in CO_2 concentration. Unlike the experiments in the test chamber or soil column, the sensor showed irregular spectral shifts, which may appear due to the turbulence created by the CO_2 bubbles. Once immersed in the water, the ambient humidity was considered stable during the experiment. Detail effects of humidity in the aqueous environment will be conducted in the future which may also explain the anomalies in the spectral shift during the experiment. After injecting 100% CO_2 for 30 min, the injection was stopped to let CO_2 gradually diffuse out of the packaged sensor. As shown in Figure 3.11 (b), diffusion of CO_2 out of the packaged sensor is very slow. An injection of reference gas to the sensing chamber may significantly improve the recovery time for such monitoring applications.

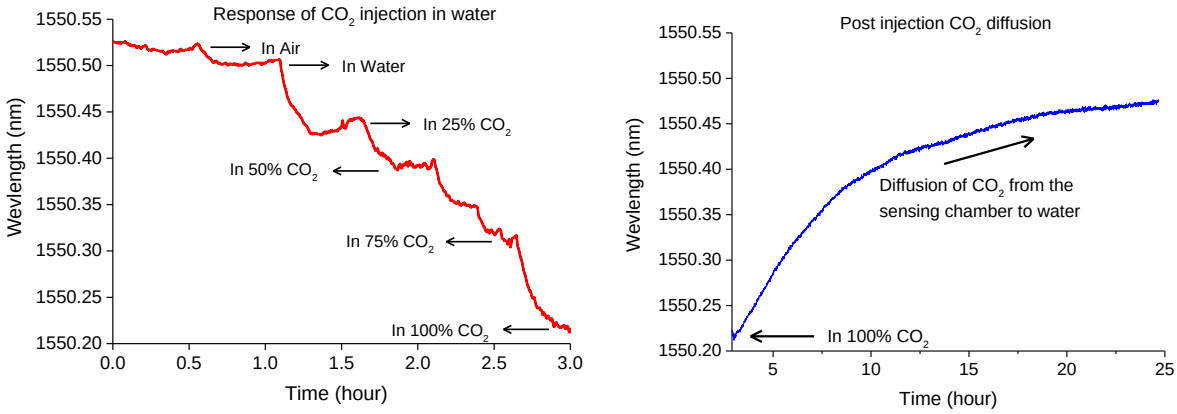

(a) (b)

Figure 3.11 (a) The response of the sensor to different concentrations of CO_2 in water, and (b) tracking slow diffusion of CO_2 gas when injection stopped.

3.5. Conclusion

In this study, an HC-PCF based MZI is introduced that can measure ambient CO_2 concentration for environmental monitoring applications. The device was constructed by placing a stub of HC-PCF between a lead-in and lead-out SMF. The sensor was packaged and characterized for known concentrations of CO_2 gases. At room temperature and atmospheric pressure, the sensor shows a linear response to CO_2 concentration with the sensitivity of 4.3 pm/ % CO_2. Considering the measurement device used in this study has wavelength stability of 1 pm, the resolution of the sensor is ~0.2% CO_2. For the test chamber dimension of 14.5 cm × 11.2 cm × 4.4 cm, the sensor shows fast response and recovery times of 64 s, and 69 s, respectively. Water-resistant but gas permeable membranes were used to package the sensor. The sensing device demonstrated the laboratory-scale leakage detection and measurement of CO_2 concentration in both subsurface and aqueous environments. The sensor showed a stable and reliable measurement of CO_2 concentrations with a considerably short response and recovery times. The experimental study of this work reveals the potential of the fiber-optic approach for environmental monitoring of CO_2 leakage and concentration.

Chapter 4 The Effect of Photonic Crystal Fibre Structure on the Performance of Mach-Zehnder Interferometer Fibre Optic Gas Sensors

This paper was published in Journal of Optical Fiber Technology in June 2020.

Kaveh Nazeri, and Colin Bradley. "The Effect of Photonic Crystal Fiber Structure on the Performance of Mach-Zehnder Interferometer Fiber-Optic Gas Sensors", Optical Fiber Technology 58 (2020), 102294.

Abstract

A compact refractive index (RI) sensor, based on the Mach-Zehnder Interferometer (MZI), has been developed and experimentally evaluated for the highly sensitive detection and quantification of gases (helium, methane, and carbon dioxide). The RI sensor utilizes a variety of fibre types: Single Mode Fibre (SMF), Photonic Crystal Fibre (PCF), and Hollow-Core Photonic Crystal Fibre (HC-PCF). In order to fabricate the MZI sensors, a short length of sensing fibre was positioned between a lead-in and a lead-out single mode fibre (SMF) with an air gap at each interface. Three types of sensors were fabricated using this configuration employing 4 mm stub of (i) PCF, (ii) 10 μm HC-PCF, and (iii) 20 μm HC-PCF as the sensing elements. The performance of these sensors we compared for detecting and measuring the quantity of gas present. The transmission spectrum of MZI sensors are formed by interference between the cladding and core modes. These transmission signals correspond to the frequency components in the sensor's Fast Fourier Transform (FFT) spectrum. The effect of gap distance on the number and amplitude distribution of the modes was examined in an effort to optimize the design elements. The resulting fiber sensors can measure the RI of a gas-filled cavity and they showed high-sensitivity to helium, methane, and carbon dioxide. The highest RI sensitivity of 3210 nm/RIU was demonstrated in the RI range of

1.0000347-to-1.000449 by a sensor with a 4 mm long sensing stub element of 10 µm HC-PCF. Cyclic tests with the group of gases demonstrated that the measurements are highly repeatable. The measurement response and recovery times for all sensors were determined, and it was concluded that the 20 µm HC-PCF sensor has the fastest response/recovery time and the PCF sensor has the slowest. This research illustrates that the sensors fabricated by the proposed method have potential for improving the ability to detect and quantify pure gases. Additionally, the sensors are highly sensitive to low percentages of CO_2, making them suitable for greenhouse gas measurement.

4.1. Introduction

Properties of fiber-optic sensors make them a superior choice for environmental monitoring applications, particularly when compared against conventional electro-optical sensors [86, 87]. Their advantageous properties include multifunctional sensing capabilities (such as temperature, pressure, strain, and corrosion), immunity to electromagnetic radiation, and high sensitivity [86, 88, 89]. Sensing mechanisms such as evanescent field absorption, direct absorption, surface Plasmon resonance, and Raman scattering are among numerous fabrication methods that have been studied [90-95]. Resulting sensors have relied on different types of optical fibers, such as single mode fiber (SMF), photonic crystal fiber (PCF), and micro-structured fibers. Moreover, micro and nanostructured materials have been widely used to measure chemical entities, mostly by deposition of a material or polymer that is sensitive to a specific parameter on the fibre [96]. Thus, the light guidance is altered by changes in its optical properties. Several applications for detection of volatile organic compounds [97], gas sensing [98], and pH measuring [99] have been reported using this

method. Nanostructured polymeric coatings such as nanoparticles, luminescent materials, and metal oxide particles can enhance chemical, physical, or optical properties of fibers in comparison with bulk material fibers [100]. It is been reported that implementation of sensitive coatings onto optical fibers can enhance some characteristics of a sensor like sensitivity and selectivity [100].

In addition to silica optical fibers, polymer optical fibers (POF) are well in use for fabrication of sensors in several sensing applications like strain [101], curvature [102], humidity [103], and temperature [104]. Advantages of POFs over silica fiber include higher flexibility in bending, higher fracture toughness [105], and higher thermo-optic coefficient [106]. It should be noted that POF materials are viscoelastic, which lead to non-uniform results to strain or stress [107]. Various sensors have been developed and studied using POF, including Fiber Bragg Grating (FBG) inscription in POFs [105, 107-109], and Long Period Gratings in microstructured POFs [110, 111]. High stability, as well as minor variations in bandwidth and reflectivity are among the advantages of these sensors [105]. In the area of gas sensing, Saharudin et al. [112] used different oxygen sensitive nanomaterial to coat one end of optical fiber to evaluate the performance of sensors. Evaluation of the effect of sol-gel coated length on POF core is described by Zolkapli et al. [113] to improve oxygen gas sensitivity.

Further to previously mentioned methods, numerous types of optical fiber interferometers have been studied, including the Sagnac, Michelson, extrinsic/intrinsic Fabry-Perot, and Mach-Zehnder interferometers. Domingues et al. [114] developed an intrinsic Fabry-Perot interferometer (FP) micro-cavity for pressure sensing. They achieved

the sensitivity of 59.39 ± 1.7 pm/Kpa for pressures up to 900kPa, using a FP interferometer with micro-cavity length of 21.86 μm. As the cavity's physical parameters can induce phase shift on the FP interferometer signal, these sensors can be used to monitor pressure, temperature, strain, and refractive index. The hybrid FP engineered by R.Wang [115] simultaneously monitors RI change and temperature fluctuations, but has relatively low sensitivity in the RI range of 1.005-1.00275. A hybrid interferometer was proposed by Sun et al. [116] by forming a Fabry-Perot cavity in one of the optical paths of a Michelson interferometer. Consequently, two distinctive interference fringes on the spectral response were formed. The simultaneous measurement of temperature and RI revealed temperature sensitivity of 13 pm/°C and resolution of 8.7 E^{-4} in the RI range of 1.33 – 1.38. Jia et al. [117] developed a temperature compensated FP sensor for humidity monitoring and gas concentration analysis, using a hollow silica tube (HST) with inner diameter of 5 μm. Liu et al. [118] developed a photonic crystal fiber Sagnac interferometer by filling the central holes of the fiber with microfluidic analytes. Although high sensitivity and resolution was achieved, but filling the air holes of fiber is complicated. Among different types of interferometers, MZIs have received significant attention, because they are robust, compact, and have high levels of precision [119].

A typical fibre-optic MZI sensor configuration has a sensing arm and a reference arm as well as a splitter that divides incident light into these arms. Light propagating in the two resulting paths is recombined by a coupler. The sensors developed in this research field have employed techniques such as mismatch splicing [120], cladding collapse [121], and hollow-core fiber splicing [122]. The configuration of in-line MZI sensors is composed of two

contact arms within the fiber formed by using different optical fibres. This includes long-period gratings (LPGs), microfibers, and tapered fibers [123-127]. The configuration of a PCF-MZI sensor can be similar to an in-line MZI sensor. By splicing a piece of PCF between two SMFs, collapsed regions are inevitably formed at both ends of the PCF. These regions play the role of splitter or coupler [128]. PCFs have solid core and periodically spaced air holes in the cladding. This provides them with unique properties of high transmission [129], low background noise [130], and tailored dispersion [131]. Hollow-Core PCF (HC-PCF) has a hollow core surrounded by a cladding that also contains air holes. The fundamental mode in HC-PCF has a quasi-Gaussian intensity distribution [132]. Air holes in the fibre enable gas sensing, as it provides the interaction between the propagated light and the gas molecules in the sensing region.

Using HC-PCF as an apparatus for gas detection was proposed in 1999 and many optical devices have subsequently been fabricated [133]. Such gas sensors were fabricated either by splicing HC-PCF to another fiber such as SMF, or without splicing using a variety of fiber connectors [134]. Fusion splicing of HC-PCF to SMF is more difficult to produce than splicing PCF to SMF, because of the presence of a hollow-core, which contains a much larger volume of air that tends to expand during splicing, thereby distorting the fibre structure. Butt coupling in opposite is a method to fabricate PCF-MZI sensors without splicing, in which a gap is created between the lead-in sensing element and lead-out fibers. The length of this gap can be controlled in the assembly process and the gap allows light coupling between the SMF and PCF elements. Due to the mode field diameter (MFD) mismatch between SMF and HC-PCF, the propagation of SMF fundamental mode into the

hollow-core fiber will excite the fundamental mode and weaker higher-order modes [134]. As it may take time for gas molecules to fully permeate the HCF-PCF cavities, the fabrication of micro-channels on the cladding of the HC-PCF, employing either femtosecond laser or Focused Ion Beam machining, has been suggested as a means to accelerate the gas diffusion [135-137].

In this study, which is a continuation of a recent article by Nazeri et al. [138], an in-line fiber-optic MZI sensor using both PCF and HC-PCF fibres is presented. The working principle of the sensor and the method of light propagation inside the gap-based gas sensor are discussed below. Important performance parameters for three types of fiber-optic MZI sensors are presented: namely, their RI sensitivities, response and recovery times, as well as the number and power distribution of modes. Relative RI detection was employed in this work due to difficulty in achieving high accuracy RI measurements in absolute RI detection [139]. The experimental results of the sensors' RI sensitivity to helium, methane, carbon dioxide, and argon are presented. Nitrogen (99.99% purity, at 18 psi) with an RI of 1.0002944 was employed as the control reference for RI characterization. The sensors showed great repeatability in their sensitivities. Moreover, given the complications of ambient RI measurement, the effect of temperature cross-sensitivity has been addressed due to the fact that the RI of most gases is a function of temperature.

4.2. Working Principle

Figure 4.1 (a) presents a schematic illustration of the proposed sensor configuration. In this arrangement, a short piece of sensing element fiber (4 mm) was placed between two SMFs with gaps at both ends. The incoming single mode light wave enters through the lead-

in SMF. Upon reaching the first sensor gap, it radiates from the SMF core, illuminating the solid/hollow-core and the cladding air holes of the sensing element. The SMF core acts as a pseudo-point light source, and the rapidly diverging beam excites the fundamental mode and higher-order modes propagating in the circular channels of the sensing element. Interaction between the propagating light and the gas molecules takes place along the length of the sensing element fiber. Optical interference occurs at the second gap due to the phase difference between the fundamental and higher-order modes. The SMF, positioned at the transmission end of the sensor, then transfers the interference spectrum to the spectrum analyzer. The device's reference and sensing arms are both in contact with gas molecules; however, the effect of RI change on the interference in the sensing arm is higher than in the reference arm. That imbalance occurs due to differences in optical-path lengths between the arms. The central solid-core of the PCF and hollow-core of HC-PCF act as the reference arm of the MZI, and the cladding air channels act as its sensing arms. The light guiding mechanisms in photonic crystal fibers are different from the total internal reflection phenomenon that occurs in typical fibers [116]. Generally, photonic crystal fibres support several higher-order core modes and sometimes additional surface modes that are located on the core-cladding boundary [108]. HC-PCF provides a remarkably strong interaction between light particles and gas molecules due to high optical field confinement [117]. Figure 4.1 (b) shows a schematic diagram of the light transmission, Optical Path Length (OPL) differences, and theoretical phase shifts in an MZI with a 4 mm long, 10 μm HC-PCF stub as the sensing element and 1mm gap at each end. Theoretical phase shifts are calculated using equation 4.2.

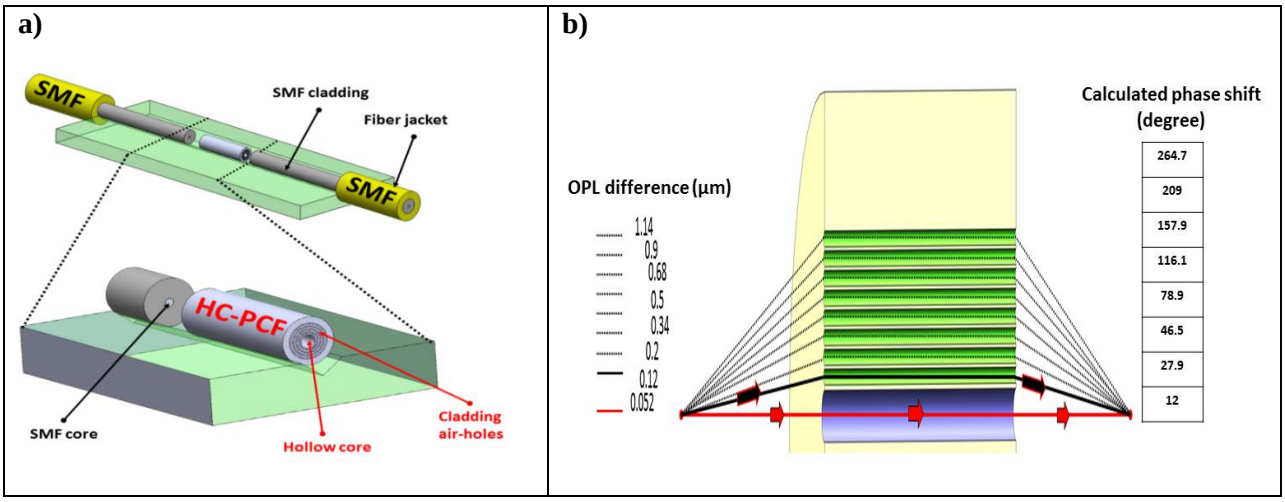

Figure 4.1 (a) Schematic illustration of the proposed sensor arrangement, (b) Schematic of light transmission and OPL differences for an MZI with 4 mm length of 10 μm HC-PCF as sensing element, and gap length of 1 mm at each end.

The fiber-optic MZI sensor's interference spectrum depends on the difference in optical path length between the light propagating in the sensing arm and in the reference arm. The interference between core and cladding modes can be written as a function of the phase difference (ϕ), core intensity (I_{core}), and cladding intensity ($I_{cladding}$) [114, 118, 119] as:

$$I = I_{core} + I_{cladding} + 2\sqrt{I_{core} I_{cladding}} \cos \emptyset \quad \textbf{(Eq. 4.1)}$$

The phase difference ($\Delta\phi$) between the two modes traveling the same distance (L) can be written as:

$$\Delta\phi = 2\pi(\Delta n_{eff})L\,\lambda^{-1} \qquad \textbf{(Eq. 4.2)}$$

where λ is the input wavelength, Δn_{eff} is the difference in the effective RI between the core and cladding modes, and L is the path length of the sensing element fiber. Considering 'm' as an integer, maximum transmission happens when $\Delta\Phi = 2\pi m$ and peaks at the following wavelength on the transmission signal:

$$\lambda_m = (\Delta n_{eff})L\,m^{-1} \qquad \textbf{(Eq. 4.3)}$$

Consequently, the m-order shift of the interference spectrum is given by the following form:

$$\Delta\lambda_m = (\Delta n_{eff} + \Delta n)L\, m^{-1} - \Delta n_{eff}\, m^{-1} = \Delta nL\, m^{-1} \quad \textbf{(Eq. 4.4)}$$

Since the length of the PCF/HC-PCF (L) is constant in equation 4.4, then any change in the RI of core and cladding of the MZI will change Δn, and correspondingly $\Delta\lambda_m$. As a result, a change will occur in the outgoing spectrum due to optical interference, which depends on the OPL difference of light in the MZI's reference and sensing arms.

4.3. Sensor Fabrication

The first step in the fabrication of fiber-optic MZI sensors consisted of using a femto-second laser to micro-machine a V-groove, having a width of 90 microns and depth of 50 microns, along a length of 25 mm microscope slide. The sensors were constructed on the slide, and the groove was used to position and align the lead-in SMF, lead-out SMF, and sensing element fibre. The sensing element fibres include 4 mm of either PCF or HC-PCFs, and flat surfaces were cleaved onto both ends of the fiber sensing element. Their exact length was ensured by verification under an optical tooling microscope. The sensing element was then positioned in the middle of the lasered V-groove and fixed on the microscope slide using epoxy glue. Subsequently, the lead-in and lead-out SMFs were positioned in fibre holders, mounted on linear-translation stages, and then were aligned with the sensing element fibre and the V-groove. A top view of the fabrication setup is shown in Figure 4.2 (a). Gap distances were accurately adjusted to control mode splitting/recombination and to achieve a strong interference spectrum. Once an acceptable interference pattern was achieved, the fibre pieces were permanently glued to the glass slide.

Three sensor types were fabricated for evaluation purposes using the above manufacturing process. All three sensor types utilised corning single mode (SMF28) lead-in

and lead-out fibres that have a numerical aperture (NA) of 0.13, mode field diameter (MFD) of 9.3 µm (±0.5 µm), and a core diameter of 8.2 µm. Specifications of the sensor types (A, B, and C) are provided below:

Sensor Type – A

This sensor type utilizes a 4.00 mm (±0.15 mm) long NKT Photonics HC-PCF (HC-PCF 1550) fiber as the sensing element. The HC-PCF fiber has a numerical aperture (NA) of 0.2, mode field diameter (MFD) of 9.00 µm (±1 µm), and core diameter of 10.00 µm. This sensing fiber element also has cladding air holes of 3.10 µm in diameter and a cladding pitch of 3.80 µm. The fiber has a narrow wavelength transmission window of 1490-to-1680 nm that supports several guided modes in this band.

Sensor Type – B

This sensor type utilizes a 4.00 mm (±0.15 mm) long Thorlabs HC19-PCF fiber as the sensing element. The HC-PCF fiber has a numerical aperture (NA) of 0.13, mode field diameter (MFD) of 13.00 µm (±2 µm), and core diameter of 20.00 µm. This sensing fiber element also has cladding air holes of 3.10 µm in diameter and a cladding pitch of 3.80 µm. The fiber has a narrow wavelength transmission window of 1490–1680 nm that supports several guided modes in this band.

Sensor Type – C

This sensor type utilizes a 4.00 mm (±0.15 mm) long NKT Photonics Low Loss single-mode fibres (LMA-10) with a solid core as the sensing element. This PCF fiber has a numerical

aperture (NA) of 0.11, mode field diameter (MFD) of 10.50 µm (±1 µm), and core diameter of 10.00 µm. Important features of this fibre type are low transmission loss, single-mode light transmission at all wavelengths, and a wavelength independent MFD.

In the experimental tests described in Sections 5.1 and 5.2, the lead-in and lead-out gap distances are fixed at 1.00 mm. In Section 5.3, the lead-in and lead-out gap distances are varied between 0.00 and 5.00 mm in 50-micron increments for each gap.

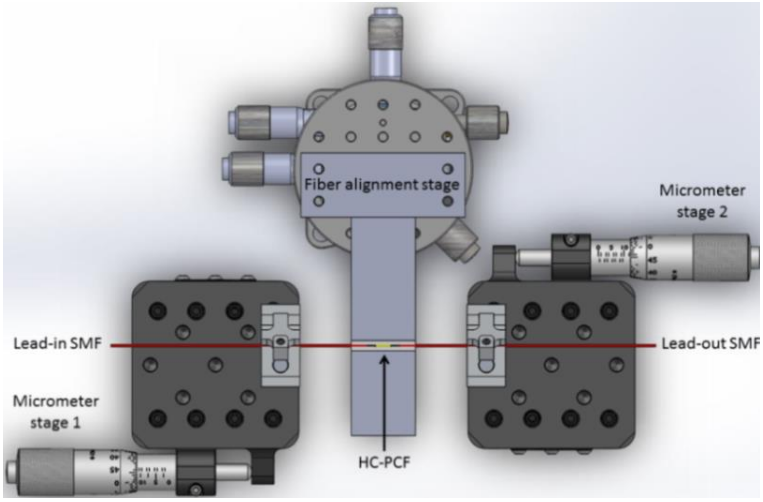

a)

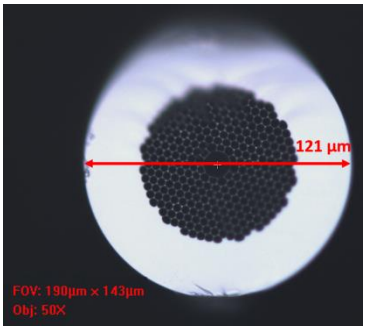

C)

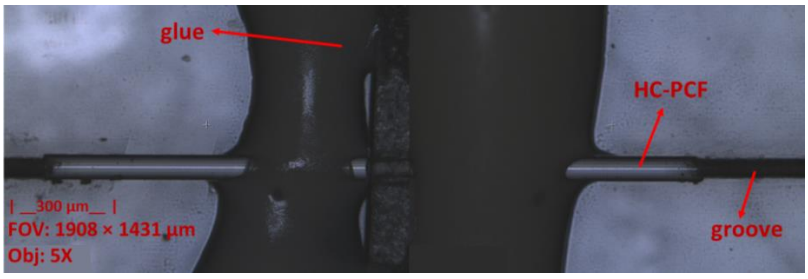

b)

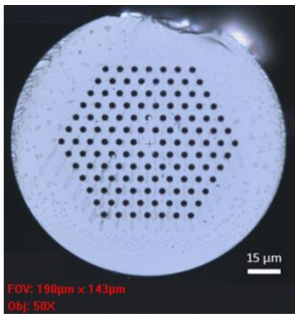

d)

Figure 4.2 (a) Top view of the fabrication setup using a fibre alignment stage and two linear-translation micro-stages for control of gap distances, (b) microscopic image of a sensing element glued to the microscope glass, (c) image of 10 micron HC-PCF fibre (Sensor Type-A), (d) image of solid-core PCF fiber (Sensor Type-C).

Figures 4.3 (a) and 4.3 (b) illustrate a normalized transmission spectrum and fringe spacing of Sensor Type-A (gaps of 1.00 mm) immersed in a test chamber containing nitrogen at atmospheric pressure. Each valley measured at the sensor's output (Figure 4.3 (a)) results from interference between the signal arms in the MZI at that wavelength. Sensor Type-A has fringe spacing of 1.22 nm. Sensor Types B and C have fringe spacing of 1.31 and 1.20, respectively.

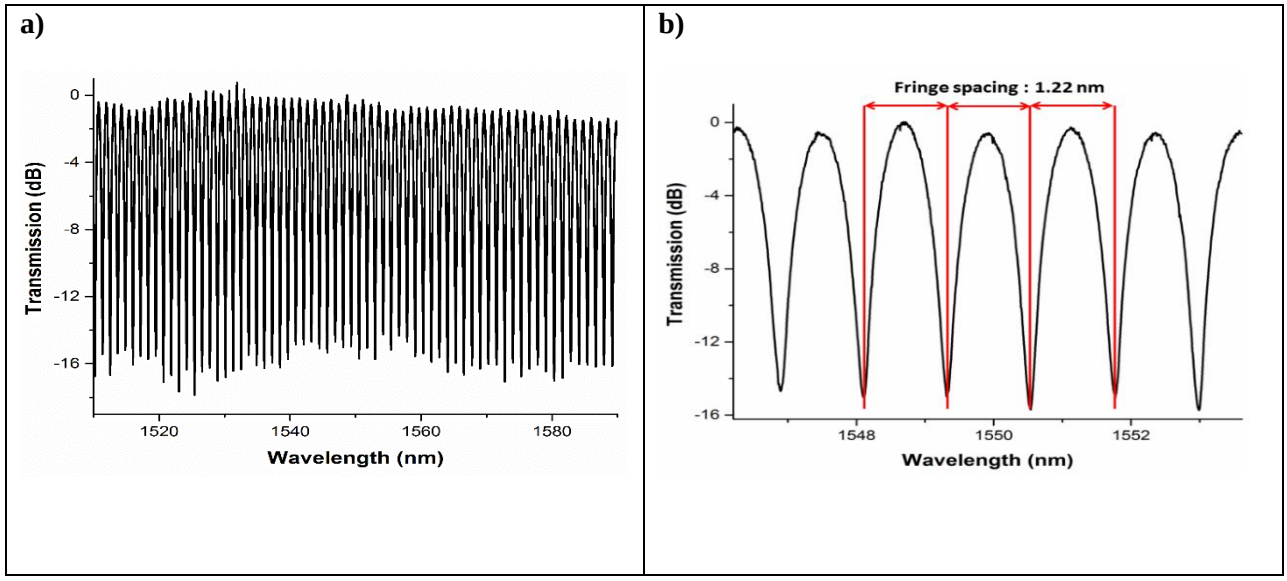

Figure 4.3 (a) Normalized transmission spectrum of Sensor Type-A with length of 4 mm and gaps of 1 mm immersed in nitrogen at room temperature and atmospheric pressure, (b) Fringe spacing measured at the lead-out side of Sensor Type-A.

4.4. Experimental Procedure

The first set of experiments conducted on the sensor types (A, B, and C) investigated the variation in the refractive index of the sensing element and gas combination. The schematic diagram of Figure 4.4 shows the overall arrangement of the sensor evaluation system, including the spectrum analyzer, input fiber circulator, the sensor fiber, and the gas

intake valves connected to the test chamber. The test chamber has dimensions of 14.5 cm × 11.2 cm × 4.4 cm, and allows two gas sources to be connected via intake valves: (i) nitrogen (N_2) gas which is used as a reference, and (ii) test (measurand) gases consisting of 25%, 50%, 75%, and 100% concentrations of CO_2, helium, argon, and methane. In addition, pressure regulators were connected to the gas lines to ensure a constant injection pressure of 15 psi was maintained through the testing process. A discharge tube with a bubbler was used to sustain the pressure inside the test chamber. A Micron Optics interrogator (SM125) with a resolution of 1 pm was used to record and evaluate changes in the transmission spectrum. Additionally, a Fibre Bragg Grating (FBG) sensor, with a sensitivity of 10 pm/°C, was used to monitor and record the temperature fluctuations inside the chamber. The Micron Optics' Enlight software was used to record and analyze the spectral shifts of the three sensor types and the FBG.

The experiments started with injecting N_2 into the test chamber until an even gas diffusion into all the PCF and HC-PCF's air holes was achieved. The measurand gases were then individually injected into the chamber and sensor responses were recorded using the Micron optics interrogator. Cyclic tests were carried out to examine the repeatability of RI measurements using the proposed sensors. Subsequently, important sensing performance parameters were studied, including RI sensitivity and the sensor response and recovery times. The spectral response of each sensor type is a function of the gas species injected into the chamber, the pressure, and temperature. Therefore, as part of the sensor characterization process, the FBG was placed in-line with the sensors and the temperature fluctuations within the chamber were simultaneously recorded in order to compensate for temperature effects.

Reliable operation and repeatable sensing capability are essential in any sensing application, especially in gas sensing. Therefore, the sensors were characterized several times and at different wavelengths, using a constant time interval (7 minutes) for each test gas at the different concentrations. Each sensor's output signal was interrogated for the gas under evaluations and the sensors showed a consistent trend in wavelength shifts (Figure 4.5).

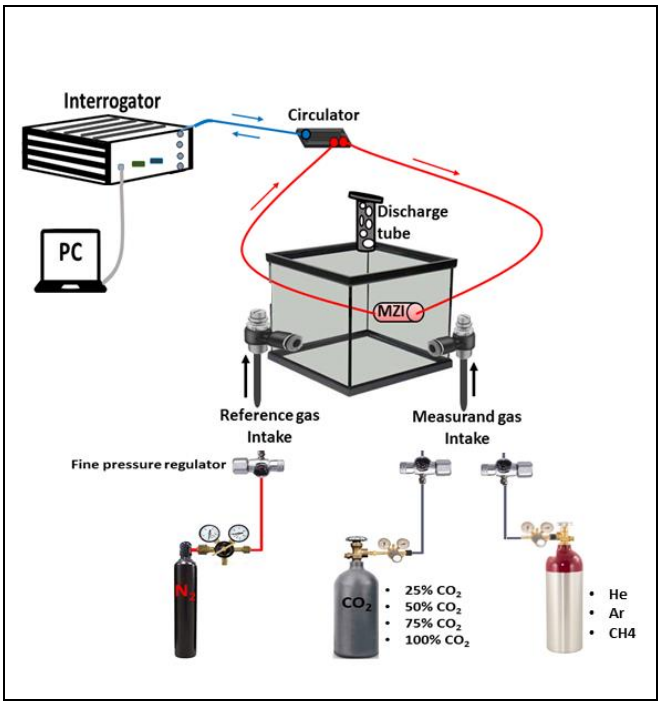

Figure 4.4 Schematic of the experimental setup: tests were carried out at room temperature and atmospheric pressure.

4.5. Results and Discussion

4.5.1. Refractive Index Measurement of the Test Gas in the Sensing Element

Figure 4.5 illustrates the response of Sensor Type-A to carbon dioxide for three experimental cycles and with a fixed lead-in and lead-out distance of 1.00 mm. The sensor was individually interrogated to analyze its spectral response to CO_2 and a complete test cycle consisted of measuring the spectral response for the reference gas (99.99% pure nitrogen); followed by an injection and measurement of CO_2 (for 7 minutes); and finally, an

injection of nitrogen back into the chamber to purge the CO_2. In comparison with the position of the spectrum resulting from measurement of the reference gas, Sensor Type-A showed wavelength spectrum wavelength shifts of 118 pm, 240 pm, 352 pm, and 480 pm when immersed in 25%, 50%, 75%, and 100% concentrations of CO_2. The transmission spectrum for the sensor underwent a blue shift in response to the presence of CO_2. The RI of CO_2 is higher than the RI of nitrogen, which resulted in the blue shift of the interference fringes. In the transmission interference fringe, spectral shifts of three different valleys at different wavelengths were used to calculate wavelength shifts and measurement errors.

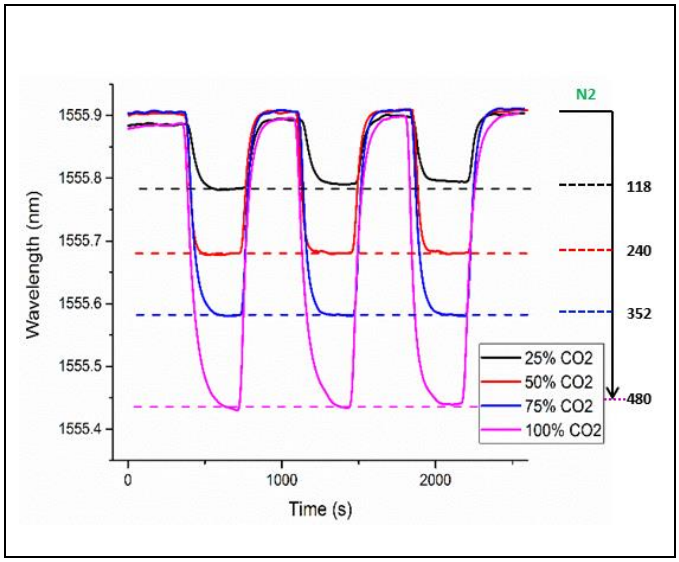

Figure 4.5 The spectral response of Sensor Type-A to different concentrations of CO_2 for 3 cycles, and a gap length of 1.00.

Figure 4.6 illustrates the response of Sensor Type-A to argon, helium, and methane for three experimental cycles. The sensor's wavelength response depended on the gas species injected into the chamber. In comparison with the position of the spectrum resulting from measurement of the reference gas, Sensor Type-A showed spectrum shifts of 850 pm (±6 pm), 53 pm (±3 pm), and 470 pm (± 5 pm) when immersed in He, Ar, and CH_4, respectively.

The transmission spectrum for each sensor test underwent red shifts in response to Ar and He, and blue shifts in response to CH_4. This finding can be explained as spectral response to a change in RI. Because the RIs of helium and argon are considerably lower than the RI of nitrogen, the interference fringe showed a red shift.

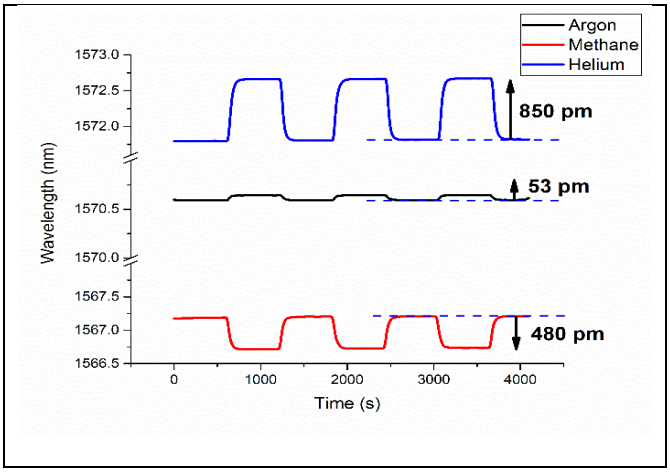

Figure 4.6 The spectral response of Sensor Type-A to 100% concentrations of Argon (99.99% pure), Helium (99% pure), and Methane for 3 cycles.

Table 4.1 summarizes the wavelength shifts of the entire family of sensor types (A, B, and C) to the measurand gases, as described above. The RI sensitivity achieved in this work is high, compared with the performance of alternative approaches described in the research literature. For example, a sensitivity of 1233 nm/RIU was reported for a HC-PCF MZI sensor [143], 1053 nm/RIU was reported for a cavity based Fabry-Perot [144], and 1546 nm/RIU was achieved for a Fabry-Perot sensor based on a hollow silica tube [145]. Sensor Type-A shows the highest wavelength shifts. In contrast, Sensor Type-C shows the lowest shifts when immersed in the measurand gases. The RI sensitivity of each MZI sensor in the RI range of 1.0000347–1.000449 is recorded in Table 4.1. The highest sensitivity of 3210 (nm/RIU) for Sensor Type-A and lowest sensitivity of 2140 (nm/RIU) for Sensor Type-C in the given RI range was achieved.

Table 4.1. Total wavelength shifts of MZI sensors for helium, methane, argon, and different concentrations of CO_2

Sensor Type	**Lead-in/out distance**	Spectral shift (pm) in helium	Spectral shift (pm) in methane	Spectral shift (pm) in 25% CO_2	Spectral shift (pm) in 50% CO_2	Spectral shift (pm) in 75% CO_2	Spectral shift (pm) in 100 % CO_2	Spectral shift (pm) in argon	**RI sensitivity (nm/RIU)**
A (10 µm)	**~ 1 mm**	850	470 (negative)	118 (negative)	240 (negative)	352 (negative)	480 (negative)	53	**3210**
B (20 µm)	**~ 1 mm**	670	430 (negative)	100 (negative)	210 (negative)	315 (negative)	432 (negative)	40	**2660**
C (PCF)	**~ 1 mm**	510	363 (negative)	95 (negative)	195 (negative)	263 (negative)	377 (negative)	30	**2140**

4.5.2. Performance parameters of MZI sensors

Response and recovery times are defined as the time the sensors required to reach 90% of the final value of the total wavelength shift. Figure 4.7 (a) is an example that shows response and recovery times for detection of methane with Sensor-A. Results indicate that Sensor-B shows the fastest response/recovery time, while Sensor-C had the slowest response/recovery time. This result can be attributed to the hollow-core structures of sensors A and B, compared to the solid-core structure of Sensor-C. The proposed HC-PCF MZI sensor has, nonetheless, the potential for advancing current capacity for low-percentage gas detection, environmental monitoring, and quantitatively analyzing changes in pure gases. Since the performance of the tested MZI sensors were evaluated at atmospheric pressure and room temperature, they can be used for detection of any pure gas with high precision. The RI of a target gas ($RI_{target\ gas}$) can be expressed by the following equation:

$$RI_{target\ gas} = RI_{N_2} - \Delta RI = RI_{N_2} - \ \Delta\lambda/(RI\ sensitivity) \qquad \textbf{(Eq. 4.5)}$$

where RI_{N_2} is the RI of the reference "N_2" gas, ΔRI is the relative difference in RI of a target and "N_2" gas. The ΔRI can be calculated using the wavelength shift ($\Delta\lambda$) of the interference fringe factoring in the sensitivity of the sensor. The $\Delta\lambda$ can be obtained by tracking a transmission valley of the interference fringes. Figure 4.7 (b) illustrates the sensitivity graph of Sensor-A to ambient RI change for the given RI range.

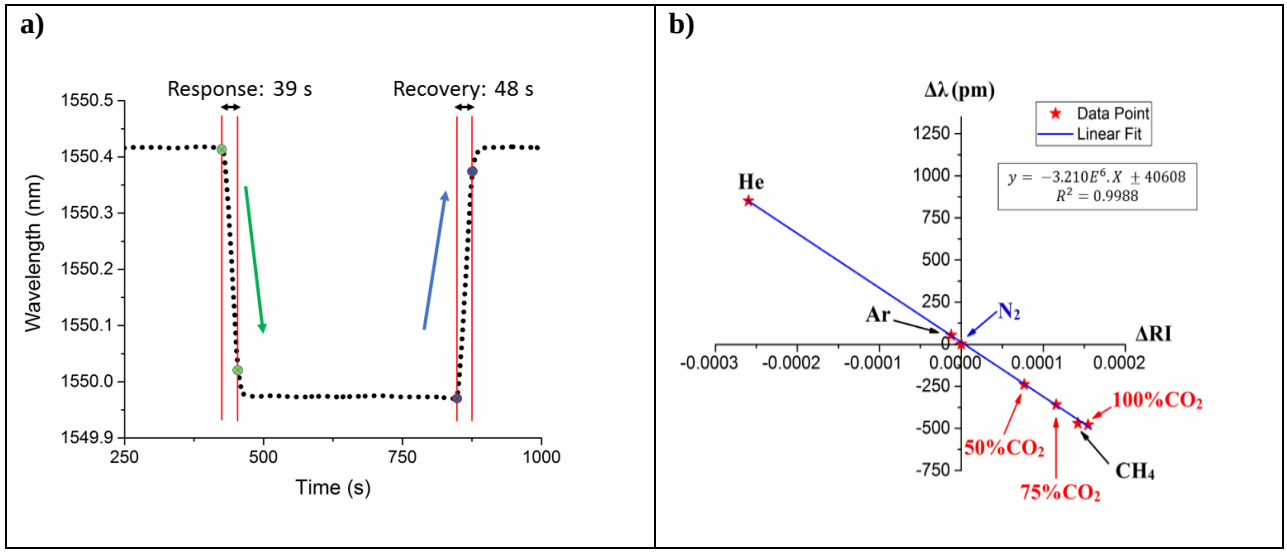

Figure 4.7 (a) Response and recovery times of Sensor-A for methane, (b) sensitivity graph of the same sensor to ambient RI change.

In order to analyze the number and power distribution of the modes participating in the modal interference process, the transmission spectrum of each sensor was Fourier transformed to obtain its corresponding spatial frequency, described as [146]:

$$v = \frac{\Delta n_{eff}.D}{\lambda^2} \qquad \textbf{(Eq. 4.6)}$$

Δn_{eff} is the effective RI difference between core and cladding of the sensing element, and D is the distance between the two ends of the SMFs. To be able to examine the characteristics of measured interference in Fourier domain, the wavelength spectra of each MZI sensor in

the presence of various gases were Fourier transformed. Figure 4.8 (a) shows the spatial frequency response of Sensor-A in the presence of a pure gas, such as nitrogen, helium, methane, and carbon dioxide. The dominant peak corresponds to the interference between one higher-order mode and the fundamental mode. A characteristic of this figure's data is that the magnitude of the spatial frequency for the dominant peak is constant in the presence of measurand gases with different RI, but the amplitude of the peaks varies [147]. The amplitude of each peak corresponds to the amount of power carried by that mode. For example, for Sensor-A, power of dominant mode has the minimum amplitude of 2.11 for helium, and the maximum amplitude of 2.58 for nitrogen. Sensor-C (Figure 4.8 (b)) carried the dominant mode with the minimum amplitude of 1.91 for nitrogen, and the maximum amplitude of 2.22 for helium. This method is another approach to characterize and distinguish the presence of different gases. In order to clarify the performance of each MZI, the next section of this report explains the effect of structure of the sensing element on the carrying power of each mode.

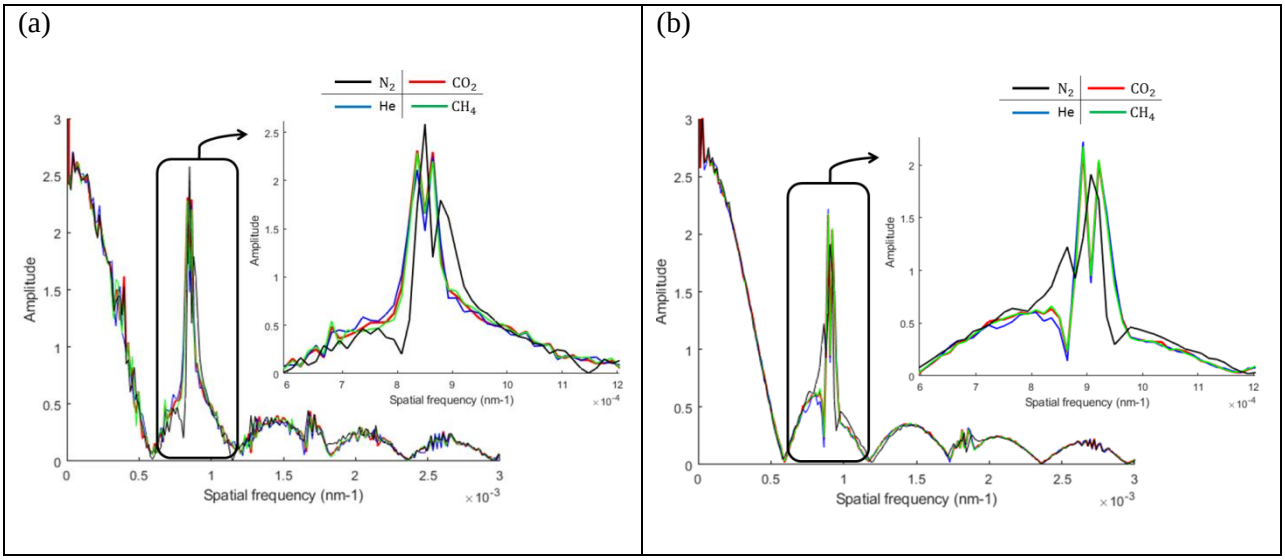

Figure 4.8 (a) Effect of gas RI on spatial frequencies for Sensor-A; The dominant mode has an amplitude of 2.11, 2.28, 2.31 and 2.58 for pure helium, carbon dioxide, methane and nitrogen respectively. (b)

Similar effect for Sensor-C; the dominant mode has an amplitude of 1.91, 2.16, 2.17 and 2.2 for pure helium, carbon dioxide, methane and nitrogen respectively.

4.5.3. Spatial frequency analysis of effect of fibre structure and gap length on number and power distribution of modes for MZI gas sensor

A second set of experiments were performed to analyze the effect of gap distance, as well as the structure of the sensing element on the modal interference of the proposed MZI gas sensors. The lead-in and lead-out SMFs were not glued to the microscope slide so that it was possible to change the gap distance on both sides of the sensing element. Linear translation stages were used to alter the gap lengths on each side of the sensing element; each gap was increased from 0 to 5.00 mm in 50-micron increments (D in equation 4.6 varied from 4 mm to 14 mm in 100 micron increments in the mentioned formula of spatial frequency). While maintaining equal gap distance on both sides of the sensing element, 100 transmission spectrums were collected for each of three types of MZI configuration: (i) a 10 µm core HC-PCF sensing element, (ii) a 20 µm core HC-PCF sensing element, and (iii) a solid core PCF as the sensing element. The spectrums were processed through a Fourier Transform in order to obtain spatial frequency graphs of each sensing element type and examine the number and power distribution of the modes. Different peaks in the spatial frequency graph correspond to the interference between fundamental mode and different higher-order modes.

4.5.3.1. Spatial Frequency Analysis of MZI sensors with solid core PCF

For the MZI with solid-core PCF, spatial frequency analysis revealed that the power is mainly carried by one mode (core-cladding 1) in the spatial frequency spectrum for gap distances ranging from 0 to 3.75 mm. For gap lengths higher than 3.75 mm, the amplitude of the dominant mode decreases dramatically. Figure 4.9 (a) shows the spatial frequency graph

for a PCF-MZI sensor with D = 6.5 mm, which contains a dominant mode at 9.5×10^{-4} (1/nm). Highest amount of power carried by the dominant mode was recorded at D = 11.3 mm with normalized FFT value of 3.56, which is higher than FFT values for HC-PCF sensors. Phase shift information produced by the MZI sensors can also be extracted from the spatial frequency graph. Figure 4.9 (b) illustrates the phase diagram of the MZI presented in figure 4.9 (a), and reveals that the dominant mode has a phase shift of 148 degrees.

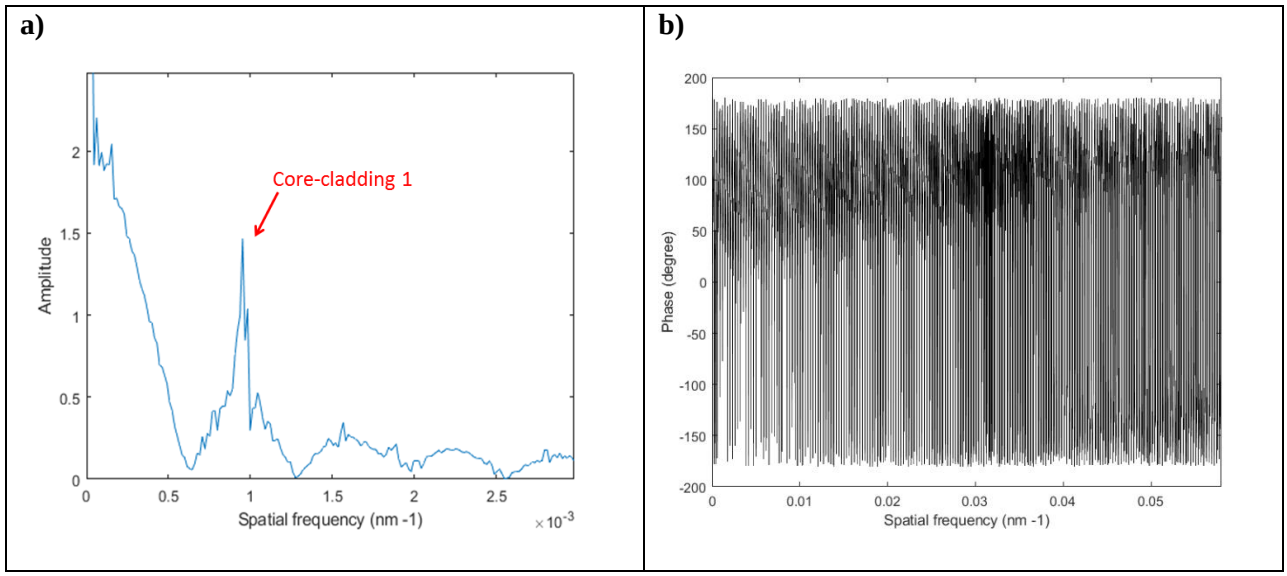

Figure 4.9 (a) Spatial frequency graph for a solid-core PCF MZI with PCF length of 4 mm and D of 6.5 mm; here, power is mainly carried by one mode. (b) The phase diagram of the same sensor; the dominant mode has a phase shift of 148 degrees.

4.5.3.2. Spatial Frequency Analysis of MZI sensors with 10 µm core HC-PCF

It was shown that the power is mainly distributed between two dominant modes in the spatial frequency spectrum, as gap distances increased. This behaviour confirms that higher-order modes would gradually leak off the sensing fibre and experience transmission losses, and fewer peaks would turn up in the spatial frequency graph due to a weakening interference effect. Figure 4.10 (a) shows the spatial frequency graph for the MZI with 10 µm HC-PCF and gaps of 1.5 mm on sides (D = 7 mm). The same device is made up of a

strong cladding mode with a spatial frequency of 5×10^{-4} (1/nm) and normalized FFT value of 3.14, which is named core-cladding 1. Besides this dominant cladding mode, the sensor also contains a relatively weaker cladding mode (core-cladding 2) with a spatial frequency of 1.1×10^{-3} (1/nm) and a normalized FFT value of 0.99. It was found that for sensors with gaps from 0 to 1.65 mm core-cladding 1 is the dominant cladding mode, while for higher gaps core-cladding 2 became the dominant mode. The highest power transmission was found in an MZI with gaps of 1.35 mm, and the amplitude of spatial frequencies decreased intensely for gaps higher than 4.5 mm. Figure 4.10 (b) was plotted by tracking dominant modes of the MZI with respect to D. It shows how the magnitudes of spatial frequencies increase by increasing length of gaps. As the spatial frequencies are obtained by equation 4.6 and transmission spectrums of MZIs, the instability of light source as well as inaccuracy in the distance between two ends of SMFs can impose errors on spatial frequency values. For example, ±0.15 mm tolerance in a 4 mm stub of sensing element can lead to errors from 1% (for D = 14 mm) to 3.75% (for D = 4 mm) on spatial frequency values. Errors associated with gap lengths can be eliminated by using automated fiber positioning systems. Besides, by equal splitting of fundamental core mode of the lead-in fiber into core and cladding modes of the HC-PCF, transmission fringe can be improved.

The results of measured phase shifts of the MZI can be compared with the calculated phase shifts (see equation 4.2) for the same sensor. The core-cladding 1 mode of the MZI sensor travels through the core and the first layer of air-holes in the cladding (those closest to the hollow-core). The calculated phase shift of the dominant mode in this MZI is 168 degrees, while the measured phase shift of the dominant mode is 172 degrees. A difference

of about 2.2% exists between the measured and calculated phase shifts. The dominant mode in the 10 µm HC-PCF MZI with highest power transmission has a phase shift of 160 degrees.

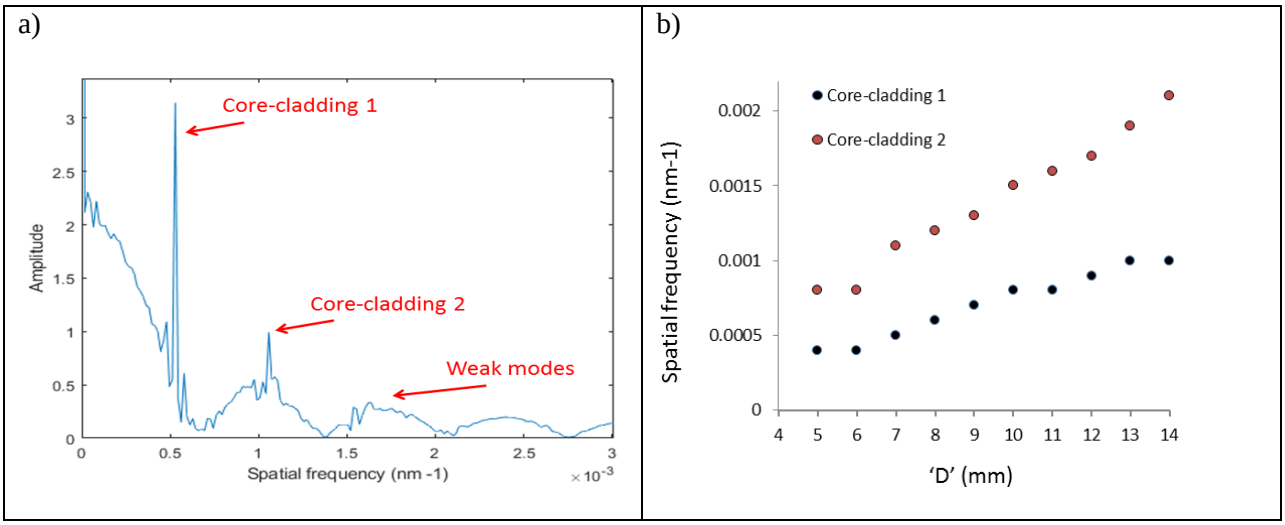

Figure 4.10 (a) Spatial frequency graph for a 10 µm HC-PCF MZI with HC-PCF length of 4 mm and D of 7 mm, (b) tracking dominant modes of the sensor with respect to D, where power is mainly distributed between two dominant modes.

4.5.3.3. Spatial Frequency Analysis of MZI sensors with 20 µm core HC-PCF

Figures 4.11 (a) and 4.11 (b) show spatial frequencies for the MZI with 4 mm of 20 micron HC-PCF as the sensing element, with gaps of 1 mm and 2.2 mm on both sides. 100 data points were analysed for this sensor, with D varying from 4 mm to 14 mm in 100 micron steps. As shown in Figure 4.11, several modes are involved in the modal interference and power is mainly distributed in three dominant modes in the spatial frequency spectrum, as gap distances increased for the MZI with 20 micron HC-PCF. Some higher-order modes would leak the sensing fiber, similar to processes observed in the MZI with 10 micron HC-PCF, but results indicate that stronger interferences as well as a higher number of modes can be carried by 20 micron HC-PCF sensors. Figure 4.11 (a) shows three strong core-cladding modes with spatial frequencies of 3.9×10^{-4} (1/nm), 4.6×10^{-4} (1/nm), and 8.5×10^{-4} (1/nm) followed by a weaker mode at 1.3×10^{-3} (1/nm).

Experiment results indicate that for gap distances from 0 to 0.75 mm on each side, core-cladding 1 was the dominant mode. The highest amount of power carried by this mode was recorded at D = 4.8 mm (with gaps of 0.4 mm) and at 2.9×10^{-4} (1/nm). For gap distances higher than 2.5 mm on each side, core-cladding 3 became the dominant mode and the highest amount of power carried by this mode was observed for D = 10 mm (with gaps of 3 mm) and at 1.4×10^{-3} (1/nm). Phase shift information of this MZI reveals that the dominant mode has a phase shift of 166 degrees.

The amplitude of spatial frequencies decreases continuously when gaps are set at 3.5 mm and higher. By tracking normalized FFT values of dominant modes, it was concluded that for gap distances ranging from 0.8 mm to 3.15 mm all three dominant modes carry high amounts of power. This observation contrasts to the results obtained by experimenting with a 10 micron HC-PCF MZI. So, higher power transmission occurs with a 20 micron HC-PCF than through the other tested sensing element configurations.

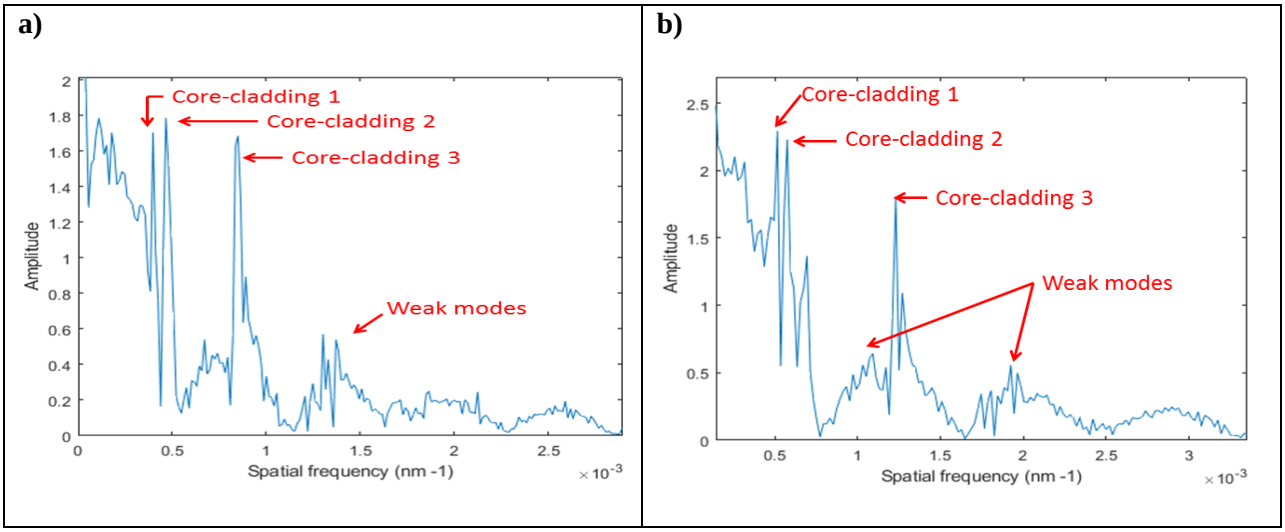

Figure 4.11 Spatial frequency graph for a 20 µm HC-PCF MZI with HC-PCF length of 4 mm and (a) D of 6 mm, (b) D of 8.4 mm. Power is mainly distributed between three dominant modes.

4.6. Conclusion

A compact PCF-based interferometric sensor structure is proposed and has been experimentally demonstrated for sensitive detection of gases. Several sensors were fabricated and characterized using 3 types of photonic crystal fibre as the sensing element. The resulting fibre sensors were able to measure the RI of a gas-filled cavity and each showed excellent sensitivity to helium, methane, argon, and various concentrations of carbon dioxide. The highest RI sensitivity of 3210 nm/RIU was demonstrated in the RI range of 1.0000347–1.000449 for a sensor with 4 mm length of 10 µm HC-PCF. This shows an improvement over results obtained through previous laboratory research and experimental design. Results of the present project indicate that the 20 µm HC-PCF MZI sensor shows the fastest response/recovery time, while solid-core PCF-MZI shows the slowest response/recovery time. The effects of gap distances on the number and amplitude distribution of the sensors' modes were examined. Spatial frequency analysis revealed that power is mainly carried by two dominant modes in the 10 µm MZI, three dominant modes in the 20 µm MZI, and one mode in the solid-core PCF. Highest amount of power transmission was recorded for an MZI with solid core PCF. It was concluded that stronger interference occurs by using 20 µm HC-PCF as sensing element of the MZI, and a higher number of modes can be carried by this fiber. Additionally, power transmission and phase shift of dominant modes were studied for MZIs with different sensing elements. This sensor type is a suitable choice for low-percentage detection of gases as well as environmental monitoring.

Chapter 5 Conclusions and Future Work

5.1. Conclusion

We present an in-line and compact Mach-Zehnder Interferometer point sensor using photonic crystal fibers, designed for high sensitivity and measurement of refractive index. The work of this dissertation includes design and fabrication procedure of the proposed MZI gas sensor. Compactness, fast response, high resolution and high sensitivity, and easy fabrication procedure were the main goals during development of the new MZI configuration.

In Chapter 2, the light propagation, working principle, and performance parameters of the proposed gas sensor were discussed for high sensitivity measurement of pure gases. The proposed MZI sensor employed a short length of HC-PCF as the sensing element of a Mach-Zehnder interferometer. Fabrication of the sensor was done manually by positioning and aligning the sensing element fiber between two single mode fibers with air gaps at each interface to allow gas diffusion into the micro holes of the sensing element fiber. The effects of length of HC-PCF on RI sensitivity, response and recovery times were studied. The sensitivity of the fabricated MZI sensor increases when the length of the sensing element decreases, which does not match the basic equations for an MZI. The main reasons are that the light propagation in the sensing arm of the proposed MZI contains more than one arm, which results in higher number of modes associated with mode coupling. In addition, the reference arm itself is in contact with the measurand gas as well, which alters from basic definition of MZI in which the reference arm is not in contact with the surrounding medium. Furthermore, it is shown that response and recovery times of the proposed sensor inversely

change with the length of the sensing element fiber, namely solid/hollow core photonic crystal fibers. It is shown that the temperature sensitivity of the fiber-optic interferometer decreases when the length of the PCF decreases.

Chapter 3 focuses on the performance of the optical fiber MZI sensor in the leakage detection of different concentrations of carbon dioxide, in a laboratory-scale test chamber, subsurface soil, and aqueous environments. The reported fiber-optic gas sensors to date either display insufficient sensitivity/reliability or require complex fabrication and/or packaging processes. The sensor was wrapped with two water-impermeable membranes that allow gas flow in the chamber. The two membranes were assembled to achieve a good balance of CO_2 permeability and water resistance, and made it operational in the aqueous environment. The sensor's signal was monitored for several days under water to check degradation of the spectrum due to presence of water vapor. The sensor shows the sensitivity of 4.3 pm/ % CO_2 and has a great potential for environmental monitoring of CO_2.

The work in Chapter 4 explains the effect of gap distance on the number and amplitude distribution of the modes. This was done to optimize the design elements. Three types of sensors were fabricated using the proposed configuration employing the same length but different types of photonic crystal fibers. For each sensor type, gap distances were varied in 50-micron increments at each gap and transmission spectrums were recorded. Spatial frequency analysis revealed that power is mainly carried by one mode in the solid-core PCF, two dominant modes in the 10 μm MZI, and three dominant modes in the 20 μm MZI. In addition, a detailed study was conducted to better understand the effect of photonic crystal fiber structure on the performance of the fiber-optic gas sensors. By comparing the

performance of these sensors in detection of gas presence, it was concluded that the sensor with 10 μm HC-PCF had the highest sensitivity, whereas the highest amount of power transmission was recorded for an MZI with solid core PCF. Stronger interference occurs by using 20 μm HC-PCF and a higher number of modes can be carried by this fiber. The sensors are highly sensitive to low percentages of CH_4 and CO_2, making them suitable for greenhouse gas measurement. It should be noted that the main drawback of this sensor is gas selectivity, as it is responsive to the presence of any gas and is not selective.

5.2. Future Work

Future research that could extend results presented in this dissertation may include the following topics:

- Characterization of the proposed MZI sensors to other parameters such as pressure and humidity.
- Fabrication of MZI sensors with alternative sensing element fibers such as microfibers and tapered fibers.
- Using numerical interface to solve the Maxwell governing equations by finite element methods.
- Numerical analysis to find the modal characteristics of the proposed configuration and optimize design elements. The numerical interface provided by COMSOL Metaphysics in the Wave Optics Module or mode analysis module is expected to be the appropriate tool.
- Using automated fiber positioning systems to eliminate errors associated with distancing.
- Deposition of polymers on the holes of the sensing element may enhance the sensitivity. In addition, by adding specific coating on holes and cladding of the sensing element fiber, gas selectivity can be achieved.

Bibliography

1. Y. Liu, J. Parisi, X. Sun, and Y. Lei, "Solid-state gas sensors for high temperature applications – a review," *Journal of Materials Chemistry A,* vol. 2, pp. 9919-9943, **2014**.
2. H. Moser, W. Pölz, J. P. Waclawek, J. Ofner, and B. Lendl, "Implementation of a quantum cascade laser-based gas sensor prototype for sub-ppmv H_2S measurements in a petrochemical process gas stream," *Analytical and Bioanalytical Chemistry,* vol. 409, pp. 729-739, January 01 **2017**.
3. Y. Shi, Z. Li, J. Shi, F. Zhang, X. Zhou, Y. Li, *et al.*, "Titanium dioxide-polyaniline/silk fibroin microfiber sensor for pork freshness evaluation," *Sensors and Actuators B: Chemical,* vol. 260, pp. 465-474, **2018**.
4. K. A. Ahmmed A. Rifat, S. A. , B. K. P. , and R. Ahmed, "Development of Photonic Crystal Fiber-Based Gas/Chemical Sensors," *Computational Photonic Sensors,* pp. 1-31, **2018**.
5. A. M. R. Pinto and M. Lopez-Amo, "Photonic Crystal Fibers for Sensing Applications," *Journal of Sensors,* vol. 2012, p. 21, **2012**.
6. P. P. Shum, D. J. J. Hu, and R. Y.-N. Wong, "Photonic Crystal Fiber–Based Interferometric Sensors," in *Intechopen*, **2017**, pp. 22-41.
7. H.-E. Joe, "A review on optical fiber sensors for environmental monitoring," *International Journal of Precision Engineering and Manufacturing-Green Technology,* vol. 5, pp. 173-191, **2018**.
8. M. P. Buric, K. P. Chen, J. Falk, and S. D. Woodruff, "Enhanced spontaneous Raman scattering and gas composition analysis using a photonic crystal fiber," *Applied Optics,* vol. 47, pp. 4255-4261, **2008**.
9. A. Abdelghani, J. M. Chovelon, N. Jaffrezic-Renault, C. Ronot-Trioli, C. Veillas, and H. Gagnaire, "Surface plasmon resonance fibre-optic sensor for gas detection," *Sensors and Actuators B: Chemical,* vol. 39, pp. 407-410, **1997**.
10. G. Stewart, F. A. Muhammad, and B. Culshaw, "Sensitivity improvement for evanescent-wave gas sensors," *Sensors and Actuators B: Chemical,* vol. 11, pp. 521-524, **1993**.
11. X. Yang, A. S. P. Chang, B. Chen, C. Gu, and T. C. Bond, "Multiplexed gas sensing based on Raman spectroscopy in photonic crystal fiber," in *IEEE Photonics Conference 2012*, **2012**, pp. 447-448.
12. Ying Wang, D. N. Wang, C. R. Liao, Tianyi Hu, Jiangtao Guo, and Huifeng Wei, "Temperature-insensitive refractive index sensing by use of micro Fabry–Pérot cavity based on simplified hollow-core photonic crystal fiber," *Opt. Lett*. 38, 269-271, **2013**.
13. D. J. J. Hu *et al*., "Novel Miniaturized Fabry–Perot Refractometer Based on a Simplified Hollow-Core Fiber With a Hollow Silica Sphere Tip," in *IEEE Sensors Journal*, vol. 12, no. 5, pp. 1239-1245, **2012**.
14. Rajan Jha, Joel Villatoro, and Goncal Badenes, "Ultrastable in reflection photonic crystal fiber modal interferometer for accurate refractive index sensing," *Appl. Phys. Lett*. 93, 191106, **2008**.
15. Sun H, Zhang J, Rong Q, Feng D, Du Y, Zhang X, et al. "A hybrid fiber interferometer for simultaneous refractive index and temperature measurements based on Fabry–Perot/ Michelson interference," *IEEE Sensors Journal*. **2013**;13(5):2039-2044.
16. Qiang Liu, Liang Xin, and Zhaoxia Wu, "Refractive index sensor of a photonic crystal fiber Sagnac interferometer based on variable polarization states, " *Applied Physics Express*, Volume 12(6), **2019**.
17. L. Li, L. Xia, Z. Xie, and D. Liu, "*All-fiber Mach-Zehnder interferometers for sensing applications*," *Optics Express,* vol. 20, pp. 11109-11120, **2012**.
18. X. Huang, X. Li, J. Yang, C. Tao, X. Guo, H. Bao*, et al.*, "An in-line Mach-Zehnder Interferometer Using Thin-core Fiber for Ammonia Gas Sensing With High Sensitivity," *Scientific Reports,* vol. 7, p. 44994, **2017**.
19. H. Y. Choi, M. J. Kim, and B. H. Lee, "All-fiber Mach-Zehnder type interferometers formed in photonic crystal fiber," *Optics Express,* vol. 15, pp. 5711-5720, **2007**.
20. F. Ahmed, V. Ahsani, L. Melo, P. Wild and M. B. G. Jun, "Miniaturized Tapered Photonic Crystal Fiber Mach–Zehnder Interferometer for Enhanced Refractive Index Sensing," in *IEEE Sensors Journal*, vol. 16, no. 24, pp. 8761-8766, **2016**.

21. Ahsani V, Ahmed F, Jun MBG, Bradley C., "Tapered Fiber-Optic Mach-Zehnder Interferometer for Ultra-High Sensitivity Measurement of Refractive Index. Sensors," *(Basel)*. 2019;19(7):1652. Published **2019** Apr 6. doi:10.3390/s19071652.
22. F. Ahmed, V. Ahsani, A. Saad, and M. B. G. Jun, "Bragg Grating Embedded in Mach-Zehnder Interferometer for Refractive Index and Temperature Sensing," *IEEE Photonics Technology Letters,* vol. 28, pp. 1968-1971, **2016**.
23. L. M. Hu, C. C. Chan, X. Y. Dong, Y. P. Wang, P. Zu, W. C. Wong, *et al.*, "Photonic Crystal Fiber Strain Sensor Based on Modified Mach–Zehnder Interferometer," *IEEE Photonics Journal,* vol. 4, pp. 114-118, **2012.**
24. B. Yao, Y. Wu, Y. Cheng, A. Zhang, Y. Gong, Y.-J. Rao, *et al.*, "All-optical Mach–Zehnder interferometric NH3 gas sensor based on graphene/microfiber hybrid waveguide," *Sensors and Actuators B: Chemical,* vol. 194, pp. 142-148, **2014**.
25. T. Hao and K. S. Chiang, "Graphene-Based Ammonia-Gas Sensor Using In-Fiber Mach-Zehnder Interferometer," *IEEE Photonics Technology Letters,* vol. 29, pp. 2035-2038, **2017**.
26. D.-W. Duan, Y.-J. Rao, L.-C. Xu, T. Zhu, D. Wu, and J. Yao, "In-fiber Mach–Zehnder interferometer formed by large lateral offset fusion splicing for gases refractive index measurement with high sensitivity," *Sensors and Actuators B: Chemical,* vol. 160, pp. 1198-1202, **2011**.
27. T. Zhang, Y. Zheng, C. Wang, Z. Mu, Y. Liu, and J. Lin, "A review of photonic crystal fiber sensor applications for different physical quantities," *Applied Spectroscopy Reviews,* vol. 53, pp. 486-502, **2018**.
28. C. Tao, H. Wei, and W. Feng, "Photonic crystal fiber in-line Mach-Zehnder interferometer for explosive detection," *Optics Express,* vol. 24, pp. 2806-2817, **2016**.
29. J. Yang, L. Zhou, X. Che, J. Huang, X. Li, and W. Chen, "Photonic crystal fiber methane sensor based on modal interference with an ultraviolet curable fluoro-siloxane nano-film incorporating cryptophane A," *Sensors and Actuators B: Chemical,* vol. 235, pp. 717-722, **2016**.
30. R. F. Cregan, B. J. Mangan, J. C. Knight, T. A. Birks, P. S. J. Russell, P. J. Roberts, *et al.*, "Single-Mode Photonic Band Gap Guidance of Light in Air," *Science,* vol. 285, p. 1537, **1999**.
31. H. Qu and M. Skorobogatiy, "Liquid-core low-refractive-index-contrast Bragg fiber sensor," *Applied Physics Letters,* vol. 98, p. 201114, **2011**.
32. K. Kalli, A. M. Cubillas, W. Urbanczyk, M. Silva-Lopez, J. M. Lazaro, O. M. Conde, *et al.*, "Detection of methane at 1670-nm band with a hollow-core photonic bandgap fiber," *Optics Express,* vol. 15, **2007**.
33. W. Jin, H. L. Ho, Y. C. Cao, J. Ju, and L. F. Qi, "Gas detection with micro- and nano-engineered optical fibers," *Optical Fiber Technology,* vol. 19, pp. 741-759, **2013**.
34. R. M. Wynne, B. Barabadi, K. J. Creedon, and A. Ortega, "Sub-Minute Response Time of a Hollow-Core Photonic Bandgap Fiber Gas Sensor," *Journal of Lightwave Technology,* vol. 27, pp. 1590-1596, **2009**.
35. L. Xuefeng, P. Joanna, L. Jinxing, X. Guan, and U. Toshitsugu, "Fabrication of Photonic Bandgap Fiber Gas Cell Using Focused Ion Beam Cutting," *Japanese Journal of Applied Physics,* vol. 48, p. 06FK05, **2009**.
36. D. N. Wang, "Micro-engineered Optical Fiber Sensors Fabricated by Femtosecond Laser Micromachining," in *Imaging and Applied Optics Technical Papers*, Monterey, California, **2012**.
37. N. L. P. Andrews, R. Ross, D. Munzke, C. van Hoorn, A. Brzezinski, J. A. Barnes, *et al.*, "In-fiber Mach-Zehnder interferometer for gas refractive index measurements based on a hollow-core photonic crystal fiber," *Optics Express,* vol. 24, pp. 14086-14099, **2016**.
38. I. Shavrin, S. Novotny, A. Shevchenko, and H. Ludvigsen, "Gas refractometry using a hollow-core photonic bandgap fiber in a Mach-Zehnder-type interferometer," *Applied Physics Letters,* vol. 100, p. 051106, **2012**.
39. Ahmed, Farid et al. "Monitoring of Carbon Dioxide Using Hollow-Core Photonic Crystal Fiber Mach-Zehnder Interferometer." *Sensors (Basel, Switzerland)* vol. 19,15 3357. **2019**, doi:10.3390/s19153357.
40. K. Nazeri, V. Ahsani, F. Ahmed, H. Joe, M. Jun and C. Bradley, "Experimental comparison of the effect of the structure on MZI fiber gas sensor performance," 2019 *IEEE Pacific Rim Conference on Communications, Computers and Signal Processing (PACRIM)*, Victoria, BC, Canada, **2019**, pp. 1-6.
41. Xiao, G.Z., et al., Monitoring changes in the refractive index of gases by means of a fiber optic Fabry-Perot interferometer sensor. Sensors and Actuators A: Physical, **2005**. 118(2): p. 177-182.

42. F. Benabid and P. J. Roberts, "Linear and nonlinear optical properties of hollow core photonic crystal fiber," *Journal of Modern Optics,* vol. 58, pp. 87-124, **2011**.
43. C. M. B. Cordeiro, M. A. R. Franco, G. Chesini, E. C. S. Barretto, R. Lwin, C. H. B. Cruz*, et al.*, "Microstructured-core optical fibre for evanescent sensing applications," *Optics Express,* vol. 14, pp. 13056-13066, **2006**.
44. Z. Zhi-guo, Z. Fang-di, Z. Min, and Y. Pei-da, "Gas sensing properties of index-guided PCF with air-core," *Optics & Laser Technology,* vol. 40, pp. 167-174, **2008**.
45. C. Tao, X. Li, J. Yang, and Y. Shi, "Optical fiber sensing element based on luminescence quenching of silica nanowires modified with cryptophane-A for the detection of methane," *Sensors and Actuators B: Chemical,* vol. 156, pp. 553-558, **2011**.
46. Q. Wang, W. Wei, M. Guo, and Y. Zhao, *Optimization of Cascaded Fiber Tapered Mach-Zehnder Interferometer and Refractive Index Sensing Technology* vol. 222: Sensors amd Actuators B: Chemical, **2016**.
47. H. Zhang, S. Gao, Y. Luo, Z. Chen, "Ultrasensitive Mach-Zehnder Interferometric Temperature Sensor Based on Liquid-Filled D-Shaped Fiber Cavity", Sensors, 18. 1239. 10.3390/s18041239, **2018**.
48. P. Jia, G. Fang, T. Liang, Y. Hong, Q. Tan, X. Chen*, et al.*, "Temperature-compensated fiber-optic Fabry–Perot interferometric gas refractive-index sensor based on hollow silica tube for high-temperature application," *Sensors and Actuators B: Chemical,* vol. 244, pp. 226-232, **2017**.
49. W. Ding, S. R. Andrews, T. A. Birks, and S. A. Maier, "Modal coupling in fiber tapers decorated with metallic surface gratings," *Optics Letters,* vol. 31, pp. 2556-2558, **2006**.
50. R. Wang and X. Qiao, "Hybrid optical fiber Fabry-Perot interferometer for simultaneous measurement of gas refractive index and temperature," *Applied Optics,* vol. 53, pp. 7724-7728, **2014**.
51. G. Nemova and R. Kashyap, "Novel fiber Bragg grating assisted plasmon-polariton for bio-medical refractive-index sensors," *Journal of Materials Science: Materials in Electronics,* vol. 18, pp. 327-330, **2007**.
52. M. S. Ferreira, L. Coelho, K. Schuster, J. Kobelke, J. L. Santos, and O. Frazão, "Fabry–Perot cavity based on a diaphragm-free hollow-core silica tube," Optics Letters, vol. 36, pp. 4029-4031, **2011**.
53. Ciais, P.; Sabine, C.; Bala, G.; Bopp, L.; Brovkin, V.; Canadell, J.; Chhabra, A.; DeFries, R.; Galloway, J.; Heimann, M.; Jones, C.; Quéré, C. Le; Myneni, R. B.; Piao, S.; Thornton, P. The physical science basis. Contribution of working group I to the fifth assessment report of the intergovernmental panel on climate change. Chang. IPCC Clim. **2013**, 465–570.
54. Cuéllar-Franca, R. M.; Azapagic, A. Carbon capture, storage and utilisation technologies: A critical analysis and comparison of their life cycle environmental impacts. J. CO2 Util. **2015**, 9, 82–102.
55. GCCSI The global status of CCS: 2012; Canberra, Australia, **2012**; ISBN 9780987186317.
56. Smith, K. L.; Steven, M. D.; Jones, D. G.; West, J. M.; Coombs, P.; Green, K. A.; Barlow, T. S.; Breward, N.; Gwosdz, S.; Krüger, M.; Beaubien, S. E.; Annunziatellis, A.; Graziani, S.; Lombardi, S. Environmental impacts of CO2 leakage: Recent results from the ASGARD facility, UK. Energy Procedia **2013**, 37, 791–799.
57. Zhao, X.; Deng, H.; Wang, W.; Han, F.; Li, C.; Zhang, H.; Dai, Z. Impact of naturally leaking carbon dioxide on soil properties and ecosystems in the Qinghai-Tibet plateau. Sci. Rep. **2017**, 7, 1–11.
58. Leung, D. Y. C.; Caramanna, G.; Maroto-Valer, M. M. An overview of current status of carbon dioxide capture and storage technologies. Renew. Sustain. Energy Rev. **2014**, 39, 426–443.
59. Arts, R.; Eiken, O.; Chadwick, A.; Zweigel, P.; van der Meer, L.; Zinszner, B. Monitoring of CO2injected at Sleipner using time-lapse seismic data. Energy **2004**, 29, 1383–1392.
60. Kiessling, D.; Schmidt-Hattenberger, C.; Schuett, H.; Schilling, F.; Krueger, K.; Schoebel, B.; Danckwardt, E.; Kummerow, J. Geoelectrical methods for monitoring geological CO2storage: First results from cross-hole and surface-downhole measurements from the CO2SINK test site at Ketzin (Germany). Int. J. Greenh. Gas Control **2010**, 4, 816–826.
61. Riding, J. B.; Rochelle, C. A. The IEA Weyburn CO2 monitoring and storage project - Final report of the European research team. Greenh. Gas Control Technol. **2005**, 2075–2078.
62. Gerstenberger, M.; Nicol, a.; Stenhouse, M.; Allinson, G.; Berryman, K.; Doody, B.; Ho, M.; McCurdy, M.; Neal, P.; Stirling, M.; Webb, T.; Wright, K. Opportunities for underground geological storage of CO2 in New Zealand -Report CCS-08/10- Risk assessment methodologies; **2009**; ISBN 9780478197273.

63. Bielinski, A.; Kopp, A.; Schütt, H.; Class, H. Monitoring of CO2 plumes during storage in geological formations using temperature signals: Numerical investigation. Int. J. Greenh. Gas Control **2008**, 2, 319–328.
64. Jenkins, C. R.; Cook, P. J.; Ennis-King, J.; Undershultz, J.; Boreham, C.; Dance, T.; de Caritat, P.; Etheridge, D. M.; Freifeld, B. M.; Hortle, A.; Kirste, D.; Paterson, L.; Pevzner, R.; Schacht, U.; Sharma, S.; Stalker, L.; Urosevic, M. Safe storage and effective monitoring of CO2 in depleted gas fields. Proc. Natl. Acad. Sci. **2012**, 109, E35–E41.
65. Lee, B. Review of the present status of optical fiber sensors. Opt. Fiber Technol. **2003**, 9, 57–79.
66. Udd, E. An overview of fiber-optic sensors. Rev. Sci. Instrum. **1995**, 66, 4015–4030, doi:10.1063/1.1145411.
67. Kersey, A. D. A review of recent developments in fiber optic sensor technology. Opt. Fiber Technol. **1996**, 2, 291–317.
68. Hromadka, J.; Tokay, B.; Correia, R.; Morgan, S. P.; Korposh, S. Carbon dioxide measurements using long period grating optical fibre sensor coated with metal organic framework HKUST-1. Sensors Actuators, B Chem. **2018**, 255, 2483–2494.
69. Shivananju, B. N.; Yamdagni, S.; Fazuldeen, R.; Sarin Kumar, A. K.; Hegde, G. M.; Varma, M. M.; Asokan, S. CO 2 sensing at room temperature using carbon nanotubes coated core fiber Bragg grating. Rev. Sci. Instrum. **2013**, 84, 065002.
70. Chong, X.; Kim, K. J.; Ohodnicki, P. R.; Li, E.; Chang, C. H.; Wang, A. X. Ultrashort Near-Infrared Fiber-Optic Sensors for Carbon Dioxide Detection. IEEE Sens. J. **2015**, 15, 5327–5332.
71. Wolfbeis, O. S.; Weis, L. J.; Ziegler, W. E.; Leiner, M. J. P. Fiber-Optic Fluorosensor for Oxygen and Carbon Dioxide. Anal. Chem. **1988**, 60, 2028–2030.
72. Chu, C.-S.; Lo, Y.-L.; Sung, T.-W. Review on recent developments of fluorescent oxygen and carbon dioxide optical fiber sensors. Photonic Sensors **2011**, 1, 234–250.
73. Wolfbeis, O. S.; Kovács, B.; Goswami, K.; Klainer, S. M. Fiber-optic fluorescence carbon dioxide sensor for environmental monitoring. Mikrochim. Acta **1998**, 129, 181–188.
74. Lee, B. H.; Kim, Y. H.; Park, K. S.; Eom, J. B.; Kim, M. J.; Rho, B. S.; Choi, H. Y. Interferometric fiber optic sensors. Sensors (Basel). **2012**, 12, 2467–86.
75. Villatoro, J.; Kreuzer, M. P.; Jha, R.; Minkovich, V. P.; Finazzi, V.; Badenes, G.; Pruneri, V. Photonic crystal fiber interferometer for chemical vapor detection with high sensitivity. Opt. Express **2009**, 17, 1447.
76. Hoo, Y. L.; Jin, W.; Shi, C.; Ho, H. L.; Wang, D. N.; Ruan, S. C. Design and Modeling of a Photonic Crystal Fiber Gas Sensor. Appl. Opt. **2003**, 42, 3509.
77. Ritari, T.; Tuominen, J.; Ludvigsen, H.; Petersen, J. C.; Sørensen, T.; Hansen, T. P.; Simonsen, H. R. Gas sensing using air-guiding photonic bandgap fibers. Opt. Express **2004**, 12, 4080.
78. Hoo, Y. L.; Jin, W.; Ho, H. L.; Ju, J.; Wang, D. N. Gas diffusion measurement using hollow-core photonic bandgap fiber. Sensors Actuators, B Chem. **2005**, 105, 183–186.
79. Yang, F.; Jin, W.; Cao, Y.; Ho, H. L.; Wang, Y. Towards high sensitivity gas detection with hollow-core photonic bandgap fibers. Opt. Express **2014**, 22, 24894.
80. Yang, F.; Tan, Y.; Jin, W.; Lin, Y.; Qi, Y.; Ho, H. L. Hollow-core fiber Fabry–Perot photothermal gas sensor. Opt. Lett. **2016**, 41, 3025.
81. Lin, Y.; Jin, W.; Yang, F.; Tan, Y.; Ho, H. L. Performance optimization of hollow-core fiber photothermal gas sensors. Opt. Lett. **2017**, 42, 4712.
82. Yang, X.; Shi, C.; Wheeler, D.; Newhouse, R.; Chen, B.; Zhang, J. Z.; Gu, C. High-sensitivity molecular sensing using hollow-core photonic crystal fiber and surface-enhanced Raman scattering. J. Opt. Soc. Am. A. Opt. Image Sci. Vis. **2010**, 27, 977–984.
83. Cubillas, a M.; Silva-Lopez, M.; Lazaro, J. M.; Conde, O. M.; Petrovich, M. N.; Lopez-Higuera, J. M. Methane detection at 1670-nm band using a hollow-core photonic bandgap fiber and a multiline algorithm. Opt. Express **2007**, 15, 17570–17576.
84. Ahmed, F.; Ahsani, V.; Melo, L.; Wild, P.; Jun, M. B. G. Miniaturized Tapered Photonic Crystal Fiber Mach-Zehnder Interferometer for Enhanced Refractive Index Sensing. IEEE Sens. J. **2016**, 16, 8761–8766.
85. Li, L.; Xia, L.; Xie, Z.; Liu, D. All-fiber Mach-Zehnder interferometers for sensing applications. Opt. Express **2012**, 20, 11109–20.

86. Lee, B., Review of the present status of optical fiber sensors. Optical Fiber Technology, 2003. 9(2): p. 57-79.
87. Grattan, K.T.V.a.T.S., Fiber optic sensor technology; an overview. Sensors and Actuators A, **2000**. 82: p. 40-61.
88. Fidanboylu, K., and Efendioğlu, H. S, Fiber Optic Sensors And their Applications. 5th International Advanced Technologies Symposium (IATS'09), **2009**.
89. Villatoro, J. and D. Monzón-Hernández, Low-Cost Optical Fiber Refractive-Index Sensor Based on Core Diameter Mismatch. Journal of Lightwave Technology, **2006**. 24(3): p. 1409.
90. Buric, M.P., et al., Enhanced spontaneous Raman scattering and gas composition analysis using a photonic crystal fiber. Applied Optics, **2008**. 47(23): p. 4255-4261.
91. Yang, X., et al. Multiplexed gas sensing based on Raman spectroscopy in photonic crystal fiber. in IEEE Photonics Conference 2012. **2012**.
92. Stewart, G., et al., Design of a fibre optic multi-point sensor for gas detection. Sensors and Actuators B: Chemical, **1998**. 51(1): p. 227-232.
93. Stewart, G., F.A. Muhammad, and B. Culshaw, Sensitivity improvement for evanescent-wave gas sensors. Sensors and Actuators B: Chemical, **1993**. 11(1): p. 521-524.
94. He, X. and G.A. Rechnitz, Linear Response Function for Fluorescence-Based Fiber-Optic CO2 Sensors. Analytical Chemistry, **1995**. 67(13): p. 2264-2268.
95. Abdelghani, A., et al., Surface plasmon resonance fibre-optic sensor for gas detection. Sensors and Actuators B: Chemical, **1997**. 39(1): p. 407-410.
96. A Elosua, C.; Arregui, F.J.; Villar, I.D.; Ruiz-Zamarreño, C.; Corres, J.M.; Bariain, C.; Goicoechea, J.; Hernaez, M.; Rivero, P.J.; Socorro, A.B. et al. Micro and Nanostructured Materials for the Development of Optical Fibre.. Sensors **2017**, 17, 2312.
97. Elosua, C.; Matias, I.R.; Bariain, C.; Arregui, F.J. Volatile organic compound optical fiber sensors: A review. Sensors **2006**, 6, 1440–1465.
98. Miao, Y.-P.; Jin, W.; Yang, F.; Lin, Y.-C.; Tan, Y.-Z.; Hoi, L.H. Advances in optical fiber photothermal interferometry for gas detection. Wuli Xuebao/Acta Phys. Sin. **2017**, 66.
99. Lin, J. Recent development and applications of optical and fiber-optic pH sensors. TrAC Trends Anal. Chem.**2000**, 19.
100. A Rivero PJ, Goicoechea J, Arregui FJ. Optical Fiber Sensors Based on Polymeric Sensitive Coatings. Polymers. **2018**; 10(3):280.
101. A. Fasano, G. Woyessa, P. Stajanca, C. Markos, A. Stefani, K. Nielsen, H. K. Rasmussen, K. Krebber, and O. Bang. Fabrication and characterization of polycarbonate microstructured polymer optical fibers for high temperature-resistant fiber Bragg Grating strain sensors, Opt. Mater. Express 6(2), 649 (**2016**).
102. A. G. Leal-Junior, A. Frizera, and M. José Pontes, Sensitive zone parameters and curvature radius evaluation for polymer optical fiber curvature sensors, Opt. Laser Technol. 100, 272–281 (**2018**).
103. G. Woyessa, K. Nielsen, A. Stefani, C. Markos, and O. Bang, Temperature insensitive hysteresis free highly sensitive polymer optical fiber Bragg grating humidity sensor, Opt. Express 24(2), 1206–1213 (**2016**).
104. G. Woyessa, J. K. M. Pedersen, A. Fasano, K. Nielsen, C. Markos, H. K. Rasmussen, and O. Bang, Zeonex-PMMA microstructured polymer optical FBGs for simultaneous humidity and temperature sensing, Opt. Lett.42(6), 1161–1164 (**2017**).
105. C. A. F. Marques, R. Min, A. Leal Junior, P. Antunes, A. Fasano, G. Woyessa, K. Nielsen, H. K. Rasmussen, B. Ortega, and O. Bang, Fast and stable gratings inscription in POFs made of different materials with pulsed 248 nm KrF laser, Opt. Express 26, 2013-2022, **2018**.
106. Rui Min, Beatriz Ortega, and Carlos Marques, Fabrication of tunable chirped mPOF Bragg gratings using a uniform phase mask, Opt. Express 26, 4411-4420 (**2018**).
107. Arnaldo G. Leal-Junior, Antreas Theodosiou, Carlos Marques, Maria José Pontes, Kyriacos Kalli, and Anselmo Frizera, Compensation Method for Temperature Cross-Sensitivity in Transverse Force Applications With FBG Sensors in POFs, J. Lightwave Technol. 36, 3660-3665 (**2018**).
108. Leal-Junior A, Theodosiou A, Díaz C, et al. Polymer Optical Fiber Bragg Gratings in CYTOP Fibers for Angle Measurement with Dynamic Compensation. Polymers (Basel). **2018**; 10(6):674.

109. Marques CAF, Pospori A, Demirci G, et al. Fast Bragg Grating Inscription in PMMA Polymer Optical Fibres: Impact of Thermal Pre-Treatment of Preforms. Sensors (Basel). **2017**; 17(4):891.
110. Marques, Carlos, Leal Junior, Arnaldo, Rui, Min, et al. Advances on Polymer Optical Fiber Gratings Using a KrF Pulsed Laser System Operating at 248 nm. Fibers. 6. 13, **2018**.
111. R. Min, C. Marques, K. Nielsen, O. Bang and B. Ortega, Fast Inscription of Long Period Gratings in Microstructured Polymer Optical Fibers, in IEEE Sensors Journal, vol. 18, pp. 1919-1923, **2018**.
112. Saharudin, S.; Isha, K.M.; Mahmud, Z.; Herman, S.H.; Noor, U.M. Performance evaluation of optical fiber sensor using different oxygen sensitive nano-materials. In Proceedings of the 2013 IEEE 4th International Conference on Photonics (ICP), Melaka, Malaysia, **2013**; pp. 309–312.
113. Zolkapli, M.; Saharudin, S.; Herman, S.H.; Abdullah,W.F.H. The Influence of Sol-Gel Coated Length and Withdrawal Rate on Plastic Optical Fiber Core towards Oxygen Gas Sensing Sensitivity. J. Teknol. **2016**, 78, 87–91.
114. Domingues, Fatima; Rodriguez, Camilo; Martins, Joana, et al. Cost-effective optical fiber pressure sensor based on intrinsic Fabry-Perot interferometric micro-cavities. Optical Fiber Technology. 42. 56-62, **2018**.
115. R. Wang and X. Qiao, Hybrid optical fiber Fabry-Perot interferometer for simultaneous measurement of gas refractive index and temperature, Applied Optics, vol. 53, pp. 7724-7728, **2014**.
116. Sun H, Zhang J, Rong Q, Feng D, Du Y, Zhang X, et al. A hybrid fiber interferometer for simultaneous refractive index and temperature measurements based on Fabry–Perot/ Michelson interference, IEEE Sensors Journal. **2013**; 13(5):2039-2044.
117. P. Jia, G. Fang, T. Liang, Y. Hong, Q. Tan, X. Chen, et al., Temperature-compensated fiber-optic Fabry–Perot interferometric gas refractive-index sensor based on hollow silica tube for high-temperature application, Sensors and Actuators B: Chemical, vol. 244, pp. 226-232, **2017**.
118. Qiang Liu, Liang Xin, and Zhaoxia Wu, Refractive index sensor of a photonic crystal fiber Sagnac interferometer based on variable polarization states, Applied Physics Express, Volume 12(6), **2019**.
119. L. Li, L. Xia, Z. Xie, and D. Liu, All-fiber Mach-Zehnder interferometers for sensing applications, Optics Express, vol. 20, pp. 11109-11120, **2012**.
120. Choi, H.Y., M.J. Kim, and B.H. Lee, All-fiber Mach-Zehnder type interferometers formed in photonic crystal fiber. Optics Express, **2007**. 15(9): p. 5711-5720.
121. Chen, X., et al., Temperature insensitive bending sensor based on in-line Mach-Zehnder interferometer. Photonic Sensors, **2013**. 4(3): p. 193-197.
122. Hu, L.M., et al., Photonic Crystal Fiber Strain Sensor Based on Modified Mach–Zehnder Interferometer. IEEE Photonics Journal, **2012**. 4(1): p. 114-118.
123. Fu, J., et al., In-Fiber M-Z Interferometer Based on Cascaded Long Period Gratings in Embedded-Core Fiber. IEEE Photonics Technology Letters, **2017**. 29(21): p. 1876-1879.
124. Mao, L., et al., Highly sensitive curvature sensor based on single-mode fiber using core-offset splicing. Optics & Laser Technology, **2014**. 57(Supplement C): p. 39-43.
125. Wang, Q., et al., Comparative Analyses of Bi-Tapered Fiber Mach-Zehnder Interferometer for Refractive Index Sensing. IEEE Transactions on Instrumentation and Measurement, **2017**. 66(9): p. 2483-2489.
126. Ahmed, F., et al., Bragg Grating Embedded in Mach-Zehnder Interferometer for Refractive Index and Temperature Sensing. IEEE Photonics Technology Letters, **2016**. 28(18): p. 1968-1971.
127. Deng, M., et al., Highly sensitive temperature sensor based on an ultra-compact Mach-Zehnder interferometer with side-opened channels. Optics Letters, **2017**. 42(18): p. 3549-3552.
128. Wang, J.-N. and J.-L. Tang, Photonic Crystal Fiber Mach-Zehnder Interferometer for Refractive Index Sensing. Sensors, **2012**. 12(3).
129. Wu, S., et al., Mode-filtered light methane gas sensor based on cryptophane A. Analytica Chimica Acta, **2009**. 633(2): p. 238-243.
130. Yang, J., et al., Sensitivity enhancing of transition mode long-period fiber grating as methane sensor using high refractive index polycarbonate/cryptophane A overlay deposition. Sensors and Actuators B: Chemical, **2015**. 207, Part A: p. 477-480.

131. Liu, S., et al., Liquid-filled simplified hollow-core photonic crystal fiber. Optics & Laser Technology, **2014**. 64: p. 140-144.
132. Tao, C., et al., Optical fiber sensing element based on luminescence quenching of silica nanowires modified with cryptophane-A for the detection of methane. Sensors and Actuators B: Chemical, **2011**. 156(2): p. 553-558.
133. Cregan, R.F., et al., Single-Mode Photonic Band Gap Guidance of Light in Air. Science, **1999**. 285(5433): p. 1537.
134. Bo Dong, E.J.H., Core-offset hollow core photonic bandgap fiber based intermodal interferometer for strain and temperature measurement. Optical Society of America, **2011**. 50: p. 3011-3014.
135. Jin, W., et al., Gas detection with micro- and nano-engineered optical fibers. Optical Fiber Technology, **2013**. 19(6, Part B): p. 741-759.
136. Wang, D.N. Micro-engineered Optical Fiber Sensors Fabricated by Femtosecond Laser Micromachining. in Imaging and Applied Optics Technical Papers. **2012**. Monterey, California: Optical Society of America.
137. Xuefeng, L., et al., Fabrication of Photonic Bandgap Fiber Gas Cell Using Focused Ion Beam Cutting. Japanese Journal of Applied Physics, **2009**. 48(6S): p. 06FK05.
138. K. Nazeri, V. Ahsani, F. Ahmed, H. Joe, M. Jun and C. Bradley, "Experimental comparison of the effect of the structure on MZI fiber gas sensor performance," 2019 IEEE Pacific Rim Conference on Communications, Computers and Signal Processing (PACRIM), Victoria, BC, Canada, **2019**, pp. 1-6.
139. Xiao, G.Z., et al., Monitoring changes in the refractive index of gases by means of a fiber optic Fabry-Perot interferometer sensor. Sensors and Actuators A: Physical, **2005**. 118(2): p. 177-182.
140. Benabid, F. and P.J. Roberts, Linear and nonlinear optical properties of hollow core photonic crystal fiber. Journal of Modern Optics, **2011**. 58(2): p. 87-124.
141. Zhi-guo, Z., et al., Gas sensing properties of index-guided PCF with air-core. Optics & Laser Technology, **2008**. 40(1): p. 167-174.
142. Wang, W. Wei, M. Guo, and Y. Zhao, Optimization of Cascaded Fiber Tapered Mach-Zehnder Interferometer and Refractive Index Sensing Technology vol. 222: Sensors amd Actuators B: Chemical, **2016**.
143. N. L. P. Andrews, R. Ross, D. Munzke, C. van Hoorn, A. Brzezinski, J. A. Barnes, et al., "In-fiber Mach-Zehnder interferometer for gas refractive index measurements based on a hollow-core photonic crystal fiber," Optics Express, vol. 24, pp. 14086-14099, 2016/06/27 **2016**.
144. M. S. Ferreira, L. Coelho, K. Schuster, J. Kobelke, J. L. Santos, and O. Frazão, "Fabry–Perot cavity based on a diaphragm-free hollow-core silica tube," Optics Letters, vol. 36, pp. 4029-4031, 2011/10/15 **2011**.
145. P. Jia, G. Fang, T. Liang, Y. Hong, Q. Tan, X. Chen, et al., "Temperature-compensated fiber-optic Fabry–Perot interferometric gas refractive-index sensor based on hollow silica tube for high-temperature application," Sensors and Actuators B: Chemical, vol. 244, pp. 226-232, 2017/06/01/ **2017**.
146. H. Zhang, S. Gao, Y. Luo, Z. Chen, "Ultrasensitive Mach-Zehnder Interferometric Temperature Sensor Based on Liquid-Filled D-Shaped Fiber Cavity", Sensors, 18. 1239. 10.3390/s18041239, **2018**.
147. Hai-wei, et al., "Fourier Analysis Applied on MZI Transmission Spectrum for Refractive Index Measurement", Photonics Technology Letters, IEEE, 27, **2015**, Pages 658-660.
148. Knight, J.C., et al., All-silica single-mode optical fiber with photonic crystal cladding. Optics Letters, 1996. 21(19): p. 1547-1549.
149. Chen, D. and L. Shen, Highly Birefringent Elliptical-Hole Photonic Crystal Fibers With Double Defect. Journal of Lightwave Technology, 2007. 25(9): p. 2700-2705.
150. Ademgil, H. and S. Haxha, Endlessly single mode photonic crystal fiber with improved effective mode area. Optics Communications, 2012. 285(6): p. 1514-1518.
151. Hao, R., et al., Photonic crystal fiber with high birefringence and low confinement loss. Optik - International Journal for Light and Electron Optics, 2013. 124(21): p. 4880-4883.
152. Birks, T.A., J.C. Knight, and P.S.J. Russell, Endlessly single-mode photonic crystal fiber. Optics Letters, 1997. 22(13): p. 961-963.
153. Jiangbing Du, Y.D., Gordon K. P. Lei,Weijun Tong,Chester Shu., Photonic crystal fiber based MZI for DPSK signal demodulation. Optical Society of America, 2010. 18: p. 7917-7922.

154. Hu, L.M., et al., Photonic Crystal Fiber Strain Sensor Based on Modified Mach–Zehnder Interferometer. IEEE Photonics Journal, 2012. 4(1): p. 114-118.
155. https://www.rp-photonics.com/photonic_crystalfibers.html
156. Xue, J., et al., Polarization filter characters of the gold-coated and the liquid filled photonic crystal fiber based on surface plasmon resonance. Optics Express, 2013. 21(11): p. 13733-13740.
157. Wang, Y., et al., Selectively Infiltrated Photonic Crystal Fiber With Ultrahigh Temperature Sensitivity. IEEE Photonics Technology Letters, 2011. 23(20): p. 1520-1522.
158. Chen, X., et al., Temperature insensitive bending sensor based on in-line Mach-Zehnder interferometer. Photonic Sensors, 2013. 4(3): p. 193-197.
159. Choi, H.Y., M.J. Kim, and B.H. Lee, All-fiber Mach-Zehnder type interferometers formed in photonic crystal fiber. Optics Express, 2007. 15(9): p. 5711-5720.
160. Lee, B.H., et al., Interferometric fiber optic sensors. Sensors (Basel), 2012. 12(3): p. 2467-86.
161. Ming Deng, C.-P.T., Tao Zhu,Yun-Jiang Rao., PCF-based Fabry–Pe´ rot interferometric sensor for strain measurement at high temperatures. IEEE PHOTONICS TECHNOLOGY LETTERS, 2011. 23: p. 700-703.
162. MacPherson, W.N., et al., Remotely addressed optical fibre curvature sensor using multicore photonic crystal fibre. Optics Communications, 2001. 193(1–6): p. 97-104.
163. Li, C., et al., Ultra-Sensitive Refractive Index Sensor With Slightly Tapered Photonic Crystal Fiber. IEEE Photonics Technology Letters, 2012. 24(19): p. 1771-1774.
164. Qiu, S.-j., et al., Miniature tapered photonic crystal fiber interferometer with enhanced sensitivity by acid microdroplets etching. Applied Optics, 2011. 50(22): p. 4328-4332.
165. Katsunari Okamoto, Fundamentals of optical waveguides (second edition).
166. Marcuse, D. Light transmission optics, New York: Van Nostrand Rein-hold, 1972.
167. Marcuse D. Theory of dielectric optical waveguides. New York: Academic press, 1974.
168. Stratton J.A. Electromagnetic Theory. New York: McGraw-Hill.
169. Hardy, A., W. Streifer. Coupled-mode theory of parallel waveguides. IEEE J.lightwave Tech., 1985.
170. Marcatili, E. A. J. Improved coupled-mode equations for dielectric guides. IEEE J. Quantum Electron, 1986.

Appendix A

Photonic Crystal Fiber Based Refractive Index Sensors

Published in TechConnect Briefs 2017 on Biotech, Biomaterial and Biomedical
K. Nazeri, V. Ahsani, F. Ahmed, P.C. Lee, and M.B.G. Jun

Abstract

In this work, two methods of fabricating Mach-Zehnder Interferometer (MZI) for sensitive ambient refractive index (IR) measurement have been proposed by using photonic crystal fiber (PCF). PCF-MZI is fabricated by fusion splicing a short length of PCF between two single-mode fibers (SMF) with fully collapsed air holes in the splicing region. Consequently, the fundamental core mode of PCF can be coupled to cladding modes at the first coupling region and then re-coupled back to the core mode at the second coupling region. Miniaturized MZI is constructed using sharply tapered PCF and the influence of sharp-tapering is then studied. Sharp-tapering over a short length of PCF is utilized by using tiny flame geometry. Experimental results verify that sharp-tapering has a greater impact on refractive index sensitivity enhancement compared to decreasing the taper waist diameter. MZI with a length of 3.8 mm and a taper waist diameter of 65 μm shows an RI sensitivity of 334 nm/RIU to ambient refractive index in the RI range of 1.3327 to 1.3463, 673 nm/RIU for an RI range of 1.3436 to 1.3917, and 1426.7 nm/RIU for a range of 1.3917 to 1.4204. Furthermore, two types of polymer-deposited PCF-MZI are fabricated. Chitosan with an RI of ~ 1.54 and Polycaprolactone (PCL) with RI of ~1.15 were deposited into the cladding air holes of the PCF using capillary force. Chitosan-filled PCF with a length of 10 mm shows an RI sensitivity of 198.6 nm/RIU for an RI range of 1.3327-1.3478, 474.5 nm/RIU for an RI range of 1.3478 to 1.3917, and 677.8 nm/RIU for an RI range of 1.3917-

1.4204.

1. Introduction

Unique properties of fiber-optic interferometric sensors such as light weight, ability of high-resolution detection, and immunity to electromagnetic waves have made them a better choice over conventional sensors. Researchers have investigated different properties of Photonic Crystal Fiber such as frequency-range of single-mode operation [148], high birefringence [149], and large mode area [150]. PCF owes its waveguide properties to an arrangement of tiny and closely spaced air holes which goes through the length of fiber [151]. Knowing the fact that regions with missing holes have a higher effective refractive index is essential to understanding the guiding properties of PCF [152]. Generally in PCF, index difference between core mode and cladding mode is larger than 0.01 [153]. This property will cause a large delay within a short length of PCF, while keeping optical attenuation of the cladding mode at a relatively low level [154]. Additionally, the guiding properties can be strongly modified by having the possibility to fill the air holes with functional gases or liquids [152, 155]. Practical devices have been made based on solution-filled PCFs such as polarization filters [156] and optical fiber sensors [157].

In addition to rapid development of PCF, new types of MZIs have been proposed using different methods such as core mismatch splicing [158], cladding collapse [159], fiber tapering [160], and hollow-core fiber splicing [161]. Using a beam splitter, an incident light will split into two arms and then recombine by a second splitter. This recombined light will produce an interference fringe according to the optical path difference (OPD) of the two arms. In the case of using MZI for ambient RI sensing, the sensing arm is exposed to solution while the reference arm is kept isolated. Ambient RI changes the OPD of MZI and

variation in the interference pattern can be quantified.

The first PCF-MZI was proposed by MacPherson et al. [162]. Moreover, tapered PCF-MZI sensor was proposed by Lie et al. with a sensing length of 2.4 cm and a taper waist diameter of 30 μm in order to achieve RI sensitivity of 1600 nm/RIU [163]. Too much reduction in taper waist can cause a reduction in the rigidity of the sensor. Acid etching of PCF was also reported for sensing applications in which short sensor length sensor is required [164]. As mentioned above, it is possible to make interference between the core mode and cladding modes of PCF. By placing two coupling regions along the PCF and using collapse-method, MZI sensors in SMF-PCF-SMF configuration have been demonstrated, as schematically shown on figure 1-a. This type of MZI usually shows sinusoidal interference spectra over a wide range of wavelength. In order to improve refractive index sensitivity, two different methods of making PCF-MZI are reported in this work. The sensors are fabricated by fusion-splicing PCF between two SMFs with fully collapsed air holes at splicing region. This happens as the structure of PCF has a lower softening point in comparison to SMF.

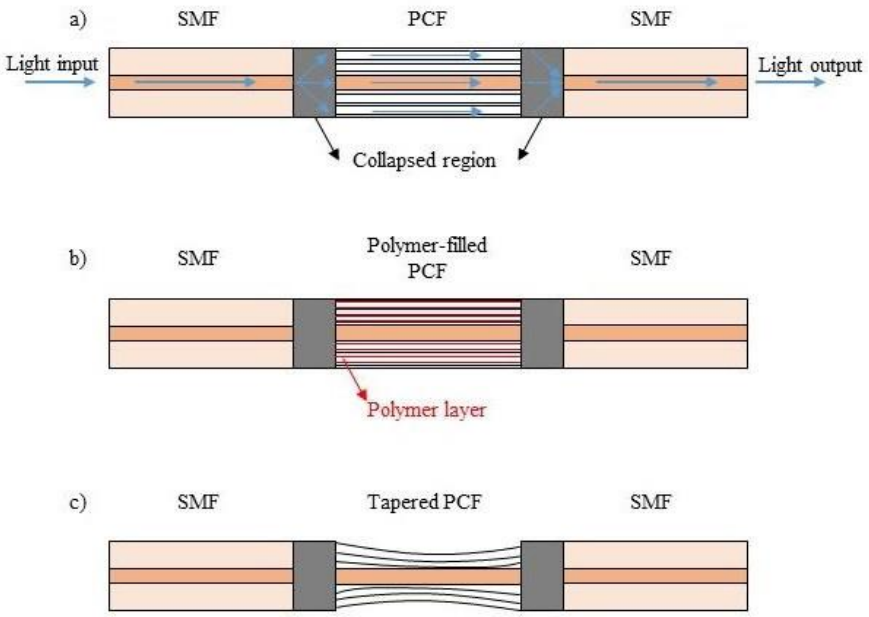

Figure 1. Schematic of a) PCF-MZI; b) Polymer-filled PCF- MZI; c) Tapering of PCF.

In the first method, miniaturized MZI is constructed by using a custom-made tapering machine and by sharply tapering the PCF, while the SMFs on both sides remain unchanged. Figure 1-c shows a schematic view of the tapered PCF-MZI. Generally, a sensor with a smaller PCF diameter shows a higher sensitivity to ambient refractive index as it allows the cladding modes to extend much closer to the solution. All sensors were characterized with different concentration of glycerin solution and the influence of sharp-tapering on PCF-MZI is studied. Results show that sharper tapering over a shorter length of PCF offer significantly higher RI sensitivity. The PCF-MZI with a taper waist diameter of 65 µm and a length of 3.8 mm shows RI sensitivity of 334 nm/RIU for RI range of 1.3327–1.3436, 673 nm/RIU for RI range of 1.3436–1.3917, and 1426.7 nm/RIU for RI range of 1.3917–1.4204. It is possible to tune the birefringence of PCF by changing refractive indices of solution in the air holes. In the second method, the cladding air holes of PCF were first filled with

Chitosan (high refractive index solution) and PCL (low refractive index solution) using capillary force, as shown in Figure 1-b. Later, by splicing a short length of polymer-filled PCF between two SMFs the new configuration was fabricated. The spectral response of interferometer is investigated in terms of wavelength shift. PCL-filled PCF-MZI showed an RI sensitivity of 173 nm/RIU for the RI range of 1.3327 to 1.3917 and 325 nm/RIU for an RI range of 1.3767 to 1.4204. But the Chitosan-filled PCF-MZI exhibited a sensitivity of 198.67 nm/RIU for the RI range of 1.3327 to 1.3478, 474.5 nm/RIU for an RI range of 1.3478 to 1.3917, and 677.8 nm/RIU for an RI range of 1.3917 to 1.4204.

2. Sensor Fabrication

Fibers used in these experiments are SMF28 (core diameter: 8.2μm) and PCF (Newport F-SM10; core diameter: 10μm). This type of PCF has 6 layers of air holes surrounding the solid core. The first step in filling the PCF air holes is to prepare polymer solutions. By mixing 0.5 gr Chitosan with 8 mL acetic acid and 80 mL deionized water, the first polymer solution was prepared. For PCL, 4 gr of PCL was mixed with 80 mL chloroform. Then, a short length of stripped and cleaved PCF was glued to the tip of a needle. The needle was attached to a syringe and the tip of the PCF was immersed in polymer solution. In order to enhance the capillary force, pressure difference was also applied through the syringe. The tip was kept in solution for a day to ensure that the air holes are filled properly. Figure 2 shows a microscopic image of solution-filled PCF. Afterwards, the PCF was heated up in an oven at 250°C for 3 hours, in order to evaporate the solution so that only a very thin layer of polymer remains inside the air holes. PCF-MZI sensors with different lengths were

fabricated and the results of 10 mm PCF are reported and compared in this paper.

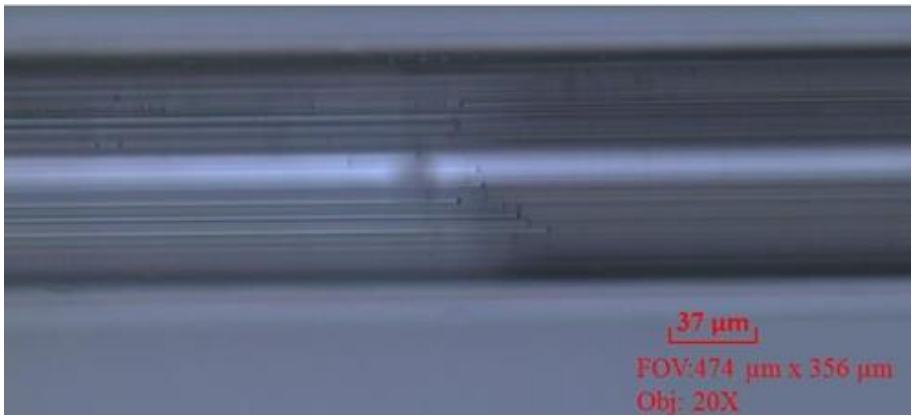

Figure 2. Microscope image of PCF filled with specified solution.

Fujikura fusion splicer was used to splice fibers (FSM 40PM). The optimum splicing condition for polymer-filled PCF was found to be the exposure of an arc power of 45 bit for 1200 milliseconds. The length of collapsing region is ~150 µm with splicing loss of about 5 db.

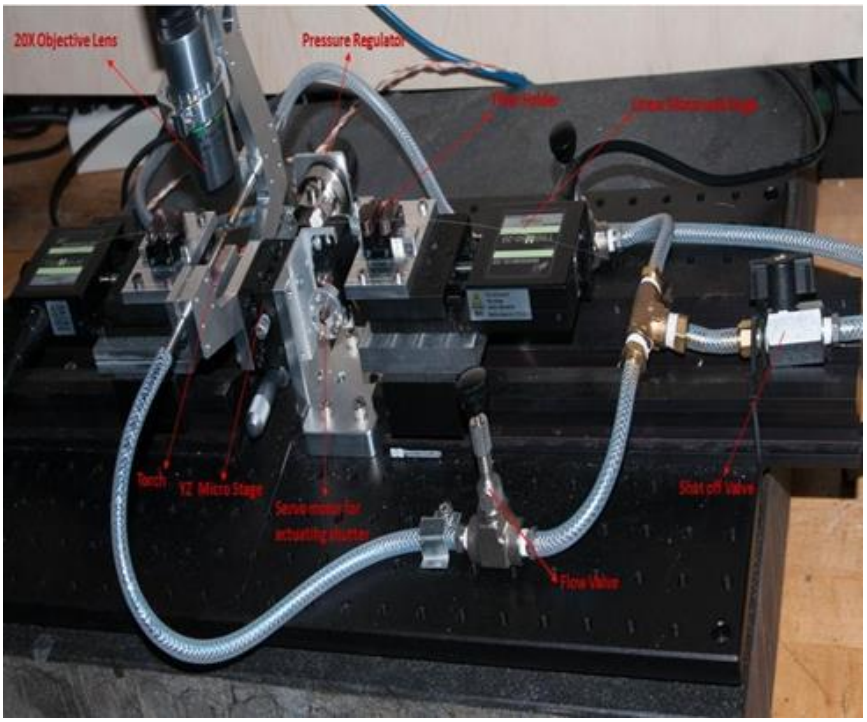

Figure 3. Details of the custom made tapering machine.

For the second experiment, custom made tapering machine was used to fabricate miniaturize MZI, as shown on Figure 3. Fiber holders were mounted on linear stages driven by servomotor with resolution of 1 μm/pulse. A converging-diverging nozzle with inner diameter of 50 μm and outer diameter of 150 μm was used. Hydrogen gas was fed into the nozzle at pressure of 20 psi to produce a flame diameter of 1 mm. The temperature of the flame at the place that fiber passes was measured to be around 1100 °C. The splicing condition for SMF-PCF-SMF configuration was an arc power of 10 bit exposed for 1500 milliseconds. The first collapsed region splits the incoming core mode into core and cladding modes and then recombines them at the second collapsed region. Using this type of nozzles and pulling the fiber at different speeds, various sensors with different waist diameters and taper angles were fabricated. With the speed of 25 μm/s, MZI with a taper waist diameter of 65 μm and a taper angle of 2.4° was fabricated, which is shown in Figure 4. Sharp tapering and reduction in waist diameter enhance the RI sensitivity of the sensor as it enables stronger mode interaction with the ambient.

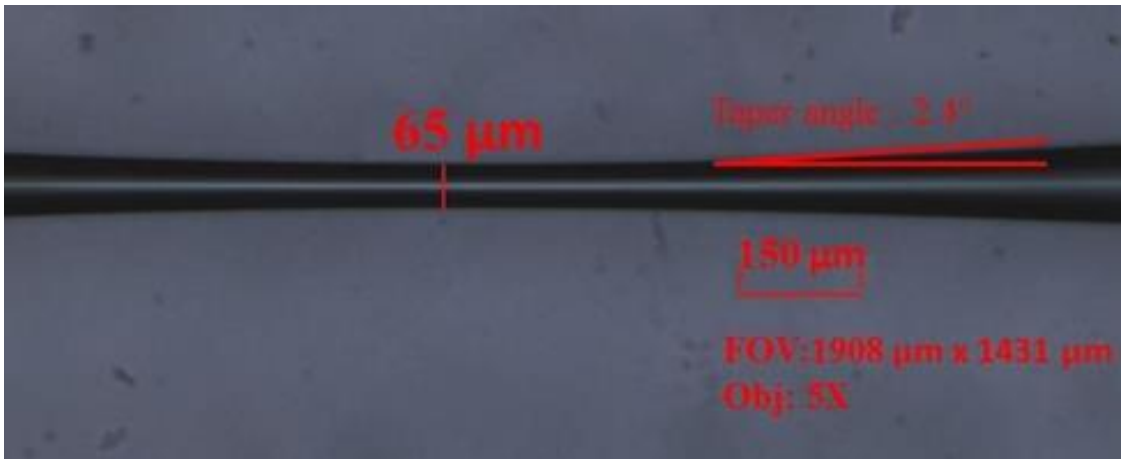

Figure 4. Microscope image of the taper morphology with taper diameter of 65 μm and taper angle of 2.4°

3. Refractive Index Sensing

Sensor performance is evaluated by its sensitivity, which is defined as wavelength shift divided by changes in ambient refractive index. For the case of tapered PCF, effective indices of core and cladding modes depend on the waist diameter of tapered PCF. Additionally, interaction between the evanescent field of the cladding mode and the ambient solution varies the index of cladding mode. Sensors were characterized with different glycerin-solution concentrations at room temperature and after each step cleaned with deionized water. Figure 5 illustrates the wavelength shifts due to changes in surrounding refractive index between 1.3327 and 1.4204 for the normal PCF-MZI, polymer-filled and tapered sensors. Tapered sensors with different waist diameters were fabricated and the results were compared, but the results of tapered PCF-MZI with a waist diameter of 65 µm and a tapering angle of 2.4° is reported in this article. It was concluded that sharp-tapering has a greater impact on refractive index sensitivity enhancement compared to decreasing taper waist diameter. As it is shown, tapered PCF-MZI shows much higher sensitivity compared to the other interferometers.

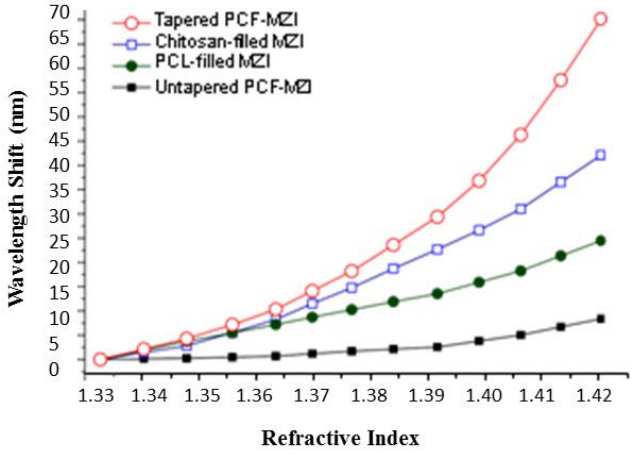

Figure 5. Refractive index sensitivity plots for a normal PCF-MZI, PCL-filled, chitosan filled, and tapered PCF-MZI sensors.

In order to compare the RI sensitivity of tapered and chitosan-filled PCF-MZI, their responses are divided into subplots shown in Figure 6. RI sensitivity of 90 nm/RIU for the IR range of 1.332 to 1.3634, 128 nm/RIU for RI range of 1.3634 to 1.3917, and 378 nm/RIU for range of 1.3917 to 1.4204 was obtained for normal PCF-MZI with a PCF length of 10 mm. The PCL filled with the same length of PCF showed RI sensitivity of 173 nm/RIU for an RI range of 1.3327 to 1.3917 and 325 nm/RIU for the range of 1.3917 to 1.4204. As demonstrated in Figure 6, chitosan-filled sensor with the same length showed RI sensitivity of 198.6 nm/RIU for the range of 1.3327 to 1.3478, 474.5 nm/RIU for RI range of 1.3478 to 1.3917 and 677.84 nm/RIU for RI range of 1.3917 to 1.4204. The tapered PCF-MZI with waist diameter of 65 µm showed RI sensitivity of 334 nm/RIU for RI range of 1.3327 to 1.3436, 673 nm/RIU for range of 1.3436 to 1.3917 and 1426.7 nm/RIU for a range of 1.3917 to 1.4204.

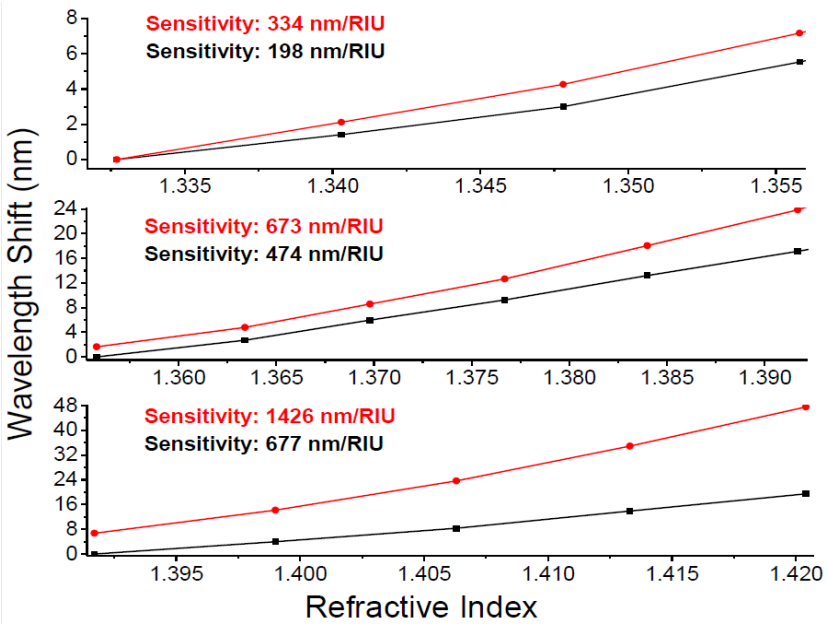

Figure 6. RI sensitivity analysis of tapered PCF-MZI and chitosan-filled MZI sensor.

4. Conclusion

Two sensitive RI sensors were proposed based on PCF using collapsing method. In addition to normal PCF-MZI, two types of polymer-filled sensors and tapered PCF-MZI were fabricated and their spectral responses were investigated. Sensors were characterized with different concentrations of glycerin. Results prove that by depositing a thin layer of appropriate polymer inside the air holes, one could enhance the sensitivity of PCF-MZI sensor to ambient refractive index. Chitosan-filled PCF shows the total wavelength shift of 42 nm due to changes in surrounding RI from 1.3327 to 1.4204. This sensor has RI sensitivity of 198.67 nm/RIU for the range of 1.3327 to 1.3478, 474.5 nm/RIU for RI range of 1.3478 to 1.3917, and 677.84 nm/RIU for RI range of 1.3917 to 1.4204.

Sharp-tapering over a short length of PCF was utilized by using a converging-diverging nozzle and a custom made tapering machine. A tapered sensor with a waist diameter of 65 μm shows a total wavelength shift of 70 nm. Additionally, it has the highest sensitivity with amount of 334 nm/RIU for RI range of 1.3327 to 1.3436, 673 nm/RIU for range of 1.3436 to 1.3917, and 1426.7 nm/RIU for range of 1.3917 to 1.4204. Based on the experiments, it was concluded that sharp-tapering has a greater impact on refractive index sensitivity enhancement compared to decreasing the taper waist diameter.

Appendix B

Principle and theoretical calculation

In order to analyze wave propagation in axially symmetric structures like optical fibers, Maxwell's equations are written in cylindrical coordinates. In a homogeneous dielectric medium, Maxwell's equations can be written in terms of electric field (e) and magnetic field (h) as [168]:

$$\nabla \times e = -\mu \frac{\partial h}{\partial t} \quad \textbf{(Eq. 1)}$$

$$\nabla \times h = \varepsilon \frac{\partial e}{\partial t} \quad \textbf{(Eq. 2)}$$

Considering an electromagnetic wave having angular frequency of ω and propagating in the Z-direction with propagating constant β, the electromagnetic fields in cylindrical coordinates for optical fibers can be written as:

$$\tilde{E} = E(r,\theta)e^{j(\omega t-\beta z)} \quad \textbf{(Eq. 3)}$$

$$\tilde{H} = H(r,\theta)e^{j(\omega t-\beta z)} \quad \textbf{(Eq. 4)}$$

where "r" is position in the plane transverse to Z-axis. By substituting equations 3 and 4 into equations 1 and 2, and writing Maxwell's equations, the following set of equations for analysis of wave propagation in optical fibers can be obtained:

$$\frac{1}{r}\frac{\partial E_z}{\partial \theta} + j\beta E_\theta = -j\omega\mu_0 H_r \quad \textbf{(Eq. 5)}$$

$$\frac{1}{r}\frac{\partial H_z}{\partial \theta} + j\beta H_\theta = -j\omega\varepsilon_0 n^2 E_r \quad \textbf{(Eq. 6)}$$

$$-\frac{\partial E_z}{\partial r} - j\beta E_r = -j\omega\mu_0 H_\theta \quad \textbf{(Eq. 7)}$$

$$-\frac{\partial H_z}{\partial r} - j\beta H_r = j\omega\varepsilon_0 n^2 E_\theta \quad \textbf{(Eq. 8)}$$

$$\frac{1}{r}\frac{\partial(rE_\theta)}{\partial r} - \frac{1}{r}\frac{\partial E_r}{\partial \theta} = -j\omega\mu_0 H_z \quad \textbf{(Eq. 9)}$$

$$\frac{1}{r}\frac{\partial(rH_\theta)}{\partial r} - \frac{1}{r}\frac{\partial H_r}{\partial \theta} = j\omega\varepsilon_0 n^2 E_z \quad \textbf{(Eq. 10)}$$

In axially symmetric optical fibers RI-distribution is not dependent on θ and can be expressed by n(r). Then the transverse electromagnetic fields are related to E_z and H_Z by:

$$E_r = -\frac{j}{[k^2 n(r)^2 - \beta^2]}\left(\beta\frac{\partial E_z}{\partial r} + \frac{\omega\mu_0}{r}\frac{\partial H_z}{\partial \theta}\right) \quad \textbf{(Eq. 11)}$$

$$E_\theta = -\frac{j}{[k^2 n(r)^2 - \beta^2]}\left(\frac{\beta}{r}\frac{\partial E_z}{\partial \theta} - \omega\mu_0\frac{\partial H_z}{\partial r}\right) \quad \textbf{(Eq. 12)}$$

$$H_r = -\frac{j}{[k^2 n(r)^2 - \beta^2]}\left(\beta\frac{\partial H_z}{\partial r} - \frac{\omega\varepsilon_0 n(r)^2}{r}\frac{\partial E_z}{\partial \theta}\right) \quad \textbf{(Eq. 13)}$$

$$H_\theta = -\frac{j}{[k^2 n(r)^2 - \beta^2]}\left(\frac{\beta}{r}\frac{\partial H_z}{\partial \theta} + \omega\varepsilon_0 n(r)^2\frac{\partial H_z}{\partial r}\right) \quad \textbf{(Eq. 14)}$$

Out of infinite possibilities, one should select those answers that satisfy the boundary conditions. The common type of boundary condition takes place when there are discontinuities in refractive index. It should be mentioned that at the boundary, the tangential components of the electromagnetic fields must be continuous [165]. Assume eigen modes of each optical waveguide before mode coupling as $\tilde{E}_p = E_p \exp(-j\beta_p z)\ and\ \tilde{H}_p = H_p \exp(-j\beta_p z)$ with p=1 and p=2. These modes should satisfy the following Maxwell's equation:

$$\nabla \times \tilde{E}_p = -j\omega\mu_0\tilde{H}_p \quad \textbf{(Eq. 15)}$$

$$\nabla \times \tilde{H}_p = j\omega\varepsilon_0 {N_p}^2 \tilde{E}_p \quad \textbf{(Eq. 16)}$$

where $N^2_{P(x,y)}$ is the RI-distribution of each waveguide. Furthermore, assume that the electromagnetic fields of the coupled waveguide can be expressed as the sum of the Eigen modes of each waveguide:

$$\tilde{E} = A(z)\tilde{E}_1 + B(z)\tilde{E}_2 \quad \textbf{(Eq. 17)}$$

$$\tilde{H} = A(z)\tilde{H}_1 + B(z)\tilde{H}_2 \quad \textbf{(Eq. 18)}$$

Again, the electromagnetic fields in the coupled waveguide should satisfy Maxwell's equations. By substituting equations 17 and 18, using vector formulas and separating the transverse and axial dependencies of electromagnetic fields, we obtain: [166]

$$\frac{dA}{dz} + \mathrm{C}_{12}\frac{dB}{dz}exp[-j(\beta_2 - \beta_2)z] + j\chi_1 A + jB\kappa_{12}exp[-j(\beta_2 - \beta_2)z] = 0 \quad \textbf{(Eq. 19)}$$

$$\frac{dB}{dz} + \mathrm{C}_{21}\frac{dA}{dz}exp[+j(\beta_2 - \beta_2)z] + j\chi_2 B + jA\kappa_{21}exp[+j(\beta_2 - \beta_2)z] = 0 \quad \textbf{(Eq. 20)}$$

Where Ƙ is the mode coupling coefficient of the directional coupler and C represents the butt coupling coefficient between two waveguides [169, 170]. Used vector formula and the correlations for Ƙ, χ and C, as well as K_a, K_b, α_a and α_b are:

$$\nabla \times (AE) = A\nabla \times E + \nabla A \times E = A\nabla \times E + \frac{dA}{dz}u_z \times E \quad \textbf{(Eq. 21)}$$

$$\kappa_{pq} = \frac{\omega\varepsilon_0 \int_{-\infty}^{+\infty}\int_{-\infty}^{+\infty}(N^2 - {N_q}^2)E_p^* E_q dxdy}{\int_{-\infty}^{+\infty}\int_{-\infty}^{+\infty}u_z(E_p^* \times H_p + E_p \times H_p^*)dxdy} \quad \textbf{(Eq. 22)}$$

$$\mathrm{C}_{pq} = \frac{\int_{-\infty}^{+\infty}\int_{-\infty}^{+\infty}u_z(E_p^* \times H_q + E_q \times H_p^*)dxdy}{\int_{-\infty}^{+\infty}\int_{-\infty}^{+\infty}u_z(E_p^* \times H_p + E_p \times H_p^*)dxdy} \quad \textbf{(Eq. 23)}$$

$$\chi_p = \frac{\omega\varepsilon_0 \int_{-\infty}^{+\infty}\int_{-\infty}^{+\infty}(N^2 - p^2)E_p^* E_p dxdy}{\int_{-\infty}^{+\infty}\int_{-\infty}^{+\infty}u_z(E_p^* \times H_p + E_p \times H_p^*)dxdy} \quad \textbf{(Eq. 24)}$$

The pair of "p" and "q" are either (p, q) = (1, 2) or (2, 1). $N^2(x, y)$ denotes the RI-distribution in the entire coupled waveguide. The sign (*) denotes the complex conjugate.

$$K_a = \frac{\kappa_{12} - \mathrm{C}_{12}\chi_2}{1 - |\mathrm{C}_{12}|^2} \quad \textbf{(Eq. 25)}$$

$$K_b = \frac{\kappa_{12} - \mathrm{C}^*{}_{12}\chi_1}{1 - |\mathrm{C}_{12}|^2} \quad \textbf{(Eq. 26)}$$

$$\alpha_a = \frac{\kappa_{21}\mathrm{C}_{12} - \chi_1}{1 - |\mathrm{C}_{12}|^2} \quad \textbf{(Eq. 27)}$$

$$\alpha_b = \frac{\kappa_{12} C^*_{12} - \chi_2}{1 - |C_{12}|^2} \quad \textbf{(Eq. 28)}$$

Taking into account δ as the difference of propagation constants between waveguides $\delta = {(\beta_2 - \beta_1)}/{2}$ and rewriting equations 19 and 20, we get the coupled mode equations:

$$\frac{dA}{dz} = -jBK_a \exp(-2j\delta z) + j\alpha_a A \quad \textbf{(Eq. 29)}$$

$$\frac{dB}{dz} = -jAK_b \exp(2\delta z) + j\alpha_b B \quad \textbf{(Eq. 30)}$$

Here the solution for directional coupler with $\beta_1 > 0$ and $\beta_2 > 0$ similar to Mach-Zehnder interferometer with two arms that have the same waveguide structure is derived. For the simple case in which $C_{pq} = \chi_p = 0$ the solutions can be written in the form:

$$A(z) = (a_1 e^{jqz} + a_2 e^{-jqz}) \exp(-j\delta z) \quad \textbf{(Eq. 31)}$$

$$B(z) = (b_1 e^{jqz} + b_2 e^{-jqz}) \exp(+j\delta z) \quad \textbf{(Eq. 32)}$$

Where $q = \sqrt{\kappa^2 + \delta^2}$. As in most of the directional couplers κ_{pq} is real, it is considered that $\kappa = \kappa_{12} = \kappa_{21}$. Additionally, constants a_1, a_2, b_1, b_2 should satisfy the initial conditions $a_1 + a_2 = A(0)$ and $b_1 + b_2 = B(0)$. By substitution in coupled mode equations and consideration of initial conditions, the following solutions are derived:

$$A(z) = \left\{\left[\cos(qz) + j\frac{\delta}{q}\sin(qz)\right] A(0) - j\frac{\kappa}{q}\sin(qz) B(0)\right\} \exp(-j\delta z) \quad \textbf{(Eq. 33)}$$

$$B(z) = \left\{\left[\cos(qz) - j\frac{\delta}{q}\sin(qz)\right] B(0) - j\frac{\kappa}{q}\sin(qz) A(0)\right\} \exp(+j\delta z) \quad \textbf{(Eq. 34)}$$

List of Publications

1) **Kaveh Nazeri**, Colin Bradley, "The Effect of Photonic Crystal Fibre Structure on the Performance of Mach-Zehnder Interferometer Fibre Optic Gas Sensors" in Optical Fiber Technology, 58 (2020), 102294.

2) **Kaveh Nazeri**, Farid Ahmed, Vahid Ahsani, Hang-Eun Joe, Colin Bradley, Ehsan Toyserkani, and Martin B. G. Jun. "Hollow-Core Photonic Crystal Fiber Mach-Zehnder Interferometer for Gas Sensing", Sensors 2020, 20(10), 2807.

3) F Ahmed, V Ahsani, **K Nazeri**, E Marzband, C Bradley, E Toysekani, and MBG Jun, *"Monitoring of Carbon Dioxide Using Hollow-Core Photonic Crystal Fiber Mach–Zehnder Interferometer"* in Sensors 19 (7), 3357.

4) **K Nazeri**, V Ahsani, F Ahmed, HE Joe, MBG Jun, and C Bradley*, "Experimental comparison of the effect of the structure on MZI fiber gas sensor performance",* in 2019 IEEE Pacific Rim Conference on Communications, Computers and Signal Processing (PACRIM).

5) Hang-Eun Joe, **Kaveh Nazeri**, Yonghyun Cho, Farid Ahmed, Jong Kweon Park, M.B.G. Jun, "Microfabrication techniques using a Femtosecond Laser for Fabrication of High Precision Optical Components", in 2018 World Congress on Micro and Nano Manufacturing, December 2017.

6) **K. Nazeri**, V. Ahsani, F. Ahmed, P.C. Lee, and M.B.G. Jun, *"Photonic Crystal Fiber Based Refractive Index Sensors"* in TechConnect World Innovation Conference and Expo, May 2017, Washington DC, USA.

7) F. Ahmed, Y. Cho, **K. Nazeri**, V. Ahsani, P. C. Lee, and M. B. G. Jun, *"Refractive Index Sensing by Femtosecond Laser Fabricated Fiber Optic Sensors"*, 11th International Conference on Micro Manufacturing, Orange County, California, USA, March 2016.